Polymerization kinetics of single microtubules and microtubule bundles under force and confinement

Dissertation

zur Erlangung des Grades eines
Doktors der Naturwissenschaften

der Fakultät Physik
der Technischen Universität Dortmund

vorgelegt von

Björn Zelinski

aus Bochum

Dezember, 2013

Erster Gutachter	Prof. Dr. Jan Kierfeld
Zweiter Gutachter	Dr. Kai P. Schmidt

Kontakt zum Autor bjoern.zelinski@tu-dortmund.de

"Nur Steine ... " Tim Fischer

Abstract

Microtubules are, next to actin filaments, one of the main components of the cytoskeleton of eukaryotic cells. The static and dynamical properties are essential for numerous intracellular processes. Their characteristic polymerization behaviour, called *dynamic instability*, is the key factor of the temporal and spatial organization of the microtubule cytoskeleton. In dynamic instability, microtubules stochastically alternate between phases of polymerization and phases of fast depolymerization. Polymerizing microtubules can generate forces in the piconewton range, which are use in positioning of cellular organelles or chromosome separation. The interplay of dynamic instability and force generation leads to complex polymerization kinetics. In this thesis we investigate the force generation of polymerizing microtubules in the presence of dynamic instability. We establish a coarse-grained model for the polymerization dynamics of single microtubules and include realistic force-velocity relations and velocity-dependent catastrophe models. In the first part of this thesis, the polymerization dynamics of single microtubules are investigated, based on the coarse-grained model, in three different scenarios, which mimic typical cellular environments. The scenarios are as follows: (i) A single microtubule is confined by a rigid and fixed wall, (ii) a single microtubule polymerizes under constant force, and (iii) a single microtubule polymerizes against a elastically coupled obstacle. For all three scenarios we calculate stochastic length distributions analytically and characterize the polymerization dynamics as a function of the growth parameters, like the tubulin concentration, the rescue rate or the obstacle stiffness.

In scenario (i) we introduce a realistic model for wall-induced catastrophes and find exponentially increasing or decreasing stationary length distributions. In scenario (ii) we determine the critical force f_c which provides the transition from unbounded to bounded growth. The critical force is smaller than the stall force and increases logarithmically with the tubulin concentration and rescue rate. In scenario (iii) we calculate the polymerization force for growth against the elastic obstacle in the absence and in the presence of rescue events. For a vanishing rescue rate the maximal polymerization force grows logarithmically with the tubulin concentration and is always smaller than the stall force. In the presence of rescue events, we analytically calculate steady-state length distributions as a function of the growth parameters, and the average polymerization force. In the steady state the average polymerization force equals the critical force f_c for growth

under constant force. In addition, we establish a dynamical mean field theory and compare mean-field results for the average polymerization force to full stochastic calculations. Based on the dynamical mean field theory, we investigate the relaxation dynamics of a single microtubule if growth parameters are perturbed.
The relaxation dynamics into the new steady state is governed by an exponential decay with a characteristic time scale, which is a function of the perturbed growth parameters. Finally we show that results are robust with respect to changes in the force-velocity relation and the catastrophe model.
In the second part of this thesis, we extend the single microtubule model to bundles of parallelly growing microtubules and investigate the polymerization dynamics of microtubule bundles growing against an elastically coupled obstacle. This scenario is close to the *in vitro* experiments by Laan *et al.*. We establish a dynamical mean field theory, characterize the cooperative polymerization dynamics and the generated force, as a function of the growth parameters and the obstacle stiffness. In the absence of rescue events and a stiff obstacle, the maximal polymerization force growth linear in the number of microtubule within the bundle. This is in agreement with results from *in vitro* experiments by Laan *et al.*. For a soft obstacle, we find a crossover to a logarithmic dependency on the microtubule number. For a non-vanishing rescue rate and a soft obstacle, we find an oscillatory polymerization dynamics, governed by *collective catastrophes* and *collective rescues*. The steady-state polymerization force oscillates around its average value and is a linear function of the microtubule number and the tubulin concentration. Finally we investigate the validity of the dynamical mean field theory, based on semi-stochastic calculations.

Zusammenfassung

Mikrotubuli sind, neben Actinfilamenten, der Hauptbestandteil des Zytoskeletts eukaryotischer Zellen. Die statischen und dynamischen Eigenschaften von Mikrotubuli sind existenziell für viele zellinterne Prozesse. Ihr charakteristisches Polymerisationsverhalten, die *dynamische Instabilität*, ist von zentraler Bedeutung für die zeitliche und räumliche Organisation des Mikrotubuli-Zytoskeletts. Unter der dynamischen Instabilität versteht man das stochastische Alternieren von Phasen mit moderater Polymerisation und Phasen schneller Depolymerisation. Polymerisierende Mikrotubuli können Kräfte im Piconewton-Bereich erzeugen, welche zur Positionierung von Zellorganellen oder zur Trennung von Chromosomen genutzt werden. Das Zusammenspiel von dynamischer Instabilität und Krafterzeugung bewirkt eine komplexe Polymerisationsdynamik.

In dieser Arbeit untersuchen wir die Krafterzeugung durch polymerisierende Mikrotubuli unter dem Einfluss der dynamischen Instabilität. Dazu etablieren wir ein idealisiertes Polymerisationsmodell für einzelne Mikrotubuli, welches realistische Kraft-Geschwindigkeits- und geschwindigkeitsabhängige Katastrophenmodelle beinhaltet. Im ersten Teil dieser Arbeit wird die Polymerisationsdynamik einzelner Mikrotubuli, anhand des idealisierten Modells, in drei unterschiedlichen Szenarien untersucht, welche ein typisches zelluläres Umfeld widerspiegeln. Die drei Szenarien sind: (i) Ein einzelner Mikrotubulus polymerisiert in einer durch starre Wände begrenzten Umgebung, (ii) ein einzelner Mikrotubulus polymerisiert unter einer konstanten Kraft und (iii) ein einzelner Mikrotubulus polymerisiert gegen ein elastisches Hindernis, welches eine längenabhängige Kraft erzeugt.

Für alle drei Szenarien bestimmen wir analytische Ausdrücke für die stochastischen Längenverteilungen und charakterisieren die Polymerisationsdynamik in Abhängigkeit der Wachstumsparameter, wie der Tubulinkonzentration, der Rettungsrate und der Härte des elastischen Hindernisses. In Szenario (i) präsentieren wir ein realistisches Modell für Katastrophen, welche durch die starren räumlichen Begrenzungen erzeugt werden. Wir finden exponentiell steigende oder fallende stationäre Längenverteilungen. In Szenario (ii) bestimmen wir die kritische Kraft F_{c}, welche den Übergang von ungebundenem zu gebundenem Wachstum bestimmt. Die kritische Kraft ist kleiner als die stall force and wächst logarithmisch mit der Tubulinkonzentration. In Szenario (iii) berechnen wir die mittlere Kraft, die ein einzelner Mikrotubulus erzeugt. In Abwesenheit von Rettungen wächst

die maximale Polymerisationskraft logarithmisch mit der Tubulinkonzentration und ist kleiner als die sogenannte "stall force" F_{stall}, bei der die Wachstumsgeschwindigkeit verschwindet. Für eine von Null verschiedene Rettungsrate bestimmen wir analytische Ausdrücke für die stationären Längenverteilungen und die mittlere Kraft als Funktionen der Wachstumsparameter. Im stationären Zustand ist die mittlere Kraft gleich der kritischen Kraft F_{c}. Zusätzlich zu stochastischen Berechnungen etablieren wir eine dynamische mean field Theorie und vergleichen Resultate aus beiden Theorien miteinander. Basierend auf der dynamischen mean field Theorie, untersuchen wir das Relaxationsverhalten einzelner Mikrotubuli, nachdem Wachstumsparameter gestört wurden. Wir finden eine exponentielle Relaxationsdynamik mit einer charakteristischen Zeitskala, welche durch die gestörten Wachstumsparameter dominiert wird. Zum Abschluss zeigen wir, das die erhaltenen Resultate robust gegenüber Änderungen in der Kraft- Geschwindigkeits-Relation und des Katastrophenmodelles sind.

Im zweiten Teil dieser Arbeit untersuchen wir die Polymerisationsdynamik von Bündeln aus parallelen Mikrotubuli, die gegen ein elastisches Hindernis wachsen. Dieses Szenario ähnelt den *in vitro* Experimenten, die von Laan *et al.* durchgeführt wurden. Wir etablieren eine dynamische mean field Theorie, charakterisieren die kooperative Polymerisationsdynamik und bestimmen die erzeugte Kraft als Funktion der Wachstumsparameter und der Elastizität des Hindernisses. In Abwesenheit von Rettungen und für ein steifes Hindernis, steigt die maximale Polymerisationskraft linear mit der Anzahl an Mikrotubuli in Übereinstimmung mit Resultaten von Laan *et al.* Für ein weiches Hindernis findet ein Übergang zu einer logarithmischen Abhängigkeit statt. Für eine von Null verschiedene Rettungsrate und ein weiches Hindernis finden wir eine oszillatorische Polymerisationsdynamik, welche durch *kollektive Katastrophen* und *kollektive Rettungen* dominiert wird. Im stationären Zustand oszilliert die Polymerisationskraft stabil um einen Mittelwert und wächst linear mit der Anzahl an Mikrotubuli und der Tubulinkonzentration. Zum Abschluss untersuchen wir die Gültigkeit der dynamischen mean field Theorie anhand semi-stochastischer Rechnungen.

Contents

Acronyms

OPDF overall probability density function

MT microtubule

MTs microtubules

MAPS microtubule-associated proteins

TUB tubulin

GTP guanosine triphosphate

GDP guanosine diphosphate

MFPT mean first-passage time

RNA ribonucleic acid

MTOC microtubule organizing center

ATP adenosine triphosphate

ADP adenosine diphosphate

Thesis overview

In chapter 1 we provide the necessary biological background to this thesis. We focus on the polymerization kinetics of microtubules and actin filaments and discuss three representative examples of force generation by polymerizing microtubules, which provide the basic motivation of this thesis.
In chapter 2 we present a coarse-grained model for microtubule polymerization under a resisting force and in the presence of dynamic instability. We discuss force-velocity relations and force-dependent catastrophe rates.
Chapter 3 deals with stochastic simulations of single microtubules, based on the coarse-grained model presented in chapter 2. Simulation parameters and parameter ranges are specified.
In chapter 4 we present the results for single microtubule polymerization dynamics in three different confinement scenarios: (i) polymerization in confinement by fixed rigid walls, (ii) polymerization under a constant force, and (iii) polymerization against an elastically coupled obstacle. For all three scenarios, we calculate stochastic microtubule length distributions, as a function of growth parameters. We address the relaxation dynamics after growth parameters are perturbed and show that results are robust with respect to changes in the force-velocity relation and the catastrophe model.
In chapter 6 the single microtubule model is extended to bundles of N parallelly growing microtubules. We introduce force-sharing and focus on growth against an elastic obstacle. This scenario is close to recent *in vitro* experiments.
Chapter 7 deals with stochastic simulations of microtubule bundles, based on the model for microtubule bundles discusses in chapter 6.
In chapter 8 we present results for microtubule bundles growing against an elastic obstacle. We establish a dynamical mean field theory and characterize the cooperative polymerization dynamics, as a function of the growth parameters. Finally we test the validity of the dynamical mean field theory, on the basis of semi-stochastic calculations.

Chapter 1

Introduction and motivation

The cytoskeleton of a living cell is a complex and highly dynamical network of biological filaments. Its static and dynamical properties are the basis for almost all mechanical processes inside a living cell. Cell motility, positioning of cellular organelles, cell division and shape generation are intracellular processes, governed by the cytoskeleton. The cytoskeleton is composed of cooperating networks of actin, intermediate, and microtubule filaments. But also regulating proteins and molecular motors are parts of the cytoskeleton. The polymerization dynamics of microtubules and actin filaments, in cooperation with molecular motors, are the key factors of the spatial and temporal organization and reorganization of the cytoskeleton and are, therefore, of particular importance. Continuous research and new experimental techniques, like TIRF-microscopy or optical tweezers, have revealed numerous properties of single microtubule and actin filaments. But in living cells the cooperation of single filaments or the cooperation of different filament types is of central importance. Examples of the cooperation of single filaments are the mitotic spindle in the case of microtubule filaments, and the contractile ring in the case of actin filaments. Neuronal growth cones are a typical example for the cooperation of different filament types. The investigation and characterization of cooperative polymerization dynamics are subject of ongoing research and are also the main objects of this thesis.
In the following section we provide the biological background for this thesis. We focus on the polymerization dynamics of microtubules and actin filaments and their regulation. For a detailed biological introduction we refer to [1]. An introduction to biophysics can be found in [2]. A recently published review article on microtubules can be found in Ref. [3].

1.1 Microtubules and actin filaments

Microtubules (MTs) assemble from the α/β-tubulin heterodimer [1]. The heterodimer, in the following called monomer, is $\sim 8\,\mathrm{nm}$ large [4, 5] and consists of a α- and β-tubulin monomer, bound by a non-exchangeable GTP-nucleotide [6] (see Fig. 1.1). At the β-

tubulin monomer a second, exchangeable GTP-nucleotide is bound, that can either be in the GTP- (non-hydrolyzed) or in the GDP-form (hydrolyzed). Tubulin monomers attach to each other in a "head-to-tail" fashion and form protofilaments. The α-end of the new tubulin monomer is bound by the β-end of the previous monomer via the GTP-nucleotide. MTs usually consist of 13 protofilaments, which form a hollow cylindrical tube with an outer diameter of $\sim 25\,\text{nm}$ (see Fig. 1.1). Protofilaments are laterally bound by non-covalent bonds, which are less stable than bonds between single tubulin monomers within the protofilaments. The exact bond type and their strength are subject of current research [7, 8]. MTs are typically $10-50\,\mu\text{m}$ long [9] and exhibit a persistence length of $\sim 6\,\text{mm}$, which is larger than their typical length [2]. Under typical conditions MTs can be seen as stiff and rigid polymers. The tubulin monomers within each protofilament point in the the same direction and create a structural polarity. Since all protofilaments within the MT are aligned parallelly, the MT itself shows a structural polarity. One can distinguish two different ends: the "$-$"-end consists of α-tubulin while the "$+$"-end consists of β-tubulin. Tubulin monomers in solution show different affinities to both MT ends (see Fig. 1.1)[9]. The addition of new monomers is much faster at the "$+$"-end compared to the "$-$"-end, which can, in general, be regarded as static. MT nucleation can be initiated by an increase of the concentration of free tubulin above a critical concentration. *In vivo*, nucleation is supported by different types of proteins [1]. In centrosomes, a special type of microtubule-organizing center (MTOC), γ-tubulin promotes the nucleation of MTs [2, 10]. The α-end of tubulin monomers binds to the γ-tubulin complex, which is tightly bound to the MTOC. The "$-$"-end of the new nucleated MT is fixed at the MTOC and is protected against depolymerization, while the "$+$"-end freely polymerizes in the cytosol. From the MTOC, often located close to the cell nucleus, MTs grow through the cell periphery towards the cell membrane. In *in vitro* experiments, nucleation of new MTs can also be initiated by an increase of the temperature [11, 12].

Filamentous actin (F-actin) assembles from actin monomers. Actin monomers are $\sim 5\,\text{nm}$ long and possess a ATP-/ADP-nucleotide binding side [1, 2]. As tubulin monomers, actin monomers attach to each other in a "head-to-tail" fashion and form protofilaments with a distinct structural polarity. As in the case of MTs we find a fast-growing "$+$"-end and a slow-growing "$-$"-end with the nucleotide binding side pointing towards the "$-$"-end (see Fig. 1.2). F-actin consists of two protofilaments, that form a right-handed helix of $5-9\,\text{nm}$ diameter [1], and exhibits a typical length of $\sim 5\,\mu m$ [13]. Its persistence length is $\sim 15\,\mu\text{m}$, which is smaller than the typical filament length. F-actin filaments can therefore be seen as a thin and flexible, compared to the rather stiff and cylindrical MT structure (compare Figs. 1.1 and 1.2). The nucleation of F-actin can also be initiated by an increase of the free actin concentration above a critical concentration [1]. As in the case of MTs, there are several proteins, which provide actin nucleation *in vivo*[1]. The Arp2/3-complex resembles the "$-$"-end of an actin filament and serves as a seed for new actin filaments.

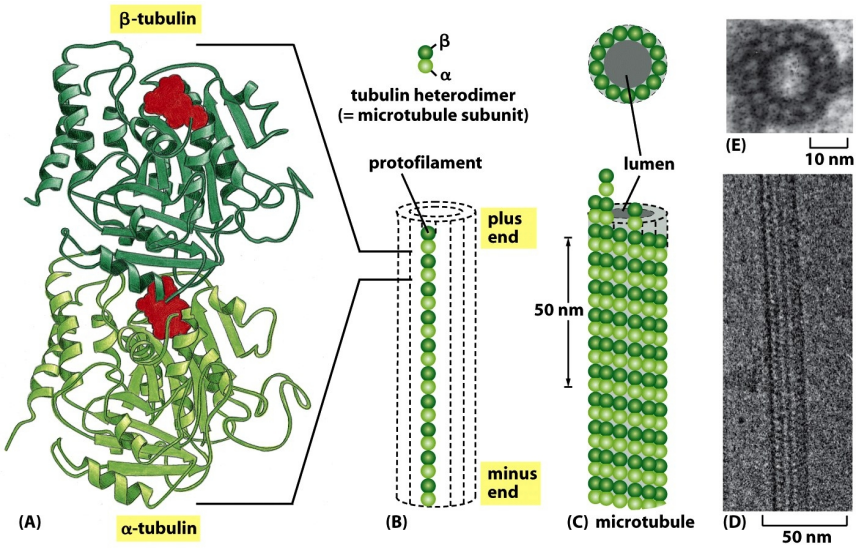

Figure 1.1: The structure of a microtubule and its subunits. (A) The subunit of each protofilament is the tubulin heterodimer, formed by a very tightly linked pair of α- and β-tubulin monomers. The GTP molecule in the α-tubulin monomer is so tightly bound that it can be considered an integral part of the protein. The GTP molecule in the β-tubulin monomer, however, is less tightly bound and has an important role in filament dynamics. Both nucleotides are shown in red. (B) One tubulin subunit ($\alpha - \beta$ heterodimer) and one protofilament are shown schematically. Each protofilament consists of many adjacent subunits with the same orientation. (C) The microtubule is a stiff hollow tube formed from 13 protofilaments aligned in parallel. (D) A short segment of a microtubule viewed in an electron microscope. (E) Electron micrograph of a cross section of a microtubule showing a ring of 13 distinct protofilaments. Picture and caption taken from Ref. [1].

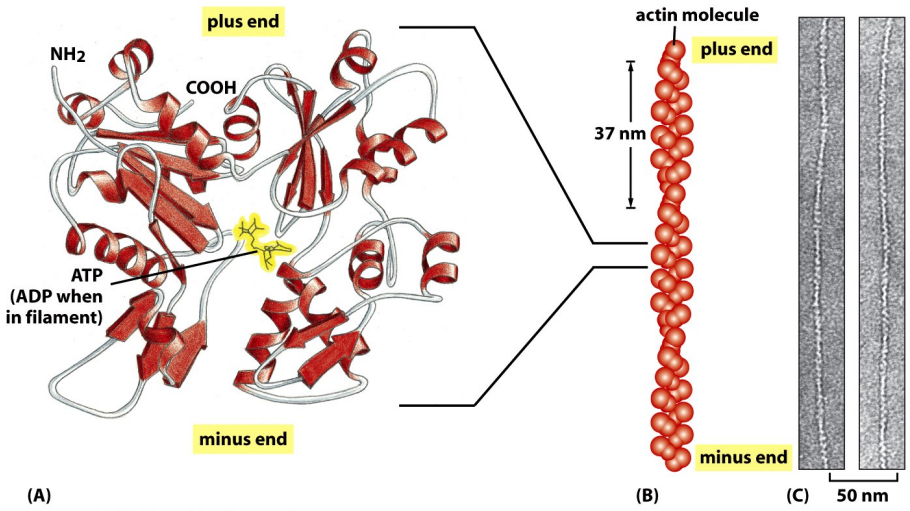

Figure 1.2: The structure of an actin monomer and actin filament. (A) The actin monomer has a nucleotide (either ATP or ADP) bound in a deep cleft in the center of the molecule. (B) Arrangement of monomers in a filament. Although the filament is often described as single helix of monomers, it can be thought of as consisting of two protofilaments, held together by lateral contacts, which wind around each other as two parallel strands of a helix, with a twist repeating every 37 nm. All the subunits within the filament have the same orientation. (C) Electron micrograph of negatively stained actin filaments. Picture and caption taken from Ref. [1].

The Arp2/3 complex also generates a characteristic branching of actin filaments. The branching of actin filaments in the presence of the Arp2/3 complex is explained in more detail later in the text. The Formin-complex actively binds free actin monomers from solution and serves as a nucleation seed [1]. In addition, the Formin-complex remains associated with the "+"-end of the actin filament and supports the incorporation of new actin monomers into the filament. There are no analogues to the Arp2/3 complex and Formin proteins for MTs. Most actin filaments are located close to the cell membrane and form, in cooperation with actin regulation proteins, the cell cortex [1].

The combination of structural polarity, different monomer affinities and hydrolysis of the NTP-nucleotide leads to complex polymerization kinetics of MTs and actin filaments.

For GTP-tubulin in solution hydrolysis proceeds very slow. In filamentous form tubulin acts as a GTPase [3, 14], which catalyzes the hydrolysis of the exchangeable GTP-nucleotide. Within the filament, GTP-tubulin hydrolyzes significantly faster to GDP-tubulin, compared to GTP-tubulin in solution[1]. In the process of hydrolysis, a phosphate group is released from the GTP-nucleotide and the GDP-nucleotide remains bound within the filament. Thus, hydrolysis leads to two different types of filament structures: one consisting of GTP-tubulin and one consisting of GDP-tubulin (see Fig. 1.3).

Since GTP-tubulin shows a higher affinity for the "+"-end of a MT, new GTP-tubulin monomers are primarily incorporated into the "+"-end, compared to the "−"-end. In addition, the "−"-end is often bound to a γ-tubulin complex, which prevents the assembly

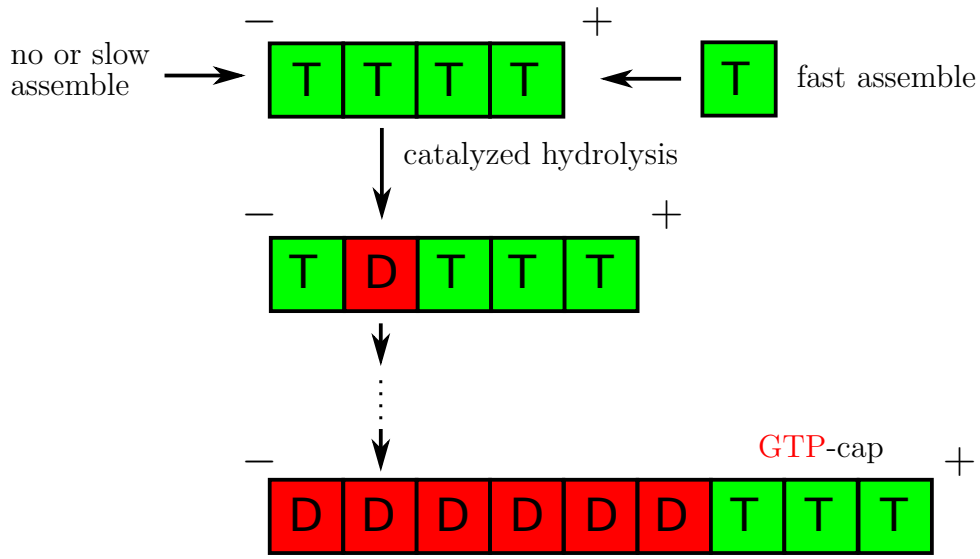

Figure 1.3: Sketch of MT polymerization and hydrolysis of GTP-tubulin. (+): "+"-end of the MT. (-): "−"-end of the MT. T denotes GTP-tubulin monomers (green). D denotes GDP-tubulin monomers (red). From top to bottom: New GTP-tubulin monomers are attached to the "+"-end of the MT with high affinity. No or only few GTP-tubulin monomers are attached to the "−"-end (top). Within the filament, GTP-tubulin is hydrolyzed to GDP-tubulin. Hydrolysis is catalyzed by the GTPase activity of the tubulin monomer (center). As hydrolysis proceeds, only GDP-tubulin remains at the "−"-end of the MT, whereas a cap of GTP-tubulin is formed at the "+"-end (bottom).

of GTP-tubulin monomers into the "−"-end. As hydrolysis proceeds within the filament, the loss of GTP-tubulin at the "+"-end is balanced by new GTP-tubulin from solution, while the amount of GDP-tubulin at the "−"-end increases. This results in a large patch of GDP-tubulin at the "−"-minus end and a patch of GTP-tubulin at the "+"-end, which is often referred as the GTP-cap (see Fig. 1.3). If hydrolysis overtakes the assembly of new GTP-tubulin monomers, the GTP-cap is lost and the whole filament consists of GDP-tubulin only (see Fig. 1.3). The interplay of incorporation of GTP-tubulin, catalyzed hydrolysis and the loss of the GTP-cap causes the characteristic polymerization behaviour of MTs, called *dynamic instability*, which we discuss in greater detail in the following paragraph.

MTs undergo a stochastic transition between periods of moderate growth and fast depolymerization, called dynamic instability [9]. In phases of growth, new GTP-tubulin monomers are incorporated in the "+"-end and the MT growth on average. Depending on the concentration of free tubulin we find growth velocities of up to $\sim 5\,\mu$m/min. Typical values of growth velocities are listed in table A.1. Periods of growth are ended by a complex process called *catastrophe*. Under typical conditions we find a wide range, $(10^{-4} \ldots 10^{-2})\,\mathrm{s}^{-1}$, of catastrophe frequencies [15, 16]. A detailed description of catastrophes follows in the next paragraph. In a period of shrinkage, large parts of single protofilaments curl outwards and depolymerize. The MT rapidly loses length with an

average velocity of $\sim 10\,\mu$m/min and switches back to a period of growth, in a process called *rescue*. Again there is a wide range, $(10^{-2} \dots 10^{-1})\,\mathrm{s}^{-1}$, of rescue frequencies. Typical values of the velocity of shrinkage and the rescue frequency are collected in table A.1. Electron micrographs of a growing and a shrinking MT are shown in Fig. 1.4. In Fig. 1.5 a typical MT length trajectory, obtained from experiments, is shown. It is generally accepted, that the hydrolysis of GTP- to GDP-tubulin within the MT causes dynamic instability. However, the exact mechanism is still subject to ongoing research. In the following, we discuss two possible mechanisms that lead to catastrophes. In a period of growth, new GTP-tubulin monomers are incorporated into the "+"-end of a MT and are hydrolyzed to GDP-tubulin on a characteristic timescale. The characteristic timescale is still not know in detail, but current research suggest values of $\sim 1\,\mathrm{s}$ [7, 17, 18]. Thus a MT consists of a section of GTP-tubulin, located at the "+"-end and called GTP-cap, and a body of GDP-tubulin. In a purely chemical mechanism, bonds between protofilaments are weakened by the hydrolysis of GTP-tubulin, while the remaining GTP-cap stabilizes the MT structure. If the GTP-cap is lost or reduced to a critical size, the MT structure is destabilized, protofilaments begin to depolymerize and a catastrophe is initiated [19]. A sketch of the stabilizing GTP-cap is shown in Fig. 1.4.

Another mechanism leading to catastrophes is based on the *structural plasticity* of the MT lattice [20]. In the context of the structural plasticity mechanism, it is assumed that GDP-tubulin prefers a curved configuration compared to a rather straight configuration of GTP-tubulin. This curvature generates additional stress within the MT. As in the pure chemical mechanism, the GTP-cap stabilizes the MT structure and its loss triggers a catastrophe. However, the kinetics governing the catastrophe mechanism can be complex and are not fully understood. A possible kinetics is the formation of cracks, propagating through the MT lattice. A critical amount of cracks can destabilize the MT structure and initiate a catastrophe [21, 22].

Mechanisms that induce rescue events are less investigated, compared to catastrophe mechanisms. Current research results indicate, that remaining patches of non-hydrolyzed GTP-tubulin within the MT structure can induce rescue events [23, 24]. However, a basic theoretical description of rescue events is still missing.

Dynamic instability is the key player in the spatial and temporal organization of the MT cytoskeleton. In Secs. 1.2 and 1.3 we discuss two representative examples of cellular processes, which are governed by the reorganization of the MT cytoskeleton.

We compare the polymerization dynamics of actin filaments to MT polymerization and, therefore, focus on the "+"-end of an actin filament and do not discuss polymerization kinetics at the "−"-end. The "−"-end of an actin filament can be bound to stabilizing proteins, such like the Arp2/3 complex, and can in such a case be regarded as static. A detailed description of actin polymerization, including polymerization kinetics at both filament ends, can be found in [1] and [2].

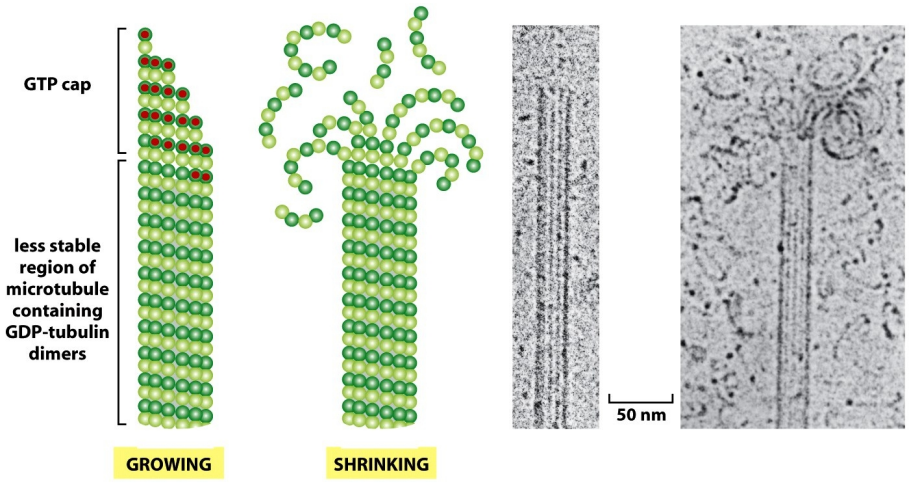

Figure 1.4: In an intact microtubule, protofilaments made from GDP-containing subunits are forced into a linear conformation by many lateral bonds within the microtubule wall, given a stable cap of GTP- containing subunits. Loss of the GTP-cap, however, allows the GDP-containing protofilaments to relax into their more curved conformation.This leads to a progressive disruption of the microtubule. Next to the drawing of a growing and shrinking microtubule, electron micrographs show actual microtubules in each of these two states, as observed in preparation in vitreous ice. Note the particular curling, disintegration GDP-containing protofilaments at the end of the shrinking microtubule. Picture and caption taken from Ref. [1].

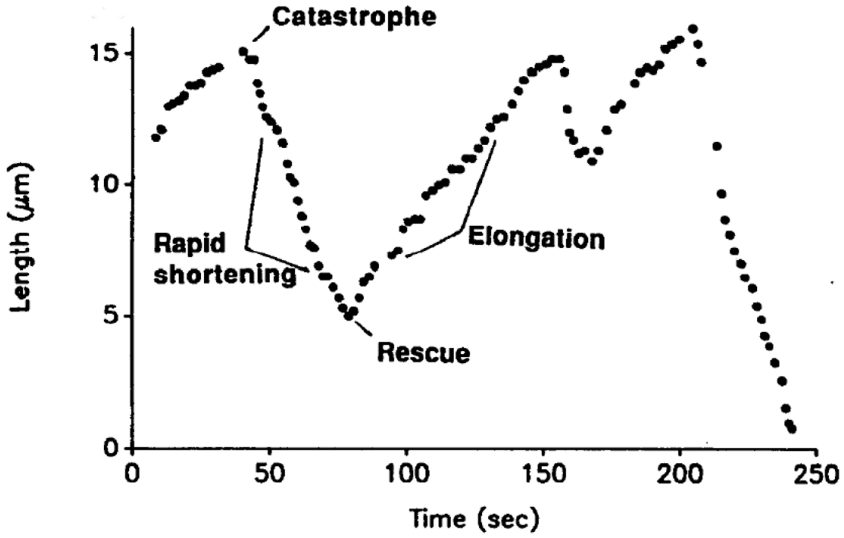

Figure 1.5: Life history of a microtubule undergoing dynamic instability inside a living cell. The rates of growth and rapid shortening are constant for extended periods, and the transitions are abrupt and stochastic. From Cassimeris *et al.* [25]. Picture and caption taken from Ref. [14].

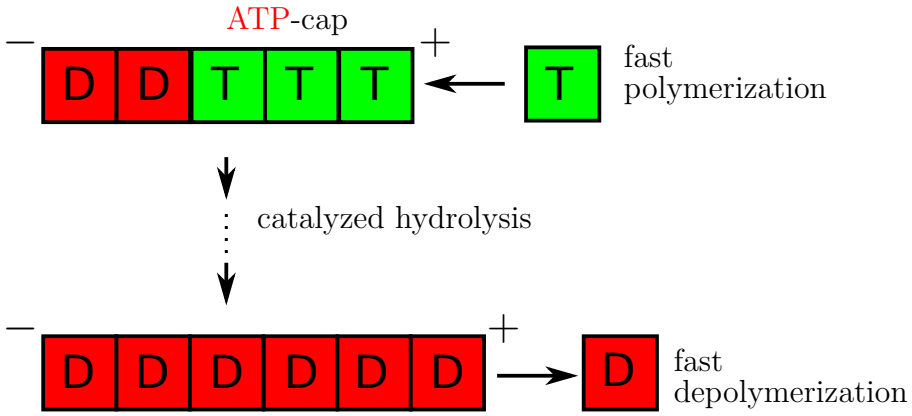

Figure 1.6: Sketch of actin polymerization and hydrolysis of ATP-Actin. (+): "+"-end of the actin filament. (-): "−"-end of the actin filament. T denotes ATP-actin monomers (green). D denotes ADP-actin monomers (red). Top: New ATP-tubulin monomers are attached to the "+"-end of the actin filament and form an ATP-cap, while hydrolysis proceeds within the filament. The actin filament growth on average. Bottom: The ATP-cap is lost and ADP-actin monomers depolymerize from the "+"-end with a high rate. The actin filament shrinks on average.

In filamentous form actin acts as an ATPase and catalyzes the hydrolysis of ATP-actin to ADP-actin. As in the case of MTs, the combination of fast attachment of ATP-actin monomers at the "+"-end and hydrolysis leads to an increase of ADP-actin at the "−"-end and to an ATP-cap at the "+"-end (see Fig. 1.6). If monomer attachment is fast compared to hydrolysis, the actin filament growth on average. We find average growth velocities of $\sim 0.2 \ldots 0.5\,\mu$m/min [2, 26, 27]. If hydrolysis overtakes monomer attachment, the ATP-cap is lost. ADP-actin monomers depolymerize from the "+"-end with a rate of $\sim 7\,\mathrm{s}^{-1}$ and the actin filament begins to shorten [2]. With a monomer size of $\sim 5\,$nm and a depolymerization rate of $\sim 7\,\mathrm{s}^{-1}$, we find an average velocity of shrinkage of $\sim 2\,\mu$m/min [2]. This dynamic transition from average growth to average shrinkage, resembles the dynamic instability of MTs. The loss of the ATP-cap and the subsequent loss of length are similar to MT catastrophes and phases of fast shrinkage. But it should be noted that in the case of actin, single ADP-monomers depolymerize from the "+"-end, whereas in the case of MTs, large parts of protofilaments curl outwards and break into smaller pieces. The underlying mechanism of shrinkage might be different in actin filaments and MTs. Actin filaments do not show rescue events and depolymerize completely. This is another difference to MT dynamical instability, where phases of shrinkage are ended by rescue events.

The MT cytoskeleton and the actin cytoskeleton are both strongly regulated by proteins. There is a multitude of well known regulating proteins. In the following, we focus on proteins which modulate the polymerization kinetics of MTs and actin filaments, and support their spatial arrangement within the cell. The polymerization dynamics of MTs is affected by several regulating proteins. Stathmin proteins bind free GTP-tubulin monomers from

solution and prevent their assembly. As a consequence, the velocity of growth decreases and the catastrophe frequency increases, since no new stabilizing GTP-tubulin monomers are incorporated into the MT-tip [28]. Kinesin-8/-13 proteins (unconventional kinesins) destabilize the "+"-end and induce catastrophes [1, 22, 29]. In contrast, XMAP125 proteins stabilize the "+"-end and accelerate the assembly of new tubulin monomers [1]. Tau and MAP2 proteins bind to the MT and increases the frequency of rescue events (see table A.1). In addition, both proteins support the formation of MT bundles. Along with MTs, MAP2 proteins form bundles of widely spread MTs, whereas Tau proteins promote the formation of closely packed MT bundles. As mentioned above, the γ-tubulin complex serves as a nucleation seed and protects the "$-$"-end against depolymerization. MT regulating proteins modulate basic properties of the dynamic instability, but do not completely suppress the dynamic instability. In addition to MT regulating proteins, chemical drugs are know that influence the polymerization kinetics of MTs. Two examples are nocodazol, which binds tubulin monomers and prevent their incorporation, and taxol, which bind to MTs and stabilizes them. A large list of MT regulating proteins can be found in [1].

Not only MTs are regulated by intracellular proteins, but also the polymerization kinetics of actin filaments. Profilin proteins bind free actin monomers from solution and support their incorporation into the "+"-end of the actin filament. The velocity of growth is increased. In contrast, thymosin proteins bind actin monomers, but prevent assembly. Also Formin proteins, mentioned above, promote the assembly of new actin monomers. Cofilin proteins bind to existing actin filaments and destabilize the filament. The Arp2/3 complex, bound to preexisting actin filaments, nucleates new actin filaments at a 70° angle relative to the original filament. This branching results in a dense, dynamic network of actin filaments. Filamin proteins connect two single actin filaments at a 90° angle, whereas Fimbrin and α-Actinin proteins support the formation of bundles, which consist of parallel actin filaments. A large list of actin regulating proteins can be found in [1].

We now discuss three representative examples for the spatial and temporal organization of polymerizing MTs in a confining environment, the complex interplay of force generation and dynamic instability, and in the case of *in vitro* experiments, the connection to cellular processes.

1.2 Nuclear positioning in fission yeast by dynamic microtubule bundles

The fission yeast *schizosaccharomyces pombe* bacterium exhibits an elliptic form, with a length of $\sim 10\ \mu$m and a width of $\sim 3\ \mu$m. The stiff cell membrane, which can not be deformed by the internal cytoskeleton, encloses a cell nucleus of $\sim 1\mu$m diameter [see Fig. 1.7(a)]. In cell division it is necessary that the cell nucleus maintains its position close to the cell center, since the nucleus determines the future division plane. A deflection from its central position during cell division leads to incomplete chromosome separation and thus to cell death. To ensure a precise positioning of the cell nucleus, *schizosaccharomyces pombe* possesses a repositioning mechanism, based on dynamic MT bundles [30, 31, 32]. Starting from the poles of the nucleus, $3-4$ MT bundles grow along the length axis of the bacterium, directed towards the cell membrane. The bundles consist of $2-3$ MTs with their minus ends connected to a MTOC and their plus ends undergoing dynamic instability (see Fig. 1.7). After a catastrophe, MTs shrink back to the nucleus and are renucleated. Within the bundles, MTs are parallelly arranged and stabilized by MAPS [33], whereas bundles are aligned anti-parallel to each other. If the cell nucleus is displaced from its central position by cell movement or by centrifugation [34], MTs on the deflection side contact the cell membrane before opposing MTs do. Contact MTs polymerize against the cell membrane and generate a force, which drives the nucleus back to its central position [see Fig. 1.7(b)]. Under typical condition MTs do not buckle considerably, so that polymerization can be seen as the only source of force generation. In *in vivo* experiments, MTs push the cell nucleus with a velocity of $\sim 0.5\ \mu$m/min through the cytosol [34], corresponding to a constant force of ~ 1 pN, which can be estimated from Stokes law [35]. In addition, experimental results show a decreased velocity of growth ($\sim 1.3\ \mu$m/min) of pushing MTs compared to force-free growing MTs ($\sim 2\ \mu$m/min) [34, 36]. MTs in contact with the cell membrane also exhibit an increased catastrophe frequency [36], indicating a connection of decreased growth velocity and increased catastrophe frequency. The repositioning is stopped, if the opposing MTs are also in contact with the cell membrane and counterbalance the pushing force. The nucleus is again placed in the center of the cell and undergoes oscillations of small amplitude, caused by MT length fluctuations. The repositioning of the cell nucleus by dynamic MT bundles could also be reproduced in simulations [37]. However, several questions remain to be answered: Do rescue events of single MTs influence the repositioning, although they are not observed in experiments? Do MT bundles generate higher forces? To answer these questions, it is necessary to investigate polymerization dynamics of single MTs and MT bundles in a confining environment and under a resisting force.

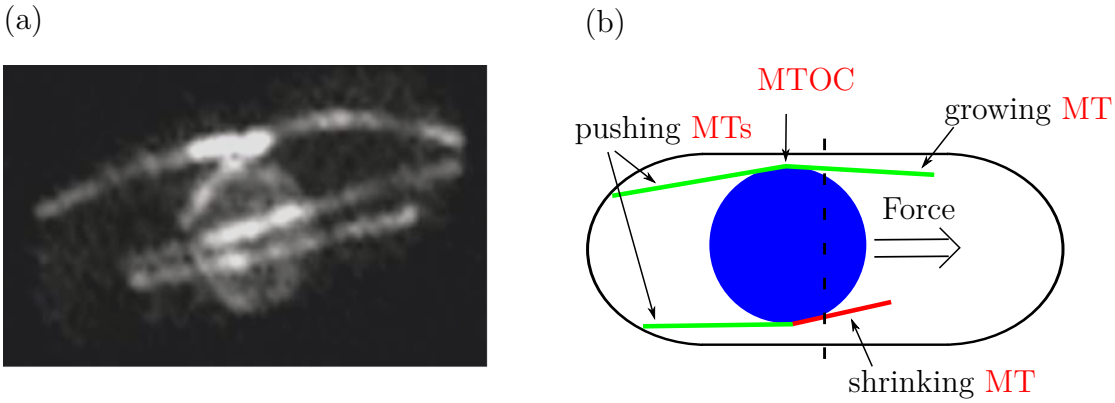

Figure 1.7: (a): Fluorescence microscopy images of schizosaccharomyces pombe. Schizosaccharomyces pombe strain expressing GFP-tubulin and the nuclear pore marker Nup85-GFP. Picture and caption taken from Ref. [37]. (b): Sketch of nuclear positioning mechanism. The dashed black line marks the center of the cell. Polymerizing MTs (green) drive the nucleus (blue) back to its central position. For reasons of clarity, we only show one MT per bundle.

1.3 Membrane deformation by polymerizing microtubules

In vitro polymerizing MTs are able to generate polymerization forces high enough to deform elastic lipid membranes. Fygenson *et al.* investigated the deformation of phospholipid vesicles by enclosed MTs [38]. Tubulin solution is introduced into a vesicle and MT nucleation is initiated by an increase of temperature. Inside the vesicle, $1-3$ MTs polymerize towards the lipid membrane and start to deform the nearly spherical vesicle (diameter $\sim 10\,\mu$m) into an ellipsoid (see Fig. 1.8). As MT polymerization continues, two thin membrane tubes form around the MTs. The vesicle assumes a shape resembling the Greek later ϕ (see Fig. 1.8). Membrane tubes are typically $2-10$ times larger than the initial diameter of the vesicle. For large deformations ($> 20\ \mu$m), Fygenson *et al.* observed MTs buckling under their own polymerization force. After catastrophes, MTs depolymerize completely and the elastic vesicle assumes its initial shape. A shape analysis of the deformed vesicle yields polymerization forces up to $\sim 4\,$pN, which are in the same range as forces generated in fission yeast (see Sec. 1.2). *In vitro*, polymerizing MTs can deform lipid membranes and generate deformations in the μm range. *In vivo*, membrane deformation by polymerizing MTs may play a major role during neuronal outgrowth or in guidance of neuronal growth cones [39, 40]. However, cell membranes are compounds of lipid membranes, membrane proteins, and the underlying cell cortex, and are, in general, less elastic than pure lipid membranes. It remains to be answered, if single MTs can deform cell membranes *in vivo* or if bundles of simultaneously polymerizing MTs are required to generate sufficient forces. In addition, it is unclear if membrane deformation can be regulated by MT growth parameters, like the tubulin concentration. To answer these questions, it is necessary to investigate the force generation of single MTs and MT

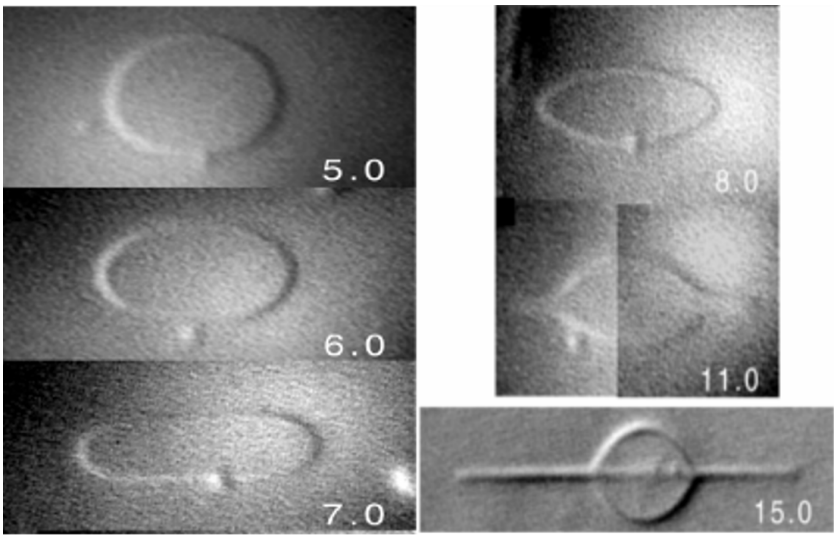

Figure 1.8: A phospholipid vesicle deformed by 1 to 3 microtubules (observed floating freely prior to vesicle deformation). The number at lower right is the length of the long axis in microns. This vesicle fortuitously stuck to the glass slide (spot below center), restricting its rotational diffusion. The final frame has a different vesicle since the other never lay in the focal plane as a ϕ shape. Picture and caption taken from Ref. [38].

bundles, growing against an elastic lipid membrane or, more generally spoken, growing against an elastic obstacle.

1.4 Optical trap experiments on microtubule bundles

We now focus on a special type of *in vitro* experiments, namely optical trap experiments, whose results are the basic motivation for this thesis. In the following we present the fundamental design of optical traps, discuss current research results and illustrate commonalities of experiments with optical traps and theoretical modelling. There is an extensive amount of literature on optical traps. We restrict our discussion on fundamental works and present review articles for further reading [41, 42, 43, 44].

Ashkin *et al.* performed the fundamental works on optical traps in the late 1980s [45] and early 1990s [46]. Optical traps consist of a controllable device of optical lenses, multiple lasers [47] and one or more dielectric particles [48]. The laser light is highly focused and a particle is placed in the focus. The laser light and the particle interact in two different ways [42]. Incident photons transfer momentum to the particle and, according to Newtons law, this momentum transfer results in a force acting on the particle. This force is termed *scattering force*. The scattering interaction and the dipole interaction generate a harmonic potential, in which the focus corresponds to the potential minimum. The dielectric particle is soundly trapped within the harmonic potential, with the minimum of the harmonic potential, i.e. the focus, as its equilibrium position. If the particle is

deflected from its equilibrium position, or if the position of the focus is changed by the controllable lens system, the harmonic potential exerts a resiting force, directed towards the focus. The resisting force increases linear with the displacement distance from the focus. Its amplitude is determined by the steepness of the harmonic potential. The fundamental properties of the harmonic potential, like its steepness or its spatial extent, can be adjusted by varying the intensity of the laser light or the spatial form of the focus. This allows a precise force control. Common realizations are approximately constant forces and spring-like elastic forces, linearly increasing with the displacement distance from the focus [17]. In experiments the steepness of the harmonic potential is determined from fluctuations of the dielectric particle around its equilibrium position. The displacement distance of the particle from its equilibrium position and its return dynamics can be measured with high accuracy. Spatial and temporal resolutions of current optical traps are in the range of nanometers and microseconds [43].

Optical traps are widely used to study the effect of in- or external forces in biological processes. They are successfully applied to the investigation of force generation by molecular motors [49], folding kinetics of RNA [50] or polymerization kinetics of biopolymers [51]. In the following we focus on experiments on MTs [17, 52], and in particular on the force generation by MT bundles [53].

In optical trap experiments on MTs, a MT seed is attached to a silica bead. The bead is placed in a microchamber and trapped in the focus of the optical trap [see Fig. 1.9(a)]. When GTP-tubulin solution is introduced, the MT starts to polymerize until its tip reaches a wall of the microchamber. The polymerizing MT now deflects the bead from its equilibrium position. The displacement is measured and offers valuable information on the current MT length, the incorporation dynamics of new monomers [17, 52], its velocity of growth and on the magnitude of the polymerization force, generated by the MT [17]. The MT polymerizes until its growth is stalled by the resisting force or a catastrophe occurs. In general, no rescue events are observed in this type of experiments and the experiment must be restarted with a new MT seed. Both the stall force and the time spent in the growing state, that is the time spent polymerizing against the resisting force, are fundamental quantities. They contain detailed information on force-velocity relations and on mechanisms that lead to catastrophes [17].

Only recently it became possible to study bundles of parallelly growing MT in optical traps [53]. Laan *et al.* investigated the force generation by bundles of parallel MTs growing simultaneously against an elastic force, realized by an optical trap [see Fig. 1.9(b)]. The experiments by Laan *et al.* yield two main results:

- Polymerizing MT bundles generate considerably higher forces, compared to a single MT. Laan *et al.* showed that the polymerization force of a MT bundle growths strictly linear in the number of MTs within the bundle, so that N MTs produce the N-fold polymerization force of a single MT under same experimental conditions.

At a tubulin concentration of $\sim 25\ \mu$M, Laan *et al.* found a polymerization force of ~ 2.7 pN for a single MT. Under the same experimental conditions, two MTs generated a polymerization force of ~ 5.5 pN and three MTs ~ 8.1 pN, which are approximately multiples of ~ 2.7 pN. The force was shared equally between all MTs within the bundle.

- During the experiments Laan *et al.* observed cooperative dynamics within the MT bundle, so called *collective catastrophes*. At forces close to the maximal polymerization force of the bundle, a catastrophe of a single MT lead to a cascade of catastrophes. The force acting on the remaining MTs was increased and within no time, each MT within the bundle switched into a state of shrinkage and the whole bundle entered a state of collective shrinkage. Laan *et al.* termed this collective behaviour a collective catastrophe.

In stochastic simulations, both the linear dependence of the polymerization force on the MT number and collective catastrophes could be reproduced by Laan *et al.* However, in the performed simulations Laan *et al.* used an artificially increased catastrophe rate and investigated a rather small set of parameter values. In addition an underlying theoretical description of MT-bundle polymerization dynamics is still missing.
We establish a detailed theoretical model for the cooperative polymerization dynamics of MT bundles growing against an elastic force. The presented model reproduces experimental results, puts them on a solid theoretical basis and allows us to investigate a wide set of parameters. We also include rescue events, which have not been considered by Laan *et al.* Rescue events of single MTs lead to a new type of collective behaviour, so called *collective rescues* [54]. Although rescue events have not been observed in optical trap experiments so far, they play a crucial role *in vivo* and due to continuous improvements of experimental techniques, it is only a matter of time until rescue events become accessible in optical trap experiments.
The last paragraph illustrates another advantage of experiments with optical traps. This type of experiment is performed under well controlled experimental conditions and can easily be reproduced. In addition, the composition of optical trap experiments can be reduced down to basic components, like a rigid wall or a spring-like resisting force. These basic components can be described by theoretical models, without too much computational effort. On the other hand optical trap experiments can be designed according to basic theoretical models and offer a good approach to merge theoretical modelling and *in vitro* experiments.

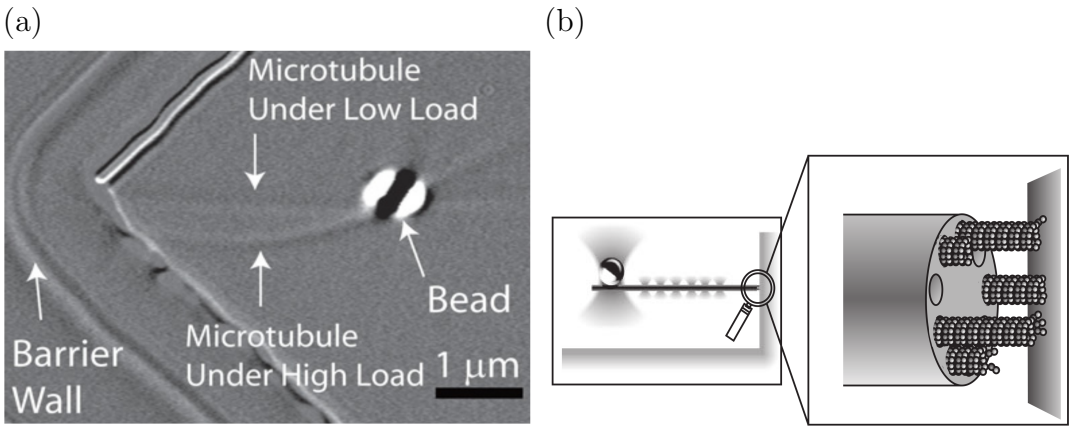

Figure 1.9: (a) Differential-interference-contrast micrograph of an experiment showing the bead, microtubule, and barrier. Picture and caption taken from Ref. [17]. (b) Schematic picture of a MT bundle nucleated by an axoneme growing against a barrier. A construct made of a bead attached to the axoneme is maintained in position by a "keyhole" trap: A single strong trap holds the bead while many shallow traps form a line trap constraining the axoneme's movement along a single direction. Picture and caption taken from Ref. [53].

Chapter 2

Coarse-grained microtubule model [1]

In this chapter we present a coarse-grained single MT model, which includes the dynamic instability and introduce the basic notation. Section 2.1 deals with single MT dynamics in the absence of force. In Section 2.2 the polymerization velocity under an opposing force is discussed, based on the *Brownian ratchet model* and is compared to a more generalized force-velocity relation by Kolomeisky *et al.* In Section 2.3 we first introduce the cooperative catastrophe model by Flyvbjerg *et al.* in the absence of force. Later the catastrophe rate is connected to an opposing force via the force-velocity relation (see Sec. 2.2). In addition, we present a catastrophe model based on experimental data, and a linear catastrophe model. Their differences and similarities are discussed.

2.1 Single microtubule dynamics

The MT dynamics in the presence of its dynamic instability is described in terms of probability densities and switching rates [56, 57]. In the growing state, a MT polymerizes with average velocity v_+. Typically we find $v_+ = (0.7-8)\times 10^{-8}\,\mathrm{m/s} = (0.4-5)\,\mu\mathrm{m/min}$ (Table A.1). The MT stochastically switches from a state of growth $(+)$ to a state of shrinkage $(-)$ with the catastrophe rate ω_c. In the shrinking state, it rapidly depolymerizes with an average velocity $v_- \simeq 3\times 10^{-7}\,\mathrm{m/s}$ (Table A.1). With the rescue rate ω_r the MT stochastically switches from a state of shrinkage back to a state of growth. We model catastrophes and rescues as Poisson processes such that $\langle\tau_+\rangle = 1/\omega_\mathrm{c}$ and $\langle\tau_-\rangle = 1/\omega_\mathrm{r}$ are the average times spent in the growing and shrinking states, respectively.

The stochastic time evolution of an ensemble of independent MTs, growing along the x-axis, can be described by two coupled master equations for the probabilities densities $p_+(x,t)$ and $p_-(x,t)$ of finding a MT with length x at time t in a growing or shrinking

[1] Parts of the text have been published in reference [55] and are ©2012 American Physical Society. http://publish.aps.org/copyrightFAQ.html

state,

$$\partial_t p_+(x,t) = -\omega_c p_+(x,t) + \omega_r p_-(x,t) - v_+ \partial_x p_+(x,t) \tag{2.1}$$

$$\partial_t p_-(x,t) = \omega_c p_+(x,t) - \omega_r p_-(x,t) + v_- \partial_x p_-(x,t). \tag{2.2}$$

In the following, we will always use a reflecting boundary at $x = 0$: A MT shrinking back to zero length undergoes a forced rescue instantaneously. This corresponds to

$$v_+ p_+(0,t) = v_- p_-(0,t). \tag{2.3}$$

A more refined model including a nucleating state, instead of a reflecting boundary condition at $x = 0$, has been considered in ref. [58]. For a constant and fixed catastrophe rate ω_c, eqs. (2.1) and (2.2), together with the boundary condition (2.3), can be solved analytically on the half-space $x > 0$, and we can determine the overall probability density function (OPDF) of finding a MT with length x at time t, $P(x,t) \equiv p_+(x,t) + p_-(x,t)$ [56, 57]. The solution exhibits two different phases: a phase of bounded growth and a phase of unbounded growth.

In the phase of bounded growth the average length loss during a period of shrinkage, $v_- \langle \tau_- \rangle = v_-/\omega_r$, exceeds the average length gain during a period of growth, $v_+ \langle \tau_+ \rangle = v_+/\omega_c$. The steady-state solution of $P(x,t)$ assumes a simple exponential form $P(x) = |\lambda|^{-1} e^{-x/|\lambda|}$ with an average length $\langle x \rangle = |\lambda|$ and a characteristic length parameter

$$\lambda \equiv \frac{v_+ v_-}{v_+ \omega_r - v_- \omega_c}, \tag{2.4}$$

with $\lambda^{-1} < 0$ for bounded growth [56]. The transition to the regime of unbounded growth takes place at $\lambda^{-1} = 0$, where the average length gain during growth equals exactly the average length loss during shrinkage,

$$v_+ \omega_r = v_- \omega_c, \tag{2.5}$$

such that $\langle x \rangle$ diverges.

In the regime of unbounded growth with $\lambda > 0$, the average length gain during a period of growth is larger than the average length loss during a period of shrinkage. There is no steady state solution, and for long times $P(x,t)$ asymptotically approaches a Gaussian distribution

$$P(x,t) \approx \frac{1}{2\sqrt{\pi D_J t}} \exp\left[-\frac{(x - Jt)^2}{4 D_J t} \right] \tag{2.6}$$

centered on an average length which approaches linear growth $\langle x \rangle \approx Jt$ with a mean

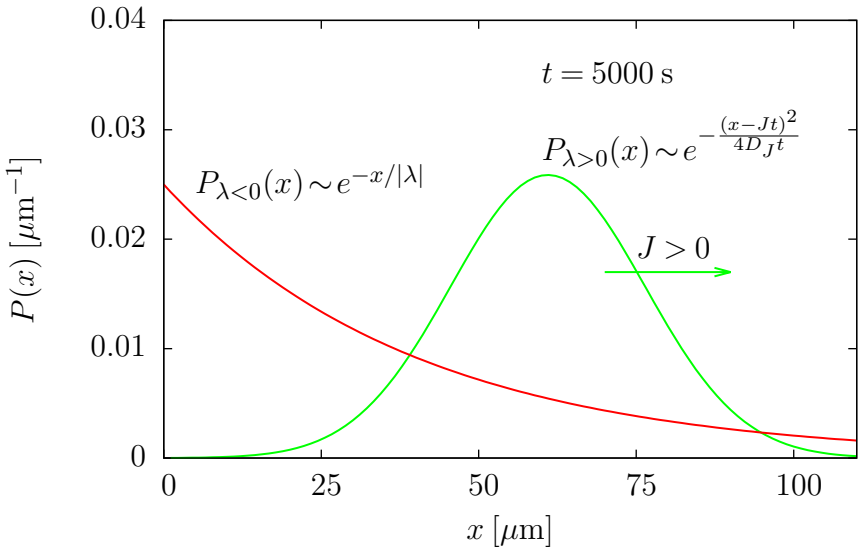

Figure 2.1: OPDF $P(x,t) = p_+(x,t) + p_-(x,t)$ as solution of eqs. (2.1) and (2.1). Red line: Steady-state OPDF $P(x)$ for bounded growth. We set $v_+ = 2 \times 10^{-8}$ m/s, $v_- = 3 \times 10^{-7}$ m/s, $\omega_c = 0.0025$ s^{-1}, and $\omega_r = 0.05$ s^{-1}, corresponding to a characteristic length parameter $\lambda \approx -4 \times 10^{-5}$ [eq. (2.4)]. Green line: OPDF $P(x,t)$ for unbounded growth and $t = 3600$ s from eq. (2.6). We set $v_+ = 2 \times 10^{-8}$ m/s, $v_- = 3 \times 10^{-7}$ m/s, $\omega_c = 0.0025$ s^{-1}, and $\omega_r = 0.1$ s^{-1}, corresponding to an average growth velocity $J \approx 1.2 \times 10^{-8}$ m/s [eq. (2.7)].

velocity J and with diffusively growing width $\langle x^2 \rangle - \langle x \rangle^2 \approx 2 D_J t$ with a diffusion constant D_J [56, 57].

The average growth velocity is given by

$$J = \frac{v_+ \omega_r - v_- \omega_c}{\omega_r + \omega_c} \tag{2.7}$$

because the asymptotic probabilities to be in a growing or shrinking state are $\pi_+ = \omega_r/(\omega_c + \omega_r)$ and $\pi_- = \omega_c/(\omega_c + \omega_r)$, respectively. The diffusion constant D_J is

$$D_J = \frac{\omega_c \omega_r (v_+ + v_-)^2}{(\omega_c + \omega_r)^3}. \tag{2.8}$$

The transition between the two growth phases can be achieved by changing one of the four parameters of MT growth, ω_c, ω_r, v_+, or v_-. In the following, we will use catastrophe models, where the catastrophe rate ω_c is a function of the growth velocity v_+, which in turn is determined by the GTP-tubulin concentration via the GTP-tubulin on-rate ω_{on} (assuming a fixed off-rate ω_{off}). Moreover, experimental data suggest that v_- is fixed to values close to $\sim 10^{-7}$ m/s (Table A.1). As a consequence, there are two tunable control parameters left, the GTP-tubulin concentration or, equivalently, the tubulin on-rate ω_{on} and the rescue rate ω_r.

These are the control parameters we will explore for single MT dynamics in the context

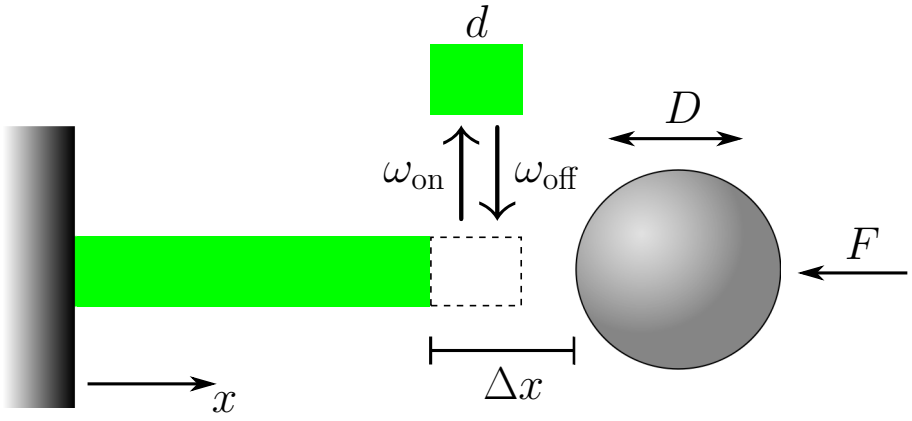

Figure 2.2: Sketch of the Brownian ratchet model. A single MT (green) polymerizes along the x-axis under an opposing force F, with GTP-tubulin on-rate ω_{on} and GTP-tubulin off-rate ω_{off}. The particle diffuses freely along the x-axis with diffusion coefficient D. A new GTP-tubulin dimer is incorporated into the MT tip, only if a gap of size $\Delta x = d$ is created by the diffusing particle.

of this thesis.

These parameters are also targets for regulation by MAPS, such as OP18/stathmin, which reduces ω_{on} by binding to GTP-tubulin dimers [28] or MAP4, which increases the rescue rate ω_r [59] (see Sec. 1.1).

Typical values for MT growth parameters can be found in appendix A, Table A.1.

2.2 Force-dependent growth velocity

In a growing state, GTP-tubulin dimers are attached to any of the 13 protofilaments with the GTP-tubulin on-rate ω_{on}, which is directly related to the GTP-tubulin concentration. We explore a regime $\omega_{on} = 30, ..., 100\,s^{-1}$, see Table A.1. GTP-tubulin dimers are detached with the rate $\omega_{off} = 6\,s^{-1}$ [60] such that we can typically assume $\omega_{on} \gg \omega_{off}$.

In the absence of force or restricting boundaries, the average velocity of growth is given by

$$v_+(0) = d\,(\omega_{on} - \omega_{off})\,. \tag{2.9}$$

Here d denotes the effective dimer size $d \approx 8\text{nm}/13 \approx 0.6\,\text{nm}$.

To include force generation by polymerizing MTs into the coarsed-grained single MT model, we introduce a special mechanism, the *Brownian ratchet model*, which couples MT polymerization to force generation [61]. A sketch of the Brownian ratchet model is presented in Fig. 2.2.

A single MT polymerizes in x-direction. A particle, which undergoes diffusive motion with diffusion coefficient D, is placed in front of the MT. F is an opposing force and acts along the x-axes. The diffusive motion of the particle generates a gap of size Δx between the MT tip and the particle surface. Only if the gap size equals the size of a dimer, thus $\Delta x = d$, a new dimer can be incorporated into the MT tip. Then the

MT elongation is governed by the GTP-tubulin on-rate ω_{on} and the diffusion coefficient D of the particle. Depending on the ration $2D/(\omega_{\text{on}}d^2)$ we can distinguish to cases:

diffusion-limited-polymerization: $2D/(\omega_{\text{on}}d^2) \ll 1$
In the diffusion-limited case the average time to diffuse a distance d, $2D/d^2$, is small compared to the inverse GTP-tubulin on-rate ω_{on}^{-1}. The inverse GTP-tubulin on-rate ω_{on}^{-1} is larger than the average time it takes the particle take to diffuse a distance $\Delta x = d$ under an opposing force F. As soon as a gap of size $\Delta x = d$ is created by the diffusing particle, a GTP-tubulin dimer drops in and is incorporated into the MT tip. The inverse GTP-tubulin on-rate ω_{on}^{-1} nearly equals the average time the particle take to diffuse a distance $\Delta x = d$ under an opposing force F. This is a mean-first passage time problem, and can analytically be treated in the context of Kramers rate theory [62, 63]. Detailed calculations can be found in various textbooks [2, 62, 63], so we restrict our discussion to the final result, the growth velocity $v_+(F)$ under force. We find

$$v_+(F) \cong \frac{D}{d}\left(\frac{Fd}{k_{\text{B}}T}\right)^2 \left[\exp\left(Fd/k_{\text{B}}T\right) - 1 - \left(Fd/k_{\text{B}}T\right)\right]^{-1}. \tag{2.10}$$

The growth velocity is a linear function of the diffusion coefficient and is independent of the GTP-tubulin on-rate. For small forces, $Fd/(k_{\text{B}}T) \ll 1$, v_+ approaches $v_+ \approx 2D/d = \text{const}$. The diffusion coefficient can be calculated from the Einstein relation and Stokes law, and is given by $D = k_{\text{B}}T/(6\pi\eta r)$ [2]. Here r is the radius of the spherical particle and η the dynamic viscosity of water. In optical trap experiments we typically have $r = 1\,\mu\text{m}$ [47, 48], $\eta = 10^{-3}\,\text{Ns/m}^2$, $T = 300\,\text{K}$ and we find $2D/(\omega_{\text{on}}d^2) \approx 10^4 - 10^5 \gg 1$ for $\omega_{\text{on}} = (10 - 100)\,\text{s}^{-1}$. The condition of diffusion-limited-polymerization is not fulfilled under typical experimental conditions. We, therefore, focus on the cases $2D/(\omega_{\text{on}}d^2) \gg 1$, the reaction-limited-polymerization.

reaction-limited-polymerization: $2D/(\omega_{\text{on}}d^2) \gg 1$
In the reaction-limited case, the diffusion coefficient is very large. The particle is in thermal equilibrium with its surrounding and the gap size Δx explores all possible positions. A new GTP-tubulin dimer is only seldom attached to the MT tip and the probability to find a gap of size Δx follows a Boltzmann distribution $p(\Delta x) \sim \exp\left(\Delta x F/k_{\text{B}}T\right)$. Since a new GTP-tubulin dimer can only be incorporated into the MT tip if $\Delta x = d$, the GTP-tubulin on-rate is modified by an additional Boltzmann factor and the force-dependent growth velocity becomes:

$$v_+(F) = d\left[\omega_{\text{on}} \exp\left(-Fd/k_B T\right) - \omega_{\text{off}}\right]. \tag{2.11}$$

Here Fd is the work that has to be done against the force F to incorporate a single GTP-tubulin dimer of size d; k_B is the Boltzmann constant and $T = 300$ K the temperature.

Equation (2.11) can explicitly be shown by establishing reaction-diffusion equations for the gap size Δx [2, 61]. In the reaction-limited case, their solution is given by eq. (2.11). In the following we use the dimensionless force

$$\eta \equiv F/F_0 \quad \text{with} \quad F_0 = k_B T/d, \tag{2.12}$$

in terms of which the force-dependent growth velocity is given by

$$v_+(\eta) = d\left[\omega_{\text{on}} e^{-\eta} - \omega_{\text{off}}\right]. \tag{2.13}$$

The characteristic force F_0 has a value $F_0 = k_B T/d \approx 7\,\text{pN}$. In experiments a characteristic force $F_0 \approx 0.8\,\text{pN}$ has been measured [53]. It is still unknown what causes the difference between theoretical and experimentally measured values. Throughout this thesis we will use $F_0 \approx 7\,\text{pN}$, unless we compare our theoretical results with experimentally measurements by Laan *et al.*[53]. In this case we will present results for $F_0 \approx 7\,\text{pN}$ and the experimental measured value $F_0 \approx 0.8\,\text{pN}$.

The dimensionless stall force

$$\eta_{\text{stall}} = \ln\left(\omega_{\text{on}}/\omega_{\text{off}}\right) \tag{2.14}$$

is defined by the condition of vanishing growth velocity $v_+(\eta_{\text{stall}}) = 0$. We typically have $\eta_{\text{stall}} \simeq 1.5, ..., 3$ or $F_{\text{stall}} \simeq 10, ..., 20\,\text{pN}$ for $\omega_{\text{on}} = 30, ..., 100\,\text{s}^{-1}$. The stall force is the maximal force that the MT can generate in the *absence* of catastrophes. In the context of this thesis, we will investigate how the forces that can be generated in the presence of the dynamic instability compare to this stall force.

There are further models, which connect the polymerization velocity v_+ to a resisting force F [64, 65, 66]. However, most of these different approaches yield no *explicit* force-velocity relations, and can not directly be used for further calculations. Furthermore, the Brownian ratchet model resembles the basic setting of current optical trap experiments [17, 52, 53]. Therefore, we will focus on the Brownian ratchet model, and the reaction-limited case. In addition, we will show later, that our results do not qualitatively change, if a more generalized force-velocity relation, outlined in the next paragraph, is employed. In their investigation of experimental data Kolomeisky *et al.* used the generalized growth velocity

$$v_+(\eta, \theta) = d\left\{\omega_{\text{on}} \exp\left(-\theta\eta\right) - \omega_{\text{off}} \exp\left[(1-\theta)\,\eta\right]\right\}, \tag{2.15}$$

which depends on the dimensionless "load distribution factor" θ [67]. The load distribution factor $\theta \in [0, 1]$ determines whether the on- or off-rates are affected by external force, while keeping the ratio of overall on- and off-rate unaffected. Under force both the tubulin on-rate ω_{on} and the tubulin off-rate ω_{off} now acquire an additional Boltzmann-like factor. For $\theta = 1$, we obtain again $v_+(\eta)$ as given by eq. (2.13). The dimensionless stall force is

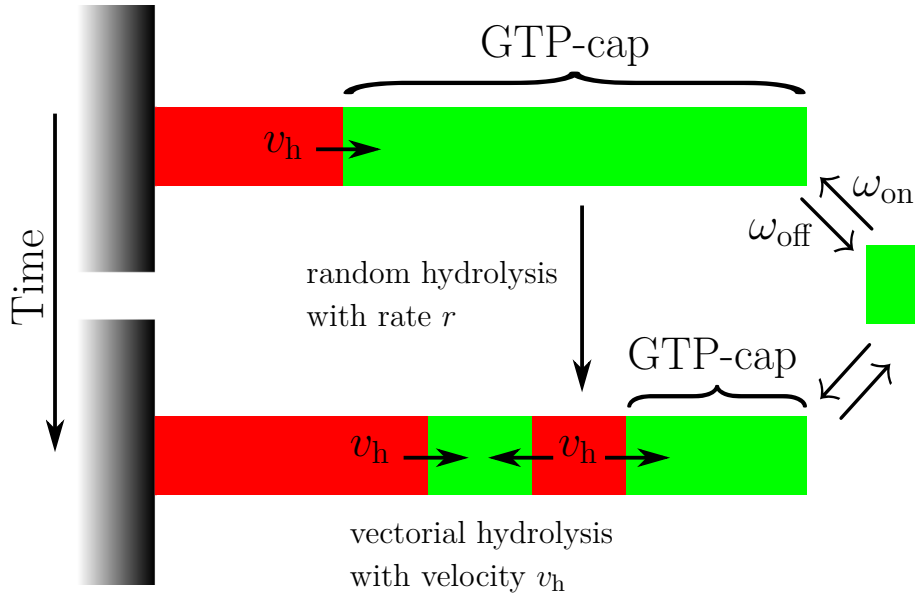

Figure 2.3: Sketch of the cooperative hydrolysis model by Flyvbjerg *et al.* New GTP-tubulin dimers attach/detach to the MT tip with rate ω_{on} and ω_{off} respectively. In random hydrolysis GTP-tubulin (green) stochastically hydrolyzes to GDP-tubulin (red) with rate r. In vectorial hydrolysis GTP-tubulin with adjacent GDP-tubulin hydrolyzes and hydrolysis fronts move through the MT with average velocity v_h. A catastrophe is initiated when the GTP-cap reaches zero length.

unaffected by θ and is still given by $\eta_{stall} = \ln(\omega_{on}/\omega_{off})$.

2.3 Force-dependent catastrophe rate

In this thesis, we focus on purely chemical catastrophe events (see Sec. 1.1), where catastrophes are initiated by the loss of the stabilizing GTP-cap, and in particular on the cooperative hydrolysis model proposed by Flyvbjerg *et al.* [18, 68]. We will not discuss more elaborate multistep catastrophe models [29, 69, 70], nor include aspects of "structural plasticity" into the description [20]. Within this model, GTP-tubulin is hydrolyzed by a combination of random and vectorial hydrolysis. A similar cooperative model has recently been proposed for the hydrolysis dynamics of F-actin [27, 71].

In the following we present a detailed description of the catastrophe model by Flyvbjerg *et al.* in the absence of force. Later we connect the resulting catastrophe rate to an opposing force.

We consider a section of a single MT, consisting entirely of GTP-tubulin and located at the plus end of the growing MT. In the following this section is called GTP-cap. New GTP-tubulin dimers are attached to the GTP-cap with GTP-tubulin on-rate ω_{on}, which is connected to the growth velocity v_+ via eq. (2.9). In *random* hydrolysis, GTP-tubulin is stochastically hydrolyzed to GDP-tubulin with a rate $r \sim 3.7 \times 10^6\,\mathrm{m^{-1}s^{-1}}$ at a random site within the GTP-cap. The cap is split up into a new cap and a remaining fraction of

GTP-tubulin, now located at the interior of the MT (see Fig. 2.3). In a second hydrolysis mechanism, called *vectorial* hydrolysis, only GTP-tubulin with adjacent GDP-tubulin is hydrolyzed. This results in hydrolysis fronts, propagating, through the GTP-cap and the remaining fraction of GTP-tubulin, with average velocity $v_\mathrm{h} \sim 4.2 \times 10^{-9}\,\mathrm{m/s}$.

Since the remaining fraction of GTP-tubulin is hydrolyzed from both sides and no GTP-tubulin can be added to this part of the MT, it disappears fast compared to the new GTP-cap. In contrast the GTP-cap growth with average velocity $v = v_+ - v_\mathrm{h}$. A catastrophe is initiated when the stabilizing GTP-cap vanishes, that is its length is decreased down to zero. The cap length is stochastically reduced by fluctuation, caused by *random* hydrolysis, and negative average velocity $v = v_+ - v_\mathrm{h} < 0$. Within the cooperative hydrolysis model, the inverse catastrophe rate ω_c^{-1} is given by the mean first-passage time (MFPT) to the state of zero cap length.

We provide an analytical expression for the MFPT in the state of vanishing cap length, as a function of the hydrolysis parameters r and v_h, and the growth velocity v_+, strictly following references [68] and [18].

The stochastic time evolution of an ensemble of independent GTP-caps is described by a linear master equation for the probability density $p(x,t)$ to find a GTP-cap of length x at time t

$$\partial_t p(x,t) = \partial_x j(x,t) \tag{2.16}$$

with

$$j(x,t) = vp(x,t) - D\partial_x p(x,t) - rxP(x,t). \tag{2.17}$$

Here rx denotes the rate with which GTP-caps are split up into two new fragments, $vp(x,t)$ the average elongation rate and $D\partial_x p(x,t)$ the rate with which the cap length is changed by fluctuations, parametrized by the diffusion coefficient $D = 0.5d(v_+ + v_\mathrm{h})$. The number of GTP-caps of length longer than x at time t is

$$P(x,t) = \int_x^\infty p(x,t)dx \tag{2.18}$$

and $P(0,t)$ the overall number of GTP-caps at time t. From eq. (2.16) we find

$$\partial_t P(0,t) = j(0,t) = vp(0,t) - D\partial_x p(0,t). \tag{2.19}$$

Since $p(x,t) = 0$ for $x < 0$ the boundary condition at $x = 0$ reads $p(0^+,t) = 0$ and the catastrophe rate ω_c, that is the temporal alteration of the total number of GTP-caps based on the overall number of GTP-caps within the ensemble, is than given by

$$\omega_\mathrm{c} \equiv -\frac{\partial_t P(0,t)}{P(0,t)} = \frac{D\partial_x p(0,t)}{P(0,t)}. \tag{2.20}$$

To obtain an explicit expression for the catastrophe rate ω_c, $P(0,t)$ and $\partial_t P(0,t)$ have

to be determined. Therefore eq. (2.16) is integrated on the interval $x \in [0,\infty[$. Since $j(\infty,t) = 0\ \forall t$ this results in

$$\partial_t P(x,t) = \left(-v\partial_x + D\partial_x^2 - r\right) P(x,t). \tag{2.21}$$

Introducing

$$x_0 \equiv (D/r)^{1/3} \tag{2.22}$$

$$t_0 \equiv \left(Dr^2\right)^{-1/3} \tag{2.23}$$

$$\gamma \equiv \frac{v}{2D^{2/3}r^{1/3}} = \frac{vt_0}{2x_0} \tag{2.24}$$

and the dimensionless variables

$$\xi \equiv x/x_0 \tag{2.25}$$

$$\tau \equiv t/t_0 \tag{2.26}$$

$$\widetilde{P}(\xi,\tau) \equiv \exp\left[-vx/(2D)\right] P(x,t) = \exp\left(-\xi\gamma\right) P(x,t) \tag{2.27}$$

we find

$$\partial_\tau \widetilde{P}(\xi,\tau) = \left(\partial_\xi^2 - \xi - \gamma^2\right) \widetilde{P}(\xi,\tau). \tag{2.28}$$

Equation (2.28) is a linear partial differential equation and is solved by separation of variables. The same type of partial differential equation describes the dynamics of a quantum mechanical particle in an electric field [72]. Its general solution is

$$\widetilde{P}(\xi,\tau) = \int d\alpha\ c(\alpha) \exp\left(-\alpha\tau\right) Ai\left(\xi + \gamma^2 - \alpha\right), \tag{2.29}$$

where $Ai(x)$ is the first Airy function [73, 74], α the separation constant and $c(\alpha)$ a coefficient function. Both, α and $c(\alpha)$, have to be determined from boundary conditions. With $p(0,t) = \partial_x P(0,t) = 0$ and eqs. (2.25) and (2.27) we obtain

$$\int d\alpha\ c(\alpha) \exp\left(-\alpha\tau\right) \left[\gamma Ai\left(\gamma^2 - \alpha\right) + Ai'\left(\gamma^2 - \alpha\right)\right] = 0 \tag{2.30}$$

from eq. (2.29).

Here $Ai'(x)$ denotes the first derivative of $Ai(x)$ with respect to x. From eq. (2.30) follows that $c(\alpha)$ is only nonzero for a discrete set of values α_k, $k = 0,1,2,\dots$, which are subject to the condition

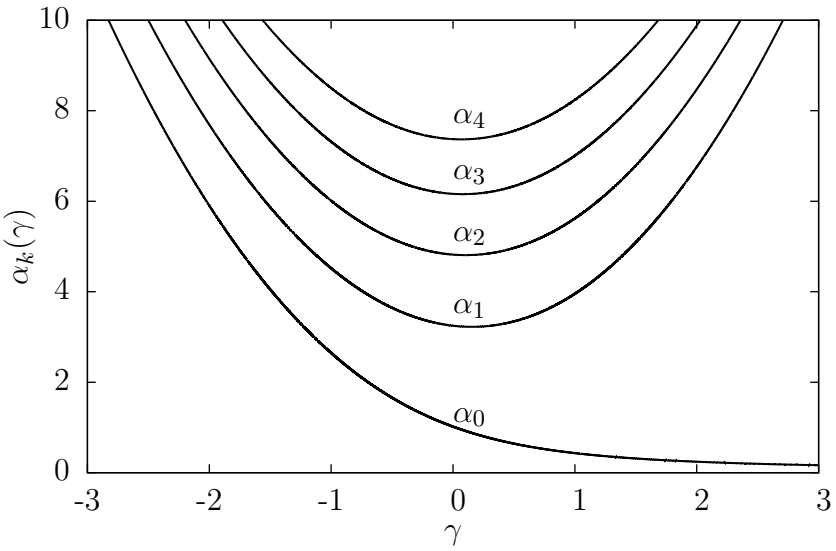

Figure 2.4: First five graphs of $\alpha_k(\gamma)$ for $k = 0, 1, 2, 3, 4$ as a function of γ.

$$\gamma = -\frac{Ai'\left(\gamma^2 - \alpha_k\right)}{Ai\left(\gamma^2 - \alpha_k\right)}. \tag{2.31}$$

Equation (2.31) is solved numerically for different values of γ. Here we want to point out, that $\gamma = \gamma(v_+)$ is a function of the growth velocity v_+ [see eq. (2.24)]. All further calculations can also be performed in terms of v_+. However, we maintain the notation by Flyvbjerg *et al.* to simplify further calculations. The first five graphs of $\alpha_k = \alpha_k(\gamma)$ are depicted in Fig. 2.4, as a function of γ.

We find $\alpha_k(\gamma) < \alpha_{k+1}(\gamma)$ for a fixed γ and $\alpha_0(\gamma) \ll \alpha_k(\gamma)$ $\forall k$ for $\gamma \geq 1$. The set of functions $Ai\left(x + \alpha_k\right)/Ai'\left(\alpha_k\right)$ forms an orthonormal basis on $x \in [0, \infty[$ and eq. (2.29) can be expanded into this basis [74]. With initial condition $P(\xi, 0) \propto \delta(\xi)$ we obtain

$$P(\xi, \tau) \propto \sum_{k=0}^{\infty} \exp\left[-\alpha_k(\gamma)\tau + \xi\gamma\right] \frac{Ai\left(\xi + \gamma^2 - \alpha_k\right)}{Ai'\left(\gamma^2 - \alpha_k\right)}. \tag{2.32}$$

From eq. (2.32) and eq. (2.26) follows

$$\partial_t P(0, t) \propto \sum_{k=0}^{\infty} \frac{\alpha_k(\gamma)}{t_0} \exp\left[-\alpha_k(\gamma)\tau\right] \frac{Ai\left(\gamma^2 - \alpha_k\right)}{Ai'\left(\gamma^2 - \alpha_k\right)} \tag{2.33}$$

and finally

$$\begin{aligned}\omega_c &= -\frac{\partial_t P(0,t)}{P(0,t)} \\ &= t_0^{-1}\left\{\sum_{k=0}^{\infty}\exp\left[-\alpha_k(\gamma)\tau\right]\frac{Ai\left(\gamma^2-\alpha_k\right)}{Ai'\left(\gamma^2-\alpha_k\right)}\right\} \\ &\quad\times\left\{\sum_{k=0}^{\infty}\alpha_k(\gamma)\exp\left[-\alpha_k(\gamma)\tau\right]\frac{Ai\left(\gamma^2-\alpha_k\right)}{Ai'\left(\gamma^2-\alpha_k\right)}\right\}^{-1}.\end{aligned} \tag{2.34}$$

As $\exp\left[-\alpha_0(\gamma)\tau\right] < \exp\left[-\alpha_k(\gamma)\tau\right]$, for $k \neq 0$, $\tau > 0$ and a fixed value of γ, each summand in eq. (2.34) with $k \neq 0$ is quickly decreased as τ increases. On long times scales $\tau \gg 1$, that is $t \gg t_0$, the catastrophe rate ω_c approaches

$$\omega_c = \frac{\alpha_0(\gamma)}{t_0}. \tag{2.35}$$

Since MTs exhibit stable growth on long time scales, up to several minutes [15], and $t_0 = [0.5d\,(v_+ + v_h)]^{-1/3} \approx (10-30)\,\mathrm{s}$ (Table A.1), we typically have $\tau = t/t_0 \gg 1$ and the catastrophe rate $\omega_c = \omega_c(v_+)$ as a function of γ, and, therefore, as a function of the growth velocity, is given by eq. (2.35). An asymptotic expansion of $\alpha(\gamma)$ in terms of γ^{-1} yields $\alpha_0 = (2\gamma)^{-1} + \mathcal{O}(\gamma^{-3})$ for $\gamma > 1$ and we obtain from eq. (2.35)

$$\omega_c \approx Dr/v \propto v_+^{-2/3}. \tag{2.36}$$

The catastrophe rate decreases as a power law over a wide range of growth velocities.

To calculate the catastrophe rate $\omega_c(v_+)$ as a function of the growth velocity we solved eq. (2.31) numerically and obtained a high order polynomial for $\alpha_0(v_+)$. This polynomial is used in combination with eq. (2.35) to compute $\omega_c(v_+)$. In Fig. 2.5 the catastrophe rate is depicted as a function of v_+. It is clearly visible that $\omega_c(v_+)$ increases as the growth velocity v_+ decreases.

The velocity-dependence of the catastrophe rate $\omega_c(v_+)$ as calculated from eq. (2.35) gives rise to a force-dependence $\omega_c(\eta) = \omega_c[v_+(\eta)]$. We assume that this is the only effect of force on the catastrophe rate [75]. As a result, the catastrophe rate increases exponentially, when $v_+(\eta)$ is decreased by applying a force $\eta = F/F_0$, but a finite value is maintained at $v_+(\eta) = 0$, which is $\omega_c(v_+ = 0) \approx 2.9\,\mathrm{s}^{-1}$. The catastrophe rate $\omega_c(\eta)$ as a function of the dimensionless load force η is shown in Fig. 2.5.

For qualitative approximations, the force-dependence of the catastrophe rate can be described by an exponential increase above the characteristic force F_0,

$$\omega_c(\eta) \sim \omega_c(\eta{=}0)e^{\eta}. \tag{2.37}$$

Different catastrophe models have been proposed and have been shown to describe exper-

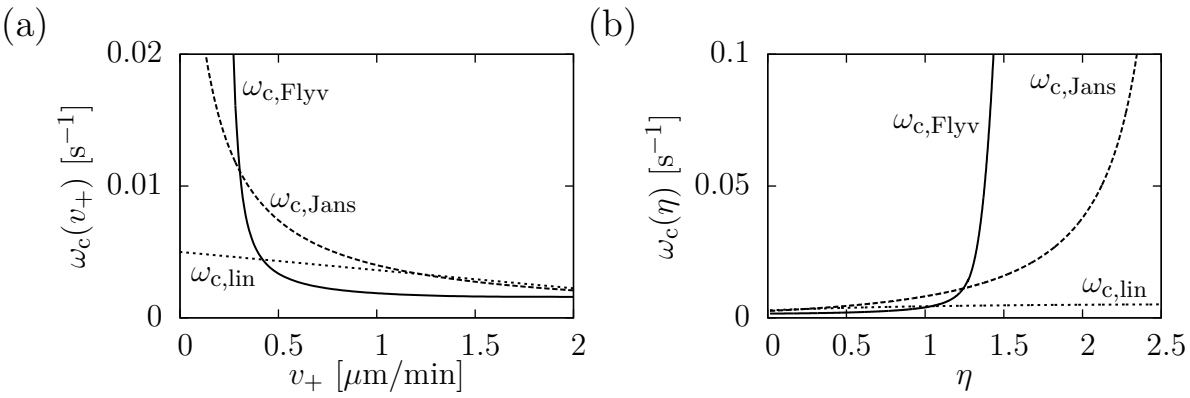

Figure 2.5: (a): The catastrophe rate $\omega_c(v_+)$ as a function of the growth velocity v_+ for the Flyvbjerg model (solid line), the Janson model (dashed line) and the linear catastrophe model (dotted line). (b): The catastrophe rate $\omega_c(\eta)$ as a function of the dimensionless load force $\eta = F/F_0$ with $F_0 \sim 7\,\mathrm{pN}$ and $\omega_{on} = 50\,\mathrm{s}^{-1}$ for the Flyvbjerg model (solid line), the Janson model (dashed line) and the linear catastrophe model (dotted line). In contrast to the linear catastrophe rate both, the Flyvbjerg and the Janson catastrophe rate, increase exponentially for forces larger than the characteristic force F_0.

imentally available data on single-MT catastrophe rates . One alternative phenomenological catastrophe model has been proposed by Janson *et al.* based on experimental data for the inverse catastrophe rate, i.e., the average catastrophe time $\langle \tau_c \rangle = 1/\omega_c$ [75]. The experimental data show that $\langle \tau_c \rangle$ increases linearly with the growth velocity v_+ such that the catastrophe rate, which we will refer as $\omega_{c,Jans}$, is given by

$$\omega_{c,Jans} = \frac{1}{a + b v_+}. \tag{2.38}$$

with $a \simeq 20\,\mathrm{s}$ and $b \simeq 1.4 \times 10^{10}\,\mathrm{s}^2 m^{-1}$ [75].

Also within the catastrophe model by Janson *et al.*, the catastrophe rate $\omega_{c,Jans}$ becomes force dependent via the force-dependence of the growth velocity [see eq. (2.13)], and the resulting catastrophe rate is a nonlinear and increasing function of the dimensionless force η (see Fig. 2.5), which increases exponentially above the characteristic force F_0.

Both the Flyvbjerg and Janson catastrophe models describe available experimental data on *single* MTs, as has been shown in Refs. [18, 68] and [75], respectively.

In both models the catastrophe rate ω_c decreases as a power law over a wide range of growth velocities,

$$\omega_c \propto v_+^{-2/3} \quad \text{(Flyvbjerg)} \quad \text{and} \quad \omega_{c,Jans} \propto v_+^{-1} \quad \text{(Janson)}. \tag{2.39}$$

Because of $v_+ \sim d\omega_{on} e^{-F/F_0}$ for large velocities, ω_c increases exponentially with force F above the characteristic force F_0 in both catastrophe models. This can also be seen in the comparison in Fig. 2.5.

It is possible to consider other types of catastrophe models where the catastrophe rate $\omega_c = \omega_c(v_+)$ is a decreasing function of the growth velocity but does *not* increase exponentially with force F above the characteristic force F_0. One particularly simple example is a catastrophe rate which decreases *linearly* with velocity,

$$\omega_{c,lin}(v_+) = \widetilde{a} - \widetilde{b}v_+. \tag{2.40}$$

The coefficients $\widetilde{a}$ and $\widetilde{b}$ are determined from experimental data [75], under condition $\widetilde{a} > \widetilde{b}v_+$ to ensure $\omega_{c,lin}(v_+) > 0\ \forall v_+$. Janson *et al.* obtained $\omega_{c,min}(v_+) \simeq 1,8 \times 10^{-3}\ s^{-1}$ for $v_+ \simeq 3,8 \times 10^{-8}$ m/s and $\omega_{c,max}(v_+) \simeq 0.05\ s^{-1}$ for $v_+ \simeq 0$ m/s, which are the minor and major catastrophe rates measured. A linear fit with eq. (2.40) results in $\widetilde{a} = 0.05$ s and $\widetilde{b} = 1 \times 10^6\ m^{-1}$. This choice of $\widetilde{a}$ and $\widetilde{b}$, however, leads to $\lambda < 0$ and to bounded MT growth, for all parameter values given in Table A.1. We, therefore, set $\omega_{c,max} = 0.1 \times \omega_{c,max}$ and obtain $\widetilde{a} = 0.005$ s and $\widetilde{b} = 8 \times 10^4\ m^{-1}$ from the linear fit. The linear catastrophe rate $\omega_{c,lin}$ is shown in Fig. 2.5(a) as a function of the growth velocity v_+ and in Fig. 2.5(b) as a function of the dimensionless load force η. In contrast to the catastrophe rates by Flyvbjerg *et al.* and Janson *et al.*, the linear catastrophe rate does not increase exponentially with forces larger than the characteristic force F_0.

Chapter 3

Single MT simulations [1]

In this chapter we present the single MT simulation model. The stochastic equations of motion for a single MT and their numerical implementation are described[2]. We specify simulation parameters, parameter ranges and define ensemble- and time-averages of observables.

3.1 Single microtubule simulation model

In the simulations we solve the stochastic Langevin-like equations of motion for the length $x(t)$ of a single MT using numerical integration with fixed time steps Δt and including stochastic switching between growth and shrinkage. In a growing state $x(t)$ is increased by $v_+\Delta t$, while in a state of shrinkage, it is decreased by $v_-\Delta t$. The equations of motion, at time $t+\Delta t$, are

$$x(t+\Delta t) = x(t) + v_+(x)\Delta t \quad \text{(growing state)} \tag{3.1}$$

$$x(t+\Delta t) = x(t) - v_-\Delta t \quad \text{(shrinking state)} \tag{3.2}$$

At $t=0$ we set $x(0)=0$, that is each MT has zero length, and if $x(t)\leq 0$ the MT undergoes a forced rescue event, corresponding to a reflecting boundary at $x=0$ (see Sec. 2.1) In the growing state, v_+ is calculated from eq. (2.9) for zero force and from eq. (2.11) under force. If the more generalized force-velocity relation by Kolomeisky *et al.* is embedded in the simulation, v_+ is calculated from eq. (2.15). As mentioned in Sec. 2.2, v_- is independent of force and takes the constant value $v_- = 3\times 10^{-7}\,\mathrm{m/s}$ (see Table A.1).
In each time step a uniformly distributed random number $\chi\in[0,1]$ is compared to $\omega_{\mathrm{r,c}}\Delta t$. If $\chi<\omega_{\mathrm{r,c}}\Delta t$ the MT changes its state of growth. We use two nested xor-shift random

[1] Parts of the text have been published in reference [55] and are ©2012 American Physical Society. http://publish.aps.org/copyrightFAQ.html

[2] All numerical implementations are performed in C++

number generators with time-dependent seed, to generate uniformly distributed random numbers [76]. The catastrophe rate ω_c is calculated from eq. (2.35) in the Flyvbjerg model, from eq. (2.38) in the Janson model and from eq. (2.40) in the linear catastrophe model.

To assure $\omega_{r,c}\Delta t \leq 1$, we use a time step $\Delta t = 0.1\,\mathrm{s}$. During the simulations all parameters of growth are fixed, see Table A.2, except for ω_{on}, which is varied in the range $\omega_{on} = (30-100)\,\mathrm{s}^{-1}$, and ω_r, which is varied in a range $\omega_r = (0.03-0.2)\,\mathrm{s}^{-1}$, see Table A.1.

We simulate an ensemble of $N_{ens} = 1000-10000$ (see Table A.2) independent MTs. Time-dependent ensemble averages $\langle O\rangle(t)$ of an observable $O(t)$ are taken over the stochastic trajectories and are calculated from

$$\langle O\rangle(t) = N_{ens}^{-1} \sum_{j=1}^{N_{ens}} O_j(t). \tag{3.3}$$

In addition we perform time averages via

$$\overline{\langle O\rangle} = \Delta T^{-1} \sum_{j=1}^{\Delta T} \langle O\rangle(t). \tag{3.4}$$

Here ΔT denotes the measurement time and we typically have $\Delta T = 50000$ time steps.

In order to determine the characteristic observables for the dynamics of single MTs we have to anticipate numerical results from Chap. 4. We present different types of stochastic trajectories and clarify how observables are determined from numerical data. All shown results are discussed in detail in the following Chapter.

3.1.1 Confinement by rigid walls

For a fixed combination of ω_{on} and ω_r we run N_{ens} independent simulations. In the steady state, determined by visual inspection of sample trajectories, the average length is calculated via eq. (3.4). In addition, we count each MT in the growing state and with $x(t) = L$, and obtain the number of MTs in the growing state and stuck to the boundary wall.

3.1.2 Constant force

For a constant force we determine the critical force F_c, which provides the transition between unbounded and bounded growth, from the condition of a vanishing average velocity $\langle V(F_c)\rangle \approx 0$. For a fixed combination of ω_{on} and ω_r, we run N_{ens} independent simulations. In the simulations we start with a small force F, trace the ensemble-averaged length $\langle x\rangle(t)$ as a function of time (see Fig. 3.1) and perform a linear fit with

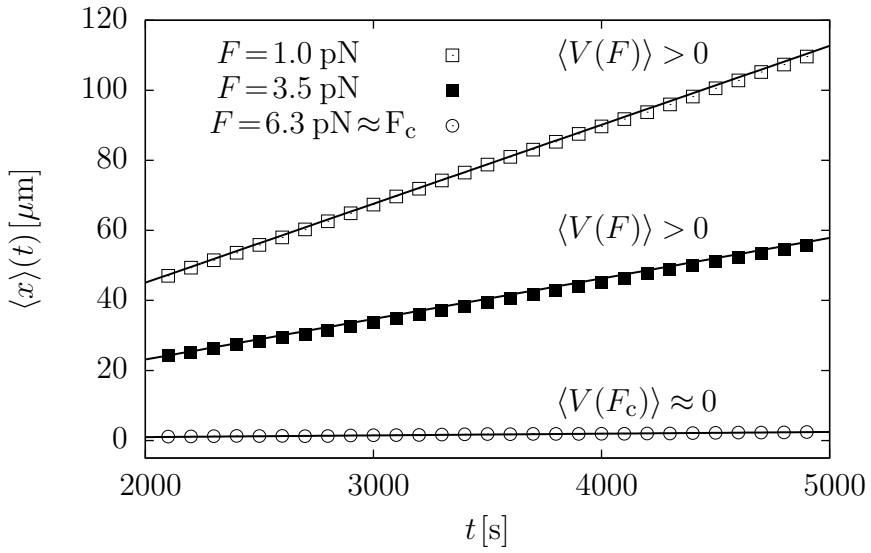

Figure 3.1: Sample trajectories for growth against a constant force F. We set $\omega_{\mathrm{on}} = 70\,\mathrm{s}^{-1}$ and $x_0 = 1\,\mu$m. Symbols represent the ensemble-averaged length $\langle x\rangle(t)$ as a function of time for $F = 1$ pN(□), 3.5 pN(■), and 6.3 pN(⊙). Solid lines are linear fits of eq. (3.5) to the data points.

$$\langle x\rangle(t) = x_0 + \langle V(F)\rangle t. \tag{3.5}$$

Here x_0 denotes the length of the ensemble at $t = 0$ and $\langle V(F)\rangle$ the ensemble-averaged velocity. We set $x_0 = 1\,\mu$m. This choice is arbitrary and does not influence the fit procedure. It turns out, that the choice of $x_0 = 1\,\mu$m reduces the impact of the reflecting boundary at $x = 0$ for forces close to the critical force F_{c}. The simulation time is significantly reduced. In independent simulation runs, we successively increase the constant force F, obtain the average velocity $\langle V(F)\rangle$ from the linear fit and determine the the critical force F_{c} from the condition $\langle V(F_{\mathrm{c}})\rangle \approx 0$ (see Fig. 3.1), for a given combination of ω_{on} and ω_{r}.

3.1.3 Elastic force

3.1.3.1 Vanishing rescue rate

For vanishing rescue rate $\omega_{\mathrm{r}} = 0$ we set $x_0 = 0$. Figure 3.2(a) shows the stochastic time evolution of a single MT. The MT polymerizes against the elastic obstacle until the maximal polymerization force F_{max} is reached. At the maximal polymerization force F_{max} a catastrophe occurs and the dynamics stops, due to missing rescue events. In the simulations, a catastrophe is initiated if the probability $\omega_{\mathrm{c}}(F)\Delta t$ to switch into a state of shrinkage, exceeds the uniformly distributed random number χ (see Sec. 3.1). The maximal polymerization force F_{max} is therefore determined from the condition $\chi < \omega_{\mathrm{c}}(F_{\mathrm{max}})\Delta t$. F_{max} is a stochastic quantity, so we run N_{ens} independent simulations ,

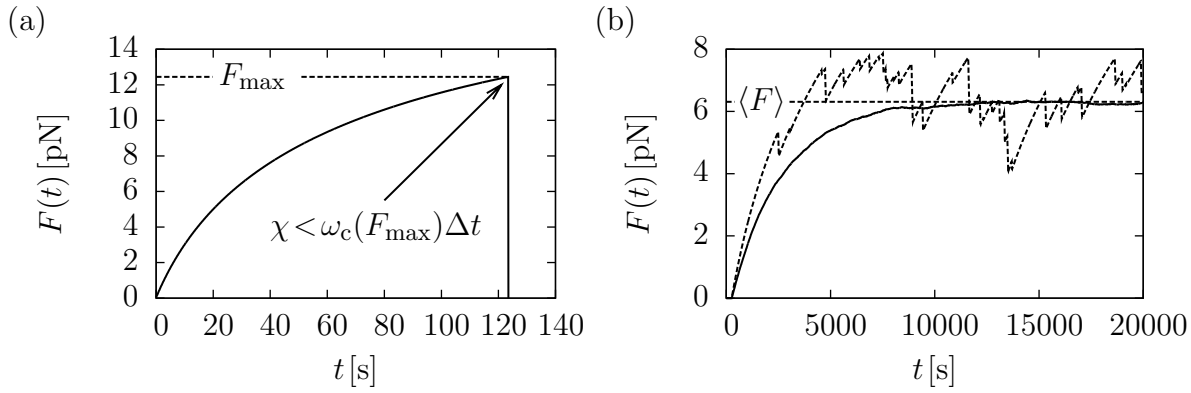

Figure 3.2: Single MT sample trajectories. (a): Vanishing rescue rate $\omega_r = 0$. Polymerization force $F(t)$ as a function of time t. We set $x_0 = 0$, $\omega_{on} = 70\,s^{-1}$ and $k = 10^{-5}$ N/m. The vertical, dashed line marks the maximal polymerization F_{max}. The stochastic quantity F_{max} is determined from the condition $\chi < \omega_c(F_{max})\Delta t$. (b): Non-zero rescue rate $\omega_r = 0.05\,s^{-1}$. Polymerization force $F(t)$ as a function of time t. We set $x_0 = 10\,\mu$m, $\omega_{on} = 70\,s^{-1}$ and $k = 10^{-7}$ N/m. The dashed line represents a single stochastic trajectory and the solid line is the time-dependent ensemble average, obtained via eq. (3.3). The average steady-state force $\langle F \rangle$ ($t \approx 15000$ s) is calculated from eq. (3.4) and marked by a vertical dashed line.

perform an ensemble average via eq. (3.3) and obtain the ensemble averaged maximal polymerization force $\langle F_{max} \rangle$.

3.1.3.2 Non-zero rescue rate

For a non-vanishing rescue rate $\omega_r > 0$ we set $x_0 = 10^{-5}$ m. Figure 3.2(b) shows the stochastic time evolution of a single MT growing against the elastic obstacle. In addition the time-dependent ensemble averaged polymerization force $\langle F(t) \rangle$ is depicted. The time-dependent ensemble average is performed over N_{ens} independent simulations via eq. (3.3). In the steady state, determined by visual inspection of sample trajectories, $\langle F(t) \rangle$ is time averaged over ΔT time steps via eq. (3.4). We obtain the average steady state force $\langle F \rangle$.

Chapter 4

Single microtubule dynamics under force and confinement [1]

In this chapter we present the results for single MT dynamics in three different confinement scenarios, which mimic cellular environments.

Section 4.1 deals with a single MT confined in a box with rigid walls. We introduce a model for wall-induced catastrophes and calculate the OPDF as a function of the growth parameters and the confinement size.

In Sec. 4.2 the MT growth under constant force. We find, as in the absence of force, a regime of bounded and a regime of unbounded growth. Both regimes are characterized by the force-dependent characteristic length parameter $\lambda(f)$ and the critical force f_c, which provides the transition between the two regimes, is determined.

In Sec. 4.3 we investigate MT growth against an elastic obstacle. We start with vanishing rescue rate ω_r, which corresponds to typical experimental conditions, and estimate the average maximal polymerization force by a dynamical mean field theory. Afterwards we focus on the case of a non-vanishing rescue rate. An analytical expression for the OPDF in the steady state is presented and discussed. We calculate the average polymerization force in the steady state as a function of the growth parameters and discuss the influence of the obstacle stiffness on length distributions and polymerization forces. In addition we present a dynamical mean field theory, compare mean field results to full stochastic calculations and discuss the validity of the mean field approximation. Within the mean field theory we derive a time evolution of the time-dependent average polymerization force. Analogue to dilution experiments, we investigate the dynamics of the MT after a sudden change in the GTP-tubulin concentration. Finally we show that our results are robust with respect to changes in the force-velocity relation and in the catastrophe model. Here we restrict our discussion to mean field results.

[1] Parts of the text have been published in reference [55] and are ©2012 American Physical Society. http://publish.aps.org/copyrightFAQ.html

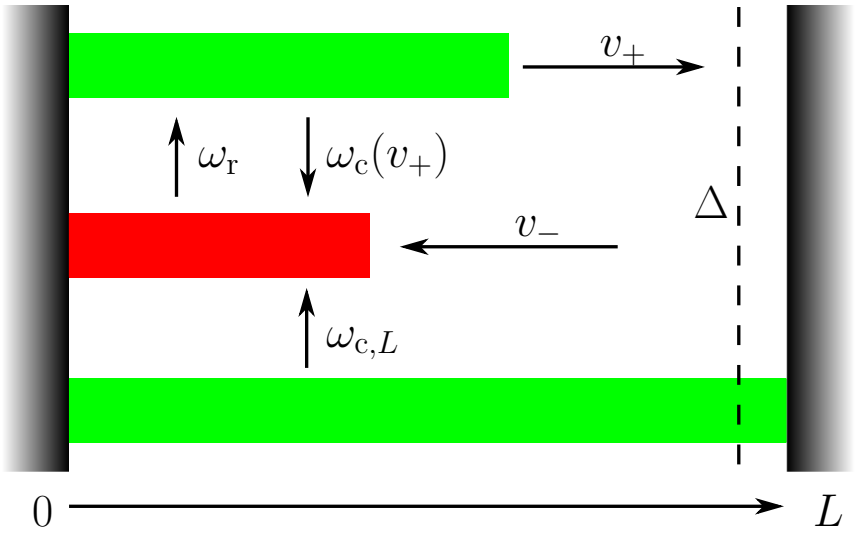

Figure 4.1: Schematic representation of the confinement and possible MT configurations. From top to bottom: A MT growing with v_+; MT shrinks with v_-. MT in a state of growth and stuck to the boundary wall with $v_+ = 0$ and $\omega_{c,L}$ the dashed line marks the interval Δ, in which the flow of probability from the boundary back into the confinement can be measured. .

4.1 Single microtubule dynamics under confinement by rigid walls

A single MT is confined to a one-dimensional box of fixed length L with rigid boundary walls at $x = 0$ and $x = L$ as shown schematically in Fig. 4.1 [77, 78]. There is no force acting on the MT but within the box catastrophes are induced upon hitting the rigid walls. We propose the following mechanism for these wall-induced catastrophes: When the MT hits the boundary at $x = L$, its growth velocity v_+ has to reduce to zero, which leads to an increase of the catastrophe rate to $\omega_{c,L} \equiv \omega_c(v_+ = 0)$. Since $\omega_{c,L}$ is finite, wall-induced catastrophes are not instantaneous but the MT sticks for an average time $1/\omega_{c,L}$ to the boundary before the catastrophe, which is in contrast to previous studies [79]. Throughout this section we use the catastrophe model by Flyvbjerg *et al.* For the average time spent at the boundary before a catastrophe, we find $\omega_{c,L}^{-1} \approx 0.29\,\mathrm{s}$. The catastrophe rate at the wall, $\omega_{c,L}$, is much higher than the bulk catastrophe rate $\omega_c(v_+)$. For $\omega_{on} = 50\,\mathrm{s}^{-1}$ we find $\omega_{c,L}/\omega_c \simeq 2300$.

To include the mechanism of wall-induced catastrophes into the description by master equations, we introduce the probabilities Q_+ and Q_- of finding the MT stuck to the boundary in a growing state and in a shrinking state, respectively. The stochastic time evolution of $Q_+(t)$ and $Q_-(t)$ is given by:

$$\partial_t Q_+(t) = -\omega_{c,L} Q_+(t) + \omega_r Q_-(t) + v_+ p_+(L) \tag{4.1}$$

$$\partial_t Q_-(t) = +\omega_{c,L} Q_+(t) - \omega_r Q_-(t) - \frac{v_-}{\Delta} Q_-(t). \tag{4.2}$$

The quantity $v_+p_+(L)$ is the flow of probability from the interior of the confining box onto its boundary and is given by the solution of eq. (2.1) and (2.2) for $x = L$, while $(v_-/\Delta)Q_-$ is the probability current from the boundary back into the interior, where Δ denotes a small interval in which the flow v_-Q_- can be measured. This implies that there is a boundary condition $v_-p_-(L,t) = (v_-/\Delta)Q_-$ for the backward current density at $x = L$, in addition to the reflecting boundary condition [eq. (2.3)] at $x = 0$. An identical model for wall-induced catastrophes has recently been introduced in Ref. [58].

In the steady state and in the limit $\Delta \approx 0$ we find

$$Q_+ \approx \frac{v_+}{\omega_{c,L}} p_+(L) \tag{4.3}$$

$$Q_- \approx 0, \tag{4.4}$$

and $v_-p_-(L,t) = (v_-/\Delta)Q_- = v_+p_+(L)$. Equation (4.3) shows that there is a non-zero probability Q_+ of finding a MT in a state of growth and stuck to the boundary, which is given by the flow of probability from the interior of the confining box onto its boundary divided by the average time being stuck to the boundary. In contrast, eq. (4.4) states that there is no MT in a shrinking state and stuck to the wall. This is intuitively clear since a MT undergoing a catastrophe begins to shrink instantaneously. In the steady state, we solve eqs. (2.1), (2.2) and (4.3) simultaneously with the additional normalization $\int_0^L [p_+(x) + p_-(x)]\,dx + Q_+ = 1$. We find $v_+p_+(x) = v_-p_-(x)$ and

$$P(x) = Ne^{x/\lambda}\left(1 + \frac{v_+}{v_-}\right) \tag{4.5}$$

$$Q_+ = N\frac{v_+}{\omega_{c,L}} e^{L/\lambda} \tag{4.6}$$

with λ from eq. (2.4) and a normalization

$$N^{-1} = \lambda\left(1 + \frac{v_+}{v_-}\right)\left(e^{L/\lambda} - 1\right) + \frac{v_+}{\omega_{c,L}} e^{L/\lambda}. \tag{4.7}$$

Equation (4.5) shows that we find an exponential OPDF $P(x)$ in confinement with the same characteristic length $|\lambda|$. If the growth is unbounded in the absence of confinement, which corresponds to $\lambda^{-1} > 0$, the OPDF is exponentially increasing; if the growth is bounded in the absence of confinement, which corresponds to $\lambda^{-1} < 0$, the OPDF remains exponentially decreasing in confinement. The same result has been obtained in Ref. [79] within a discrete growth model. In independent *in vivo* experiments, both exponentially increasing [80] and exponentially decreasing OPDFs [56] have been found.

In the following we focus on the case $\lambda^{-1} > 0$ of exponentially increasing OPDFs. In the

steady state, the average length of a MT within the confining box is given by

$$\begin{aligned}\langle x\rangle &= \int_0^L xP(x)dx + Q_+L \\ &= N\left\{\left(1+\frac{v_+}{v_-}\right)\lambda^2\left[1+e^{L/\lambda}\left(\frac{L}{\lambda}-1\right)\right]+L\frac{v_+}{\omega_{c,L}}e^{L/\lambda}\right\}. \end{aligned} \tag{4.8}$$

In the limit of instantaneous wall-induced catastrophes, $Q_+ \approx 0$, we obtain

$$\frac{\langle x\rangle}{L} \approx \frac{1}{1-e^{-L/\lambda}} - \frac{\lambda}{L}, \tag{4.9}$$

i.e., the average MT length $\langle x\rangle/L$ depends on the two control parameters ω_r and ω_{on} only via the ratio L/λ. This scaling property is lost if wall-induced catastrophes are not instantaneous because eq. (4.8) then exhibits additional v_+- and thus ω_{on}-dependencies. Within our model the increased catastrophe rate at the boundary gives rise to an increased overall average catastrophe rate

$$\omega_{c,\text{eff}} = \omega_c(v_+) + Q_+[\omega_{c,L} - \omega_c(v_+)], \tag{4.10}$$

for which we find $\omega_{c,\text{eff}} \simeq 0.03\,\text{s}^{-1}$ for $L = 1\,\mu$m and $\omega_{c,\text{eff}} \simeq 0.006\,\text{s}^{-1}$ for $L = 10\,\mu$m as compared to $\omega_c \simeq 0.0015\,\text{s}^{-1}$ for these conditions.

We set the length of the confining box to $L = 1\,\mu$m and $L = 10\,\mu$m, which are typical length scales in experiments [17, 81] and cellular environments [34], and we calculate $\langle x\rangle$ and Q_+ as functions of ω_{on} and ω_r. The parameter regimes displayed in Figs. 4.2 and 4.3 correspond to regimes $L/\lambda \gg 1$ for $L = 10\,\mu$m and $L/\lambda \ll 1$ for $L = 1\,\mu$m. Results obtained from stochastic simulations agree with analytical findings (Figs. 4.2 and 4.3). It is clearly visible that the size L of the confinement has a significant influence on $\langle x\rangle$, mainly via the ratio L/λ.

The probability Q_+ to find the MT at the wall increases with increasing rates in the range of $Q_+ \approx 0, ..., 0.03$ and exhibits only a weak dependency on L, see Figs. 4.3. Even for maximum rates, the probability of finding a MT in a growing state and stuck to the wall is limited to several percent, due to the large catastrophe rate $\omega_{c,L}$ at $x = L$. Therefore, in most cases wall-induced catastrophes can be viewed as instantaneous, and the approximation (4.9) works well. For increasing on-rate ω_{on} or rescue rate ω_r, the ratio L/λ approaches $L/\lambda \approx L\omega_r/v_-$ from below. According to the approximation (4.9), the mean length $\langle x\rangle$ then increases and approaches $\langle x\rangle/L \approx 1/(1-e^{-L\omega_r/v_-}) - v_-/L\omega_r$ from below. For $L = 10\,\mu$m, we have $L/\lambda \gg 1$ and the length distribution is exponential, $P(x) \sim e^{x/\lambda}$. The ratio $\langle x\rangle/L$ saturates at a high value $\langle x\rangle/L \approx 0.7, ..., 0.9$ [Figs. 4.2 (a),(c)]. For $L/\lambda \gg 1$ the MT length distribution becomes very narrow around the maximal length L. In contrast, for $L = 1\,\mu$m, we have $L/\lambda \ll 1$, and L is too small to establish the characteristic exponential decay of the length distribution. The length distribution $P(x)$

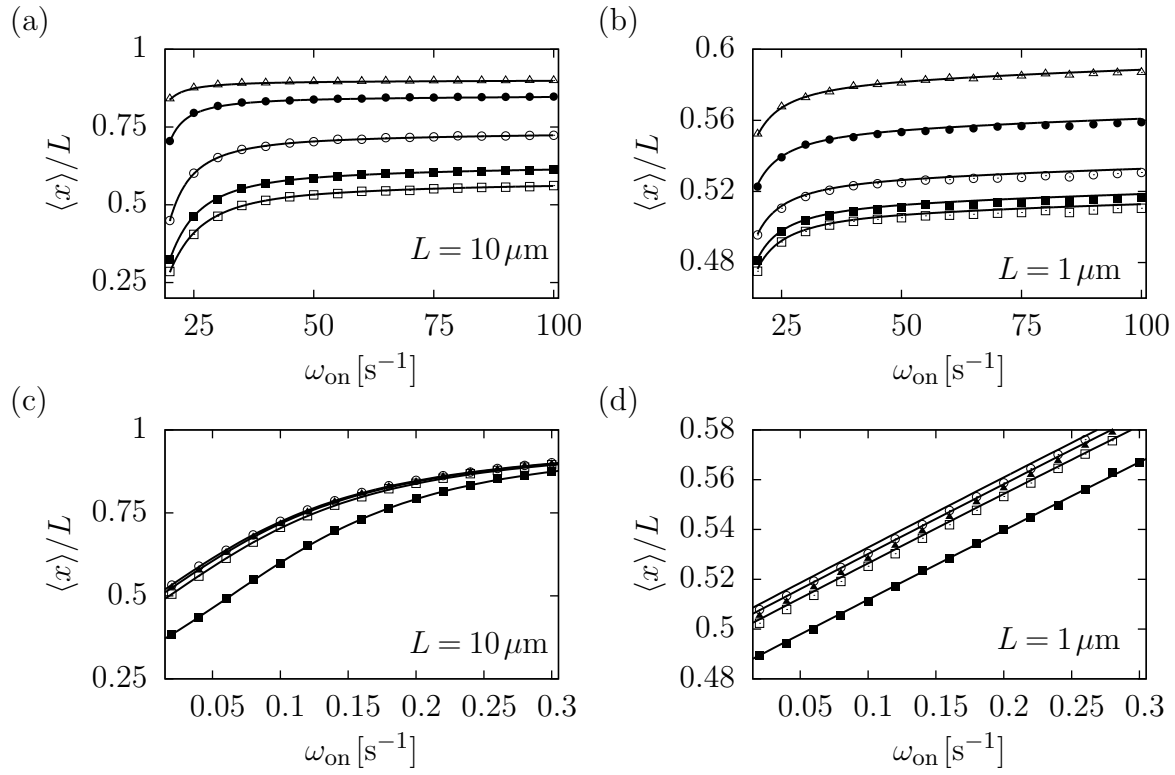

Figure 4.2: The average length $\langle x\rangle/L$ as a function of ω_{on} and ω_{r} for confinement by fixed rigid walls. Data points are results from stochastic simulations, lines are analytical results (eq. 4.8). Top row: The average length $\langle x\rangle/L$ as a function of ω_{on} for different values of $\omega_{\mathrm{r}} = 0.03\,\mathrm{s}^{-1}(\boxdot), 0.05\,\mathrm{s}^{-1}(\blacksquare), 0.1\,\mathrm{s}^{-1}(\odot), 0.2\,\mathrm{s}^{-1}(\bullet)$ and $0.3\,\mathrm{s}^{-1}(\triangle)$. (a) $L = 10\,\mu\mathrm{m}$. (b) $L = 1\,\mu\mathrm{m}$. Lower row: The average length $\langle x\rangle/L$ as a function of ω_{r} for different values of $\omega_{\mathrm{on}} = 25\,\mathrm{s}^{-1}(\blacksquare), 50\,\mathrm{s}^{-1}(\boxdot), 75\,\mathrm{s}^{-1}(\blacktriangle), 100\,\mathrm{s}^{-1}(\boxdot)$. (c) $L = 10\,\mu\mathrm{m}$. (d) $L = 1\,\mu\mathrm{m}$.

is almost uniform, and the ratio $\langle x\rangle/L \approx 0.5, ..., 0.6$ deviates only slightly from the result $\langle x\rangle/L = 1/2$, characteristic for a broad uniform distribution [Figs. 4.2(b),(d)].

4.2 Single microtubule dynamics under a constant force

In the second scenario a constant force η is applied to the MT and the right boundary is removed, so that the MT is allowed to grow on $x \in [0, \infty[$. According to eq. (2.13) the growth velocity under force is smaller, but it remains constant for fixed η. With eq. (2.35) this results in a higher, but also constant, catastrophe rate $\omega_{\mathrm{c}}[v_+(\eta)] > \omega_{\mathrm{c}}[v_+(0)]$. Since v_- and ω_{r} are independent of force, the stochastic dynamics of the MT is described by eqs. (2.1) and (2.2) with the same solutions $P(x,t)$ as in the absence of force, but with a decreased velocity of growth $v_+(\eta)$ and an increased catastrophe rate $\omega_{\mathrm{c}}(\eta)$ [56, 57]. Throughout this section we use the catastrophe model by Flyvbjerg *et al.* In particular, we still find two regimes, a regime of bounded growth and a regime of unbounded growth.

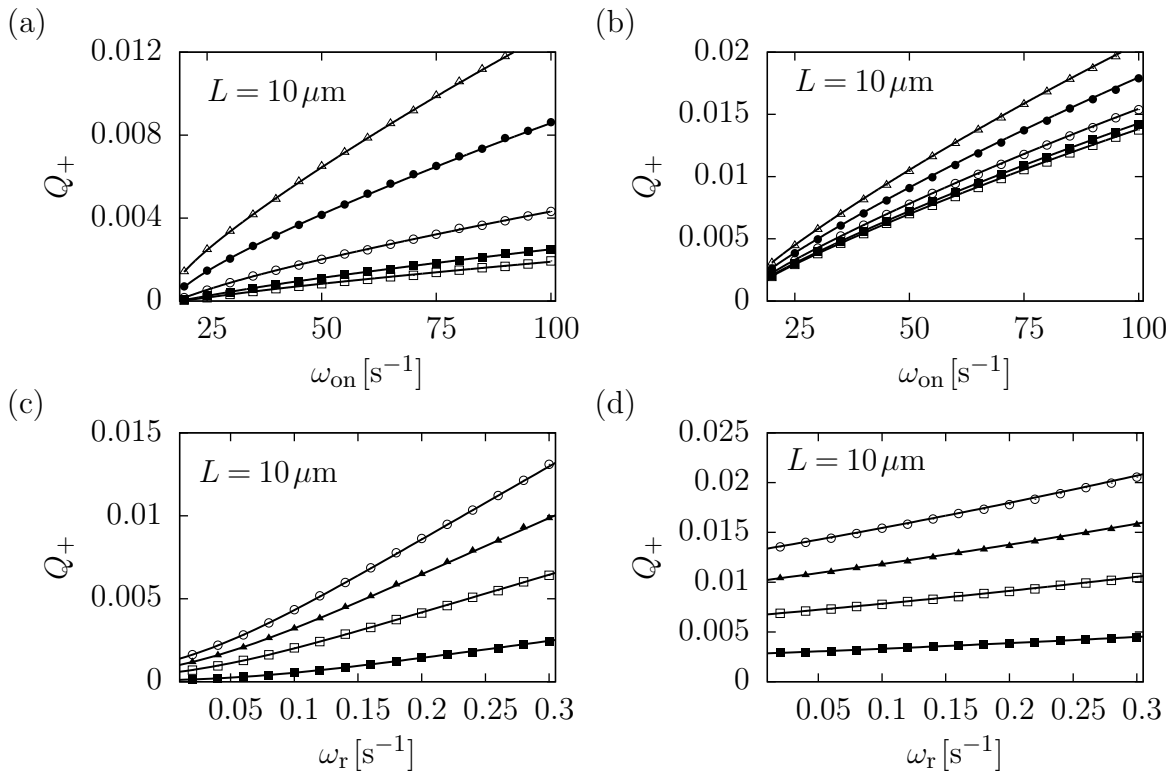

Figure 4.3: The probability Q_+ to find the MT at the wall as a function of $\omega_{\rm on}$ and $\omega_{\rm r}$ for confinement by fixed rigid walls. Data points are results from stochastic simulations, lines are analytical results (eq. 4.3). Top row: Q_+ as a function of $\omega_{\rm on}$ for different values of $\omega_{\rm r} = 0.03\,{\rm s}^{-1}(\boxdot), 0.05\,{\rm s}^{-1}(\blacksquare), 0.1\,{\rm s}^{-1}(\odot), 0.2\,{\rm s}^{-1}(\bullet)$ and $0.3\,{\rm s}^{-1}(\triangle)$. (a) $L = 10\,\mu$m. (b) $L = 1\,\mu$m. Lower row: Q_+ as a function of $\omega_{\rm r}$ for different values of $\omega_{\rm on} = 25\,{\rm s}^{-1}(\blacksquare), 50\,{\rm s}^{-1}(\boxdot), 75\,{\rm s}^{-1}(\blacktriangle), 100\,{\rm s}^{-1}(\boxdot)$. (c) $L = 10\,\mu$m. (d) $L = 1\,\mu$m.

In the regime of bounded growth $P(x,t)$ is again exponentially decreasing, and the force-dependent average length is $\langle x(\eta)\rangle = |\lambda(\eta)|$ with the corresponding force-dependent length parameter

$$\lambda(\eta) \equiv \frac{v_+(\eta)v_-}{v_+(\eta)\omega_\mathrm{r} - v_-\omega_\mathrm{c}(\eta)} \tag{4.11}$$

as compared to eq. (2.4) in the absence of force. In the regime of unbounded growth $\langle x(\eta)\rangle$ increases linearly in time with the force-dependent mean velocity $J(\eta) = [v_+(\eta)\omega_\mathrm{r} - v_-\omega_\mathrm{c}(\eta)]/[\omega_\mathrm{r} + \omega_\mathrm{c}(\eta)]$, cf. eq. (2.7). The MT length distribution $P(x,t)$ assumes again a Gaussian form [eq. (2.6)] where also the diffusion constant $D_J(\eta)$ follows the same eq. (2.8) with force-dependent growth velocity $v_+(\eta)$ and catastrophe rate $\omega_\mathrm{c}(\eta)$.

In the presence of a constant force η, the transition between bounded and unbounded growth is governed by the force-dependent length parameter $\lambda(\eta)$. The regimes of bounded and unbounded growth are now separated by the condition $\lambda^{-1}(\eta) = 0$, which is shifted compared to the case $\eta = 0$, see Fig. 4.5. The inverse length parameter $\lambda^{-1}(\eta)$ is a monotonously decreasing function of force η and changes sign from positive to negative values for increasing force η. Therefore $\lambda^{-1}(\eta_\mathrm{c}) = 0$ or

$$v_+(\eta_\mathrm{c})\omega_\mathrm{r} = v_-\omega_\mathrm{c}(\eta_\mathrm{c}), \tag{4.12}$$

defines a critical force for the transition from unbounded to bounded growth. A single MT exhibiting unbounded growth ($\lambda^{-1}(0) > 0$) in the absence of force undergoes a transition to bounded growth with $\lambda^{-1}(\eta) < 0$ by applying a supercritical force $\eta > \eta_\mathrm{c}$. On the other hand, starting with a combination of on-rate ω_on and rescue rate ω_r and a force η, which results in bounded growth with $\lambda^{-1}(\eta) < 0$, the MT can still enter the regime of unbounded growth by increasing ω_on or ω_r so that the force η becomes subcritical, $\eta < \eta_\mathrm{c}$ or $\lambda^{-1}(\eta) > 0$.

Rewriting condition (4.12) as $v_+(\eta_\mathrm{c}) = v_-\omega_\mathrm{c}(\eta_\mathrm{c})/\omega_\mathrm{r} > 0$ and using that $v_+(\eta)$ decreases with η, it follows that the critical force is always smaller than the stall force, $\eta_\mathrm{c} < \eta_\mathrm{stall}$, which satisfies $v_+(\eta_\mathrm{stall}) = 0$, and it approaches the stall force only for vanishing catastrophe rate. Qualitatively, we can obtain an explicit result for the critical force η_c by using the approximations of an exponentially decreasing growth velocity, $v_+(\eta) \approx v_+(0)e^{-\eta}$, which is valid for $\omega_\mathrm{on} \gg \omega_\mathrm{off}$ [see eq. (2.13)], and an exponentially increasing catastrophe rate above the characteristic force F_0, eq. (2.37), in the condition (4.12) for the critical force. This leads to

$$\eta_\mathrm{c} \sim \frac{1}{2}\ln\left(\frac{v_+(0)\omega_\mathrm{r}}{v_-\omega_\mathrm{c}(0)}\right) \sim \frac{1}{2}\ln\left(\frac{\omega_\mathrm{on} d\omega_\mathrm{r}}{v_-\omega_\mathrm{c}(0)}\right) \tag{4.13}$$

which shows that the critical force grows approximately logarithmically with on-rate ω_on (note that the catastrophe rate in the absence of force decreases with ω_on as $\omega_\mathrm{c}(0) \propto 1/\omega_\mathrm{on}$ [18]) and rescue rate ω_r. A negative η_c for small on-rates and rescue rates signals that the MT is for all forces $\eta > 0$ in the bounded phase. In Fig. 4.4 we show exact results for

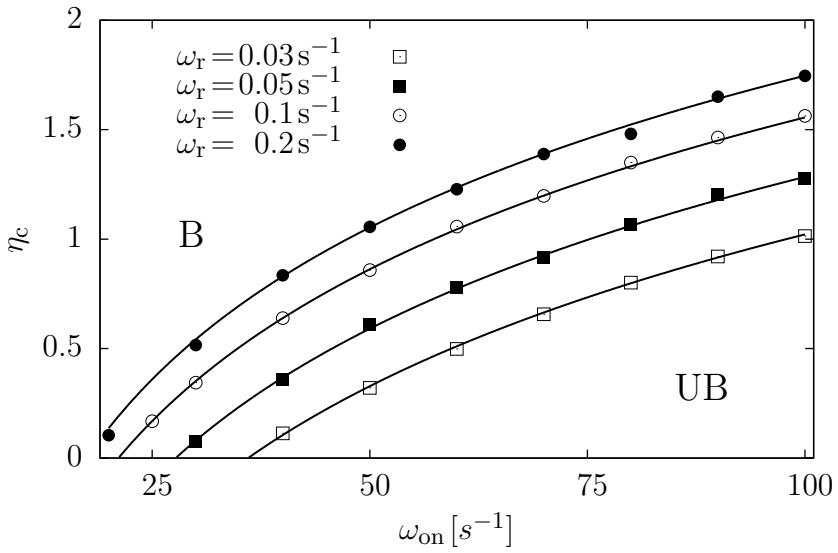

Figure 4.4: Critical force η_c as a function of ω_{on} for $\omega_r = 0.03\,s^{-1}(\boxdot), 0.05\,s^{-1}(\blacksquare), 0.1\,s^{-1}(\odot), 0.2\,s^{-1}(\bullet)$. Data points represent results from simulations, lines represent solutions of eq. (4.12) for a fixed combination of ω_{on} and ω_r. B: bounded growth. UB: unbounded growth.

the critical force η_c as a function of the on-rate ω_{on} and for different rescue rates ω_r from solving condition (4.12) numerically and from stochastic simulations. Agreement between both methods is good.

The condition $\lambda^{-1}(\eta) = 0$ specifies the boundary between bounded and unbounded growth at a given force η. In Fig. 4.5, the resulting phase boundary is shown as a function of ω_{on} and ω_r. There is good agreement between numerical solutions of $\lambda^{-1}(\eta) = 0$ and stochastic simulations. With increasing force, the boundary between the two regimes of growth shifts to higher values of ω_{on} and ω_r, and forces up to $F \sim 1.4 \cdot F_0$ can be overcome by a single MT in the parameter regimes of ω_{on} and ω_r considered.

4.3 Single microtubule dynamics under an elastic force

In the third scenario, an elastically coupled barrier is placed in front of the MT as shown in Fig. 4.6, which models the optical traps used in Refs. [17, 53] or the elastic cell cortex *in vivo*. If the barrier is displaced from its equilibrium position x_0 by the growing MT with length $x > x_0$, it causes a force $F(x) = k(x - x_0)$ resisting further growth. For $x < x_0$ there is no force. We use $x_0 = 0\,\mu$m in the case of vanishing rescue rate, $x_0 = 10\,\mu$m in the case of finite rescue rate and a spring constant k in the range $10^{-7}\,$N/m (soft) to $10^{-5}\,$N/m (stiff as in the optical trap experiments in [53]).

An elastic force $F(x) = k(x - x_0)$ represents the simplest and most generic x-dependent

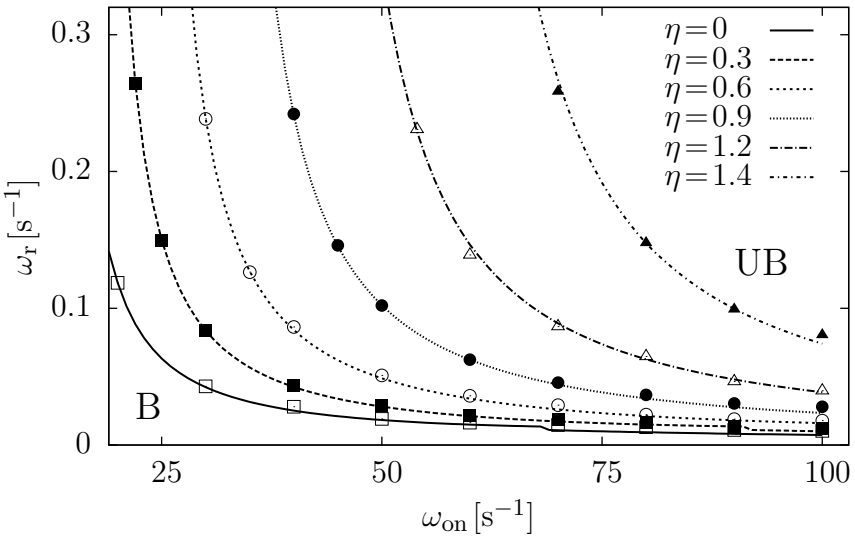

Figure 4.5: Phase boundary between bounded (B) and unbounded growth (UB) as a function of ω_{on} and ω_r for MT growth under constant force. Data points for $\eta = 0(\boxdot), 0.3(\blacksquare), 0.6(\odot), 0.9(\bullet), 1.2(\triangle), 1.4(\blacktriangle)$ represent results from simulations, lines represent solutions of $\lambda^{-1}(\eta) = 0$ [see eq. (4.11)] for a constant force η.

force. Whereas for a confinement of fixed length or a constant force, the MT length x was the only stochastic variable, the force $F(x)$ itself is now coupled to x and becomes stochastic as well. Therefore, not only are the MT length distributions of interest but also the maximal and average polymerization forces which are generated during MT growth.

4.3.1 Vanishing rescue rate

We first discuss growth in the absence of rescue events, $\omega_r = 0$. This situation corresponds to optical trap experiments [17, 53], which are performed on short time scales and no rescue events are observed. In a state of growth the MT grows against the elastic obstacle with velocity $v_+[\eta(x)]$ and $\eta(x)$ increases. For simplicity we suppress the x-dependency in the notation in the following. At a maximal polymerization force η_{max}, the MT undergoes a catastrophe and starts to shrink back to zero and the dynamics stops due to missing rescue events. No steady state is reached. Since switching to the state of shrinkage is a stochastic process, the maximal polymerization force η_{max} is a stochastic quantity which fluctuates around its average value. We calculate the average maximal polymerization force $\langle \eta_{max} \rangle$ within a mean field approach.

Because no steady state is reached in the absence of rescue events, we have to use a dynamical mean field approach, which is based on the fact that the MT growth velocity $dx/dt = v_+(\eta)$ is related to the time evolution of the force by $d\eta/dt = (k/F_0)dx/dt$.

In order to obtain the average maximal polymerization force, we perform an ensemble

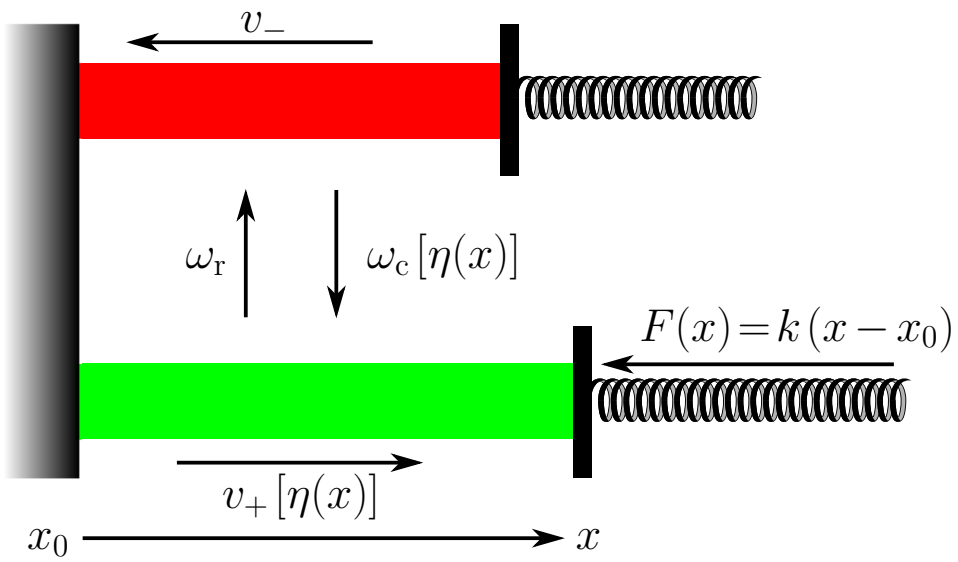

Figure 4.6: Schematic representation of a single MT growing against an elastic obstacle with spring constant k. From top to bottom: MT shrinks (red) with v_-. MT growth (green) under force $F(x) = k(x - x_0)$ with $\eta(x) \equiv F(x)/F_0$, $v_+[\eta(x)]$, and force-dependent catastrophe rate $\omega_c[\eta(x)]$.

average over many realizations of the stochastic growth trajectory and obtain

$$\frac{d}{dt}\langle\eta\rangle = \frac{k}{F_0}\langle v_+(\eta)\rangle. \tag{4.14}$$

Since the probability density function $p(\eta)$, which determines the ensemble average, is not known, we use a mean-field like approximation to perform further calculations. In the following, we assume a strongly localized probability density distribution function, centered at the average polymerization force $\langle\eta\rangle$, and with most of the probability weight localized at or close to the average maximal polymerization force $\langle\eta\rangle$. In addition we neglect all higher correlations. This type of approximation allows us to replace global averages by local averages. To be more precise, we set $\langle v_+(\eta)\rangle \approx v_+(\langle\eta\rangle)$. The average growth velocity under force is replaced by the growth velocity under the average force $\langle\eta\rangle$ and we obtain, in mean field approximation, the following equation of motion for $\langle\eta\rangle$,

$$\frac{d}{dt}\langle\eta\rangle = \frac{k}{F_0}v_+(\langle\eta\rangle) \tag{4.15}$$

With the initial condition $\langle\eta\rangle(0) = 0$ we find a time evolution

$$\langle\eta\rangle(t) = \ln\left[(1 - \omega_{on}/\omega_{off})\, e^{-t/\tau} + \omega_{on}/\omega_{off}\right] \tag{4.16}$$

$$\approx \eta_{stall} + \ln\left[1 - \exp(-t/\tau)\right] \tag{4.17}$$

with a characteristic time scale $\tau = F_0/dk\omega_{off} \approx (10^2 ... 10^4)\,\mathrm{s}$ for $k \approx 10^{-5} ... 10^{-7}\,\mathrm{N/m}$. For

long times $t \gg \tau$, eq. (4.16) approaches the dimensionless stall force $\langle \eta \rangle = \eta_{\text{stall}}$, see eq. (2.14), which is the maximal polymerization force in the absence of catastrophes. The approximation (4.17) holds for $\omega_{\text{on}}/\omega_{\text{off}} \gg 1$.

MT growth is ended, however, by a catastrophe, and the average time spent in the growing state is $t = 1/\omega_{\text{c}}(\langle \eta_{\text{max}} \rangle)$. Together with eq. (4.16), this gives a self-consistent mean field equation for the average maximal polymerization force $\langle \eta_{\text{max}} \rangle$,

$$\langle \eta_{\text{max}} \rangle = \ln \left[(1 - \omega_{\text{on}}/\omega_{\text{off}})\, e^{-1/\omega_{\text{c}}(\langle \eta_{\text{max}} \rangle)\tau} + \omega_{\text{on}}/\omega_{\text{off}} \right]. \tag{4.18}$$

The average maximal polymerization force $\langle \eta_{\text{max}} \rangle$ is always smaller than the stall force η_{stall} as can be seen from eqs. (4.16) and (4.17). Since $\omega_{\text{on}}/\omega_{\text{off}} \gg \omega_{\text{c}}\tau \gg 1$ for realistic forces and parameter values, eq. (4.18) can be approximated by

$$\begin{aligned} \langle \eta_{\text{max}} \rangle &\approx \ln \left(\frac{\omega_{\text{on}}}{\omega_{\text{off}} \tau \omega_{\text{c}}(\langle \eta_{\text{max}} \rangle)} \right) \\ &= \eta_{\text{stall}} - \ln \left[\tau \omega_{\text{c}}(\langle \eta_{\text{max}} \rangle) \right]. \end{aligned} \tag{4.19}$$

For a catastrophe rate increasing exponentially above the characteristic force F_0, eq. (2.37), we find

$$\langle \eta_{\text{max}} \rangle \sim \frac{1}{2} \ln \left(\frac{\omega_{\text{on}} dk}{F_0 \omega_{\text{c}}(0)} \right), \tag{4.20}$$

i.e., the average maximal polymerization force grows logarithmically in ω_{on} (note that the catastrophe rate in the absence of force decreases as $\omega_{\text{c}}(0) \propto 1/\omega_{\text{on}}$ [18]), see Fig. 4.7 for $k = 10^{-5}\,\text{N/m}$. Within a slightly different catastrophe model obtained from experimental data and discussed in section 4.4.1, this logarithmic dependence can be shown exactly.

Fig. 4.7 shows $\langle \eta_{\text{max}} \rangle$ as a function of ω_{on}. Analytical results from eq. (4.18) agree with numerical findings from stochastic simulations. The average maximal polymerization force $\langle \eta_{\text{max}} \rangle$ increases with increasing k, see eq. (4.20), but it remains smaller than the stall force η_{stall}. Stochastic simulations show considerable fluctuations of $\langle \eta_{\text{max}} \rangle$, which are caused by broad and exponentially decaying probability distributions for η_{max} and which we quantify by measuring the standard deviation $\langle \eta_{\text{max}}^2 \rangle - \langle \eta_{\text{max}} \rangle^2$. For increasing k, probability distributions become more narrow and mean field results approach the simulation results for $\langle \eta_{\text{max}} \rangle$.

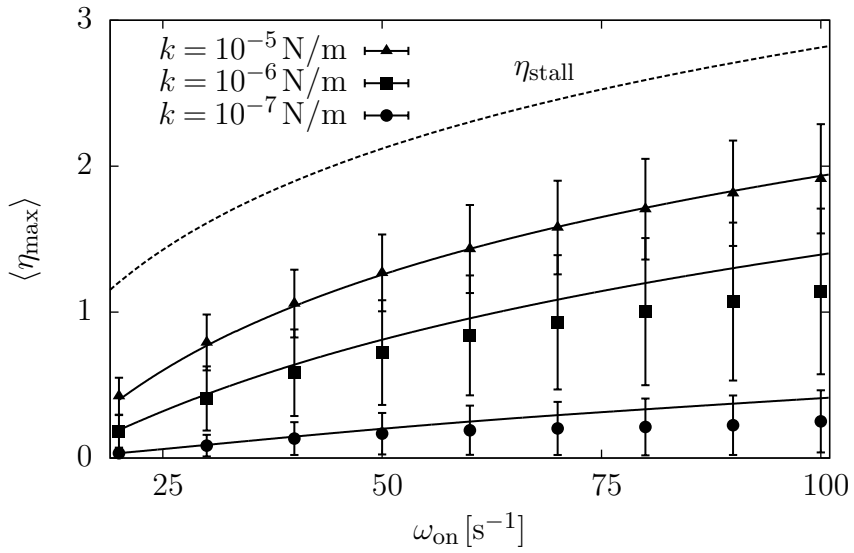

Figure 4.7: Average maximal polymerization force $\langle \eta_{\mathrm{max}} \rangle$ for an elastic obstacle and in the absence of rescues as a function of ω_{on} for different values of $k = 10^{-5}\,\mathrm{N/m}$(▲), $10^{-6}\,\mathrm{N/m}$(■), and $10^{-7}\,\mathrm{N/m}$(●). Data points represent results from simulations, solid lines are solutions of eq. (4.18). Error bars represent the standard deviation of the stochastic quantity $\langle \eta_{\mathrm{max}} \rangle$. Dashed line: dimensionless stall force $\eta_{\mathrm{stall}} = \ln(\omega_{\mathrm{on}}/\omega_{\mathrm{off}})$.

4.3.2 Non-zero rescue rate[2]

4.3.2.1 Stochastic approach

For a non-zero rescue rate ω_{r}, phases of growth, in which $\eta(x)$ increases and which last $1/\omega_{\mathrm{c}}(\eta)$ on average, are ended by catastrophes which are followed by phases of shrinkage. Shrinking phases last $1/\omega_{\mathrm{r}}$ on average, and during shrinkage the elastic obstacle is relaxed and $\eta(x)$ decreases. After rescue, the MT switches back to a state of growth. In contrast to the case without rescue events, the system can attain a steady state. In this steady state, the average length loss during shrinkage, v_-/ω_{r}, equals the average length gain during growth, $v_+(\eta)/\omega_{\mathrm{c}}(\eta)$, and the MT oscillates around a time-averaged stall length $\langle x \rangle$, which is directly related to the time-averaged polymerization force by $\langle \eta \rangle = (k/F_0)(\langle x \rangle - x_0)$. In the following, the steady state dynamics and the average polymerization force are characterized. We start with an analysis of the full master equations focusing on the stationary state followed by a dynamical mean field theory, which can also be applied to dilution experiments.

In the presence of a x-dependent force $\eta(x)$, the master equations for the time evolution

[2]Parts of the results of this section have been achieved in cooperation with Nina Müller during her bachelor thesis [82].

of $p_+(x,t)$ and $p_-(x,t)$ become

$$\partial_t p_+(x,t) = -\omega_c(x)p_+(x,t) + \omega_r p_-(x,t) - \partial_x[v_+(x)p_+(x,t)] \tag{4.21}$$

$$\partial_t p_-(x,t) = \omega_c(x)p_+(x,t) - \omega_r p_-(x,t) + v_-\partial_x p_-(x,t), \tag{4.22}$$

which differ from eqs. (2.1) and (2.2) by the x-dependence of the growth velocity and the catastrophe rate. Both growth velocity $v_+(x) = v_+[\eta(x)]$ and catastrophe rate $\omega_c(x) = \omega_c\{v_+[\eta(x)]\}$ become x-dependent via their force-dependence. Therefore, also the force-dependent length parameter $\lambda(\eta)$ from eq. (4.11) becomes x-dependent via its force-dependence, $\lambda(x) = \lambda[\eta(x)]$. Eqs. (2.1) and (2.2) are supplemented by a reflecting boundary condition $v_+(0)p_+(0,t) = v_-p_-(0,t)$ at $x = 0$, similar to eq. (2.3).

For the steady state, eqs. (4.21) and (4.22) are solved on the half-space $x > 0$ with reflecting boundary conditions at $x = 0$, and we can calculate the overall MT length distribution $P(x) = p_+(x) + p_-(x)$ explicitly,

$$P(x) = N\left(1 + \frac{v_-}{v_+(x)}\right) e^{x_0/\lambda(0)} \exp\left[\int_{x_0}^{x} dx'/\lambda(x')\right] \tag{4.23}$$

with a normalization

$$N^{-1} = \int_0^\infty dx \left(1 + \frac{v_-}{v_+(x)}\right) e^{x_0/\lambda(0)} e^{\int_{x_0}^{x} dx'/\lambda(x')}, \tag{4.24}$$

where $\lambda(x) = \lambda(\eta = 0)$ in the force-free region $x < x_0$ and $\lambda(x) = \lambda[\eta(x)]$ for $x > x_0$ and, likewise, $v_+(x) = v_+(\eta = 0)$ for $x < x_0$ and $v_+(x) = v_+[\eta(x)]$ for $x > x_0$. This implies $e^{x_0/\lambda(0)} e^{\int_{x_0}^{x} dx'/\lambda(x')} = e^{x/\lambda(0)}$ and, thus, a simple exponential dependence of $P(x)$ for $x < x_0$. A similar OPDF has been found for dynamic MTs in the presence of MT end-tracking molecular motors [83].

With increasing length x, also the force $\eta(x)$ increases and, thus, $v_+[\eta(x)]$ decreases and $\omega_c[\eta(x)]$ grows exponentially. If x becomes sufficiently large that the condition $\lambda^{-1}[\eta(x)] < 0$ holds, the distribution $P(x)$ starts to *decrease* exponentially. In this length regime the MT undergoes a catastrophe with high probability. Because the distribution always decreases exponentially for sufficiently large x, a single MT growing against an elastic obstacle is always in the regime of bounded growth regardless of how large the values of ω_{on} and ω_r are chosen. This behavior is a result of the linearly increasing force, which gives rise to arbitrarily large forces for increasing x in contrast to growth under constant or zero force, where a MT can either be in a phase of bounded or unbounded growth as mentioned above.

The behavior is also in contrast to length distributions in confinement between fixed rigid walls, where we found a transition between exponentially decreasing and increasing length distributions: The elastic obstacle typically leads to a non-monotonic length distribution

with a *maximum* in the region $x > x_0$ (as long as the on-rate $\omega_{\rm on}$ and rescue rate $\omega_{\rm r}$ are sufficiently large and the obstacle stiffness k sufficiently small). While rescue events and an exponential decrease in the growth velocity $v_+[\eta(x)]$ cause $P(x)$ to increase exponentially for small MT length, catastrophes are responsible for an exponential decrease for large x. The interplay between rescues and catastrophes gives rise to strongly *localized* probability distributions with a maximum. Figs. 4.8 (a-d) show the steady state distribution $P(x)$ obtained from eq. (4.23) for different values of $\omega_{\rm on}$ and $\omega_{\rm r}$. We chose $k = 10^{-7}\,{\rm N/m}$ and $x_0 = 10\,\mu{\rm m}$. In the steady state, a stable length distribution with a well defined average length $\langle x\rangle = \int_0^\infty P(x)x dx$ is maintained although the MT is still subject to dynamic instability. The length distributions drop to zero for large x, where $\lambda^{-1}(x) \sim -\omega_{\rm c}(x)/v_+(x)$ and $\omega_{\rm c}(x)/v_+(x)$ increases exponentially with increasing force.

The most probable MT length $x_{\rm mp}$ maximizes the stationary length distribution [eq. (4.23)]. Because $v_- \gg v_+(x)$ and using the approximation of an exponentially decreasing growth velocity, $v_+[\eta(x)] \approx v_+(0)e^{-\eta(x)}$, which is valid for $\omega_{\rm on} \gg \omega_{\rm off}$ [see eq. (2.13)], we obtain a condition $\lambda^{-1}(x_{\rm mp}) = -\partial_x \eta(x_{\rm mp}) = -k/F_0$ or

$$v_+(\eta_{\rm mp})\omega_{\rm r} - v_-\omega_{\rm c}(\eta_{\rm mp}) = -(k/F_0)v_-v_+(\eta_{\rm mp}) \tag{4.25}$$

for the corresponding most probable force $\eta_{\rm mp} = (k/F_0)(x_{\rm mp} - x_0)$.

For an exponentially increasing catastrophe rate above the characteristic force F_0, eq. (2.37), we find

$$\eta_{\rm mp} \sim \frac{1}{2}\ln\left[\frac{v_+(0)\omega_{\rm r}}{v_-\omega_{\rm c}(0)}\left(1+\frac{kv_-}{F_0\omega_{\rm r}}\right)\right] \tag{4.26}$$

We can distinguish two limits:
(i) For a *soft* obstacle with $kv_-/F_0\omega_{\rm r} \ll 1$ the most probable force $\eta_{\rm mp}$ is identical to the critical force $\eta_{\rm c}$ for MT dynamics under constant force, see eq. (4.13), because the right hand side in the condition (4.25) for $\eta_{\rm mp}$ can be neglected and we exactly recover condition (4.12) for $\eta_{\rm c}$. The most probable MT length thus "self-organizes" into a "critical" state with $\eta_{\rm mp} \approx \eta_{\rm c}$, and a MT pushing against a soft elastic obstacle generates the same force as if growing against a constant force. This force grows logarithmically in the on-rate $\omega_{\rm on}$ and the rescue rate $\omega_{\rm r}$.
(ii) For a *stiff* obstacle with $kv_-/F_0\omega_{\rm r} \gg 1$, on the other hand, the most probable force is larger than the critical force, $\eta_{\rm mp} \gg \eta_{\rm c}$, and the MT growing against a stiff obstacle generates a *higher* force. This limit can also be realized for vanishing rescue rate $\omega_{\rm r}$, and for $kv_-/F_0\omega_{\rm r} \gg 1$ we indeed recover the maximal pushing force in the absence of rescue events, i.e. $\eta_{\rm mp} \approx \langle\eta_{\rm max}\rangle$ from eq. (4.20) with $v_+(0) \approx \omega_{\rm on}d$. This force grows logarithmically in the on-rate $\omega_{\rm on}$. Furthermore, if $\eta_{\rm mp}$ becomes negative for small on-rates and rescue rates [leading to $\lambda^{-1}(0) < -k/F_0$, see eq. (4.26)] the stationary length distribution has no maximum, see for example Figs. 4.8(a,b) at the lowest on-rates.

With respect to the MT's ability to generate force the two limits can be interpreted also in the following way: F_0 is the characteristic force above which the catastrophe rate increases exponentially. For $kv_-/F_0\omega_r \ll 1$, the average length loss during a period of shrinkage, v_-/ω_r, is much smaller than the length F_0/k, which is the displacement $x - x_0$ of the elastic obstacle under the characteristic force F_0. Therefore, the MT tip always remains in the region $x > x_0$ under the influence of the force for a soft obstacle with $kv_-/F_0\omega_r \ll 1$, whereas, for a stiff obstacle $kv_-/F_0\omega_r \gg 1$, it typically shrinks back into the force-free region $x < x_0$ before the next rescue event . The force generation by the MT can only be enhanced by rescue events if rescue takes place under force in the regime $x > x_0$. Therefore, we find an increased polymerization force $\eta_{mp} \approx \eta_c \gg \langle\eta_{max}\rangle$ as compared to the force $\langle\eta_{max}\rangle$ without rescue events discussed in the previous section only in the limit $kv_-/F_0\omega_r \ll 1$, i.e., for a soft obstacle or sufficiently large rescue rate. In the limit $kv_-/F_0\omega_r \gg 1$ of a stiff obstacle, the MT only generates the same force as in the absence of rescues, $\eta_{mp} \approx \langle\eta_{max}\rangle$.

By comparing the condition (4.12) or $v_+(\eta_c) = v_-\omega_c(\eta_c)/\omega_r$ for the critical force η_c, the condition (4.25) or $v_+(\eta_{mp}) = v_-\omega_c(\eta_{mp})/\omega_r(1 + kv_-/F_0) < v_-\omega_c(\eta_{mp})/\omega_r$ for the most probable force η_{mp}, and the condition $v_+(\eta_{stall}) = 0$ for the stall force, see eq. (2.14), it follows that

$$\eta_c \leq \eta_{mp} \ll \eta_{stall} \tag{4.27}$$

i.e., force generated against an elastic obstacle is between critical and stall force but typically well below the stall force, which is the maximal polymerization force in the absence of catastrophes. Therefore, the stall length $x_{stall} = (F_0/k)\ln(\omega_{on}/\omega_{off}) + x_0$ is always much larger than the most probable MT length x_{mp} at the maximum of the stationary length distribution, see Fig. 4.8(a). This shows that the dynamic instability reduces the typical MT length significantly compared to simple polymerization kinetics.

In order to quantify the width of the stationary distribution $P(x)$ we expand the exponential in eq. (4.23) up to second order about the maximum at x_{mp}. To do so we first expand $\lambda^{-1}(x)$ up to first order:

$$\lambda^{-1}(x) \approx -\frac{k}{F_0}\left[\frac{v_+(x_{mp})\omega_r + v_-\omega_c(x_{mp})}{v_+(x_{mp})v_-}\right](x - x_{mp}) \tag{4.28}$$

where we used $v_+[\eta(x)] \approx v_+(0)e^{-\eta(x)}$, which is valid for $\omega_{on} \gg \omega_{off}$ [see eq. (2.13)], and where we approximated the catastrophe rate by an exponential $\omega_c[\eta(x)] \approx \omega_c(0)e^{\eta(x)}$ according to eq. (2.37) resulting in $\omega_c'[\eta(x)] \approx k\omega_c[\eta(x)]/F_0$. The prime denotes a derivative with respect to the length x. Using the expansion [eq. (4.28)] in eq. (4.23), we obtain an approximately Gaussian length distribution

$$P(x) \approx N\left(1 + \frac{v_-}{v_+(x)}\right)e^{x_0/\lambda(0)}\exp\left[\frac{(x_{mp} - x_0)^2}{2\sigma^2}\right]\exp\left[-\frac{(x - x_{mp})^2}{2\sigma^2}\right] \tag{4.29}$$

with a width

$$\sigma^2 = \frac{F_0}{k}\left[\frac{v_+(x_{\rm mp})v_-}{v_+(x_{\rm mp})\omega_{\rm r} + v_-\omega_{\rm c}(x_{\rm mp})}\right] \approx \left(\frac{F_0}{k}\right)^2\left(1+\frac{2F_0\omega_{\rm r}}{kv_-}\right)^{-1} \tag{4.30}$$

where we used the saddle point condition (4.25) in the last approximation and the exponential approximations $v_+[\eta(x)] \approx v_+(0)e^{-\eta(x)}$ and $\omega_{\rm c}[\eta(x)] \approx \omega_{\rm c}(0)e^{\eta(x)}$. Again we have to distinguish the two limits of soft and stiff obstacles:
(i) For a soft obstacle with $kv_-/F_0\omega_{\rm r} \ll 1$ we find $\sigma^2 \approx F_0 v_-/2k\omega_{\rm r}$. This shows that the width of the length distribution decreases with increasing $\omega_{\rm r}$ but is roughly independent of the on-rate $\omega_{\rm on}$, as can also be seen in the series of numerical results shown in Figs. 4.8. A closer inspection shows that the width of the stationary length distribution $P(x)$ is slightly decreasing with the on-rate $\omega_{\rm on}$.
(ii) For a stiff obstacle with $kv_-/F_0\omega_{\rm r} \gg 1$, on the other hand, we find $\sigma^2 \approx (F_0/k)^2$, which only depends on obstacle stiffness. All in all, σ^2 is monotonously decreasing for increasing stiffness k.

For a soft obstacle $kv_-/F_0\omega_{\rm r} \ll 1$, high rescue rates thus lead to a sharply peaked length distribution $P(x)$ and suppress fluctuations of the MT length around $x = x_{\rm mp}$ and we expect $\langle x\rangle \approx x_{\rm mp}$ to a very good approximation. This property of a sharp maximum in $P(x)$ will make the mean field approximation that is discussed in the next section very accurate.

If the obstacle stiffness k is increased the most probable MT length $x_{\rm mp} = x_0 + \eta_{\rm mp}F_0/k$ approaches x_0, and a considerable probability weight is shifted to MT lengths x below x_0 (see Fig. 4.9). The average length approaches and finally drops below x_0. This signals that the force generated by the MT is no longer sufficient to push the obstacle out of its equilibrium position x_0. The obstacle now serves as a fixed rigid boundary and $P(x)$ approaches the results from eqs. (4.6) and (4.7). The dynamics of a single MT within confinement can therefore be seen as a special case of the dynamics in the presence of an elastic obstacle, i.e., for small $\omega_{\rm on}$ and $\omega_{\rm r}$ or for large spring constants k.

So far we have quantified the generated force by the most probable force $\eta_{\rm mp}$. The generated force can also be quantified by the average steady-state force $\langle\eta\rangle = \int_0^\infty \eta(x)P(x)dx$. Using the stationary distribution [eq. (4.23)] with normalization [eq. (4.24)] we can calculate $\langle\eta\rangle$; results are shown in Fig. 4.10 in comparison with the most probable force $\eta_{\rm mp}$, which is determined numerically from the maximum of $P(x)$, and the stall force $\eta_{\rm stall}$ in the absence of dynamic instability from eq. (2.14). For $\langle\eta\rangle$, there is excellent agreement with stochastic simulations over the complete range of parameter values. The results clearly show that the dynamic instability reduces the ability to generate polymerization forces since, even for large values of $\omega_{\rm on}$ and $\omega_{\rm r}$, the average force $\langle\eta\rangle$ is always smaller

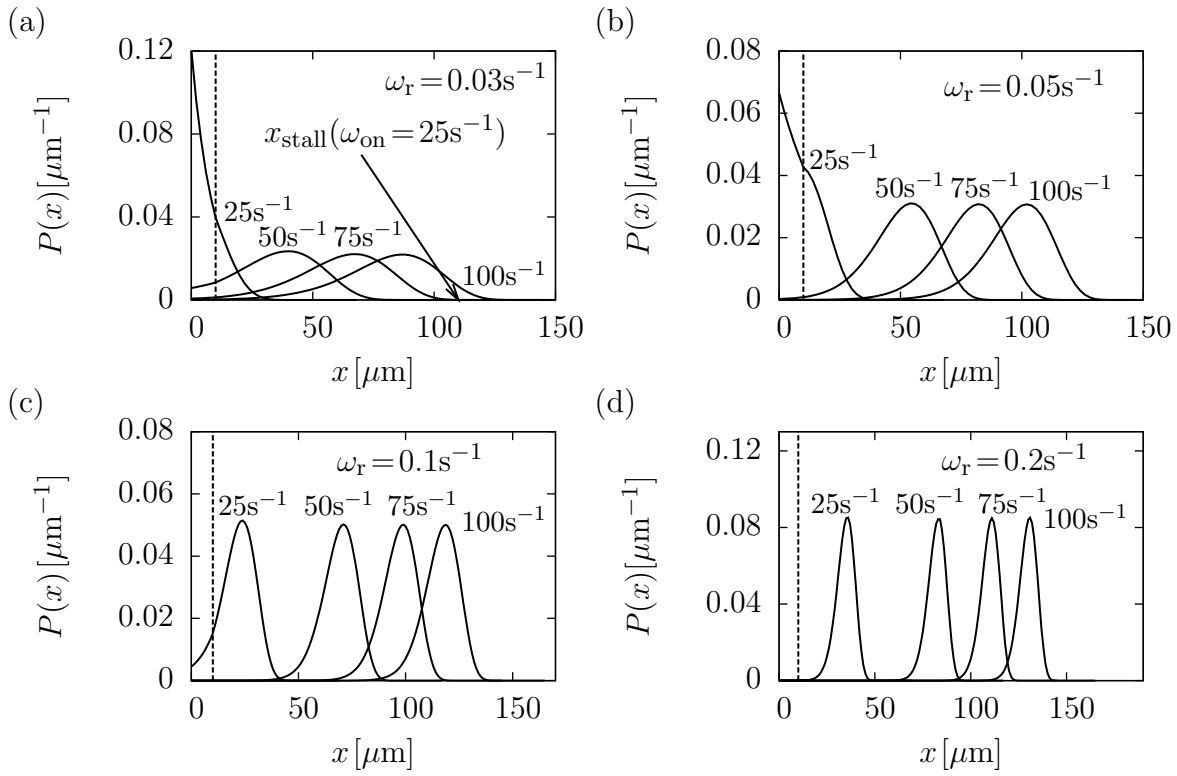

Figure 4.8: Stationary MT length distribution $P(x)$ in the steady state for growth against an elastic obstacle with $\omega_{on} = 25\,s^{-1}, 50\,s^{-1}, 75\,s^{-1}, 100\,s^{-1}$ and different values of ω_r. We set $k = 10^{-7}\,N/m$ and $x_0 = 10^{-5}\,m$. (a) $\omega_r = 0.03\,s^{-1}$. (b) $\omega_r = 0.05\,s^{-1}$. (c) $\omega_r = 0.1\,s^{-1}$. (d) $\omega_r = 0.2\,s^{-1}$. Dashed line represents x_0. In picture (a) the stall length x_{stall} for $\omega_{on} = 25\,s^{-1}$, obtained from simple polymerization kinetics, is indicated by an arrow.

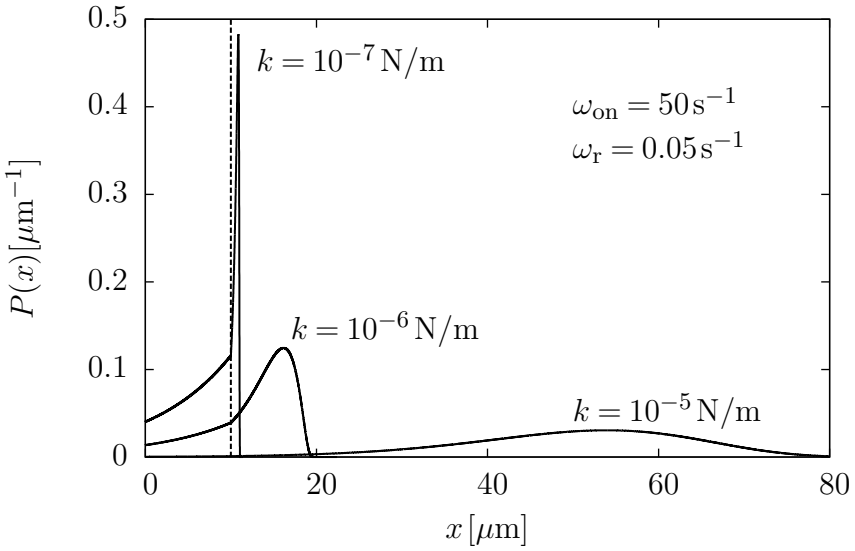

Figure 4.9: Steady state distribution $P(x)$ from eq. (4.23) for $\omega_{on} = 50\,s^{-1}$, $\omega_r = 0.05\,s^{-1}$ and different values of the spring constant k. Dashed line represents x_0.

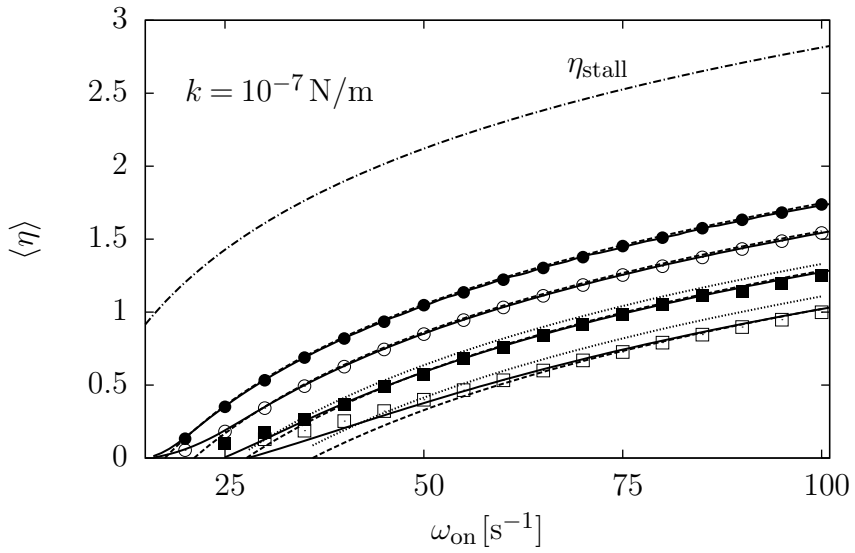

Figure 4.10: Average steady state force $\langle\eta\rangle$ as a function of ω_{on} for growth against an elastic obstacle with $\omega_r = 0.03\,s^{-1}(\boxdot), 0.05\,s^{-1}(\blacksquare), 0.1\,s^{-1}(\odot), 0.2\,s^{-1}(\bullet)$ and $k = 10^{-7}$N/m. Solid lines: $\langle\eta\rangle = \int_0^\infty \eta(x)P(x)dx$ with $P(x)$ given by eqs. (4.23) and (4.24). Dashed lines: $\langle\eta\rangle$ calculated from mean field equation (4.32). Dotted lines: most probable force η_{mp}, measured in simulations, for $\omega_r = 0.03\,s^{-1}$ and $\omega_r = 0.05\,s^{-1}$. Also shown is the dimensionless stall force η_{stall} obtained from simple polymerization kinetics [eq. (2.14)].

than the stall force. Nevertheless forces up to $F \sim 1.5\,F_0$ can be obtained in the steady state for realistic parameter values. Comparing $\langle\eta\rangle$ and η_{mp} we find $\langle\eta\rangle \leq \eta_{mp}$, and both forces become identical, $\langle\eta\rangle \approx \eta_{mp}$, in the limit of large rescue rates or a soft obstacle $kv_-/F_0\omega_r \ll 1$. Comparing different combinations of ω_{on} and ω_r and the corresponding forces, one finds that the influence of the on-rate ω_{on} on force generation is more significant than the influence of the rescue rate ω_r. For $\omega_{on} = 100\,s^{-1}$, a four fold increase of the rescue rate ω_r gives rise to an increase of $\langle\eta\rangle$ by a factor of ~ 1.5, while for $\omega_r = 0.1\,s^{-1}$, a four fold increase of the on-rate ω_{on} results in an amplification of the force $\langle\eta\rangle$ by a factor of ~ 9. These results can be explained within a mean field theory presented in the next section.

4.3.2.2 Mean field approach

In the following, we show that we can reproduce many of the results for the average polymerization force $\langle\eta\rangle$ for non-zero rescue rate using a simplified mean field approach. Since the switching between the two states of growth is a stochastic process, the length x and the force $\eta(x)$ are stochastic variables. Therefore, the velocity of growth $v_+[\eta(x)]$ and the catastrophe rate $\omega_c[\eta(x)]$ also become stochastic variables which, in the steady state, fluctuate around their average values. Within the mean field approach we neglect these fluctuations and use $\langle v_+[\eta(x)]\rangle = v_+(\langle\eta\rangle)$ and $\langle\omega_c[\eta(x)]\rangle = \omega_c(\langle\eta\rangle)$. In the mean field

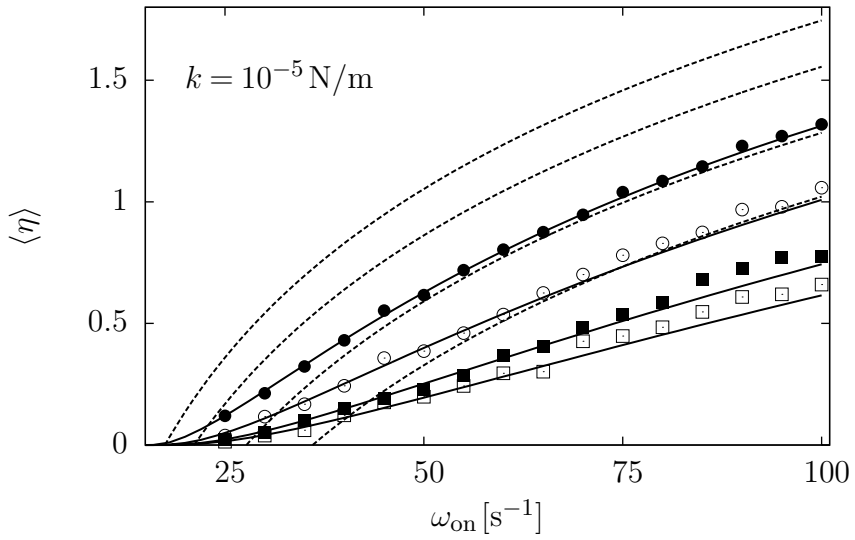

Figure 4.11: Average steady state force $\langle\eta\rangle$ as a function of ω_{on} for growth against an elastic obstacle with $\omega_{\mathrm{r}} = 0.03\,\mathrm{s}^{-1}(\boxdot), 0.05\,\mathrm{s}^{-1}(\blacksquare), 0.1\,\mathrm{s}^{-1}(\odot), 0.2\,\mathrm{s}^{-1}(\bullet)$ and $k = 10^{-5}\mathrm{N/m}$. Solid lines: $\langle\eta\rangle = \int_0^\infty \eta(x)P(x)dx$ with $P(x)$ given by eqs. (4.23) and (4.24). Dashed lines from bottom to top: $\langle\eta\rangle$ calculated from mean field equation (4.32) for $\omega_{\mathrm{r}} = 0.03\,\mathrm{s}^{-1}, 0.05\,\mathrm{s}^{-1}, 0.1\,\mathrm{s}^{-1}$, and $0.2\,\mathrm{s}^{-1}$.

approximation, the average time in the growing state is given by $1/\omega_{\mathrm{c}}(\langle\eta\rangle)$ and the average growth velocity is $v_+(\langle\eta\rangle)$. The average time in a shrinking state is $1/\omega_{\mathrm{r}}$. Therefore, the mean field probabilities to find the MT growing or shrinking are $p_+ = \omega_{\mathrm{r}}/[\omega_{\mathrm{r}} + \omega_{\mathrm{c}}(\langle\eta\rangle)]$ and $p_- = \omega_{\mathrm{c}}(\langle\eta\rangle)/[\omega_{\mathrm{r}} + \omega_{\mathrm{c}}(\langle\eta\rangle)]$, respectively. This results in the following mean field average velocity v of a single MT under force:

$$v(\langle\eta\rangle) = \frac{v_+(\langle\eta\rangle)\omega_{\mathrm{r}} - v_-\omega_{\mathrm{c}}(\langle\eta\rangle)}{\omega_{\mathrm{r}} + \omega_{\mathrm{c}}(\langle\eta\rangle)}. \tag{4.31}$$

In the steady state the barrier is pushed so far that $\langle\eta\rangle$ stalls the MT. We require $v(\langle\eta\rangle) = 0$ and obtain the condition

$$v_+(\langle\eta\rangle)\omega_{\mathrm{r}} = v_-\omega_{\mathrm{c}}(\langle\eta\rangle) \tag{4.32}$$

for the stationary state. This condition corresponds to a force, where the average length gain during growth, $v_+(\langle\eta\rangle)/\omega_{\mathrm{c}}(\langle\eta\rangle)$, equals the average length loss during shrinking, v_-/ω_{r}. From the mean field equation (4.32), the average steady state force, $\langle\eta\rangle$ can be calculated as a function of ω_{r} and ω_{on}. The average length $\langle x\rangle$ can be obtained from the relation $\langle\eta\rangle = (k/F_0)(\langle x\rangle - x_0)$. Results obtained from the mean field equation (4.32) match numerical results from stochastic simulations very well as shown in Fig. 4.10.

The mean field condition (4.32) is identical to the condition (4.12) for the critical force

η_c for MT dynamics under constant force such that

$$\langle \eta \rangle = \eta_c, \tag{4.33}$$

which can be interpreted as "self-organization" of the average MT length or the average force to the "critical" state. Therefore, the curves presented in Fig. 4.10 for $\langle \eta \rangle$ are identical to the curves shown in Fig. 4.4 for η_c.

This also allows us to take over the results we derived for the critical constant force η_c. Using the approximation of an exponentially decreasing growth velocity, $v_+[\eta(x)] \approx v_+(0)e^{-\eta(x)}$, which is valid for $\omega_{on} \gg \omega_{off}$ [see eq. (2.13)], and an exponentially increasing catastrophe rate above the characteristic force F_0, see eq. (2.37), we find

$$\langle \eta \rangle \sim \frac{1}{2} \ln \left(\frac{v_+(0)\omega_r}{v_-\omega_c(0)} \right). \tag{4.34}$$

which is identical to the result (4.12) for η_c.

Comparing with the stall force and the most probable force, we use relation (4.27) and find

$$\langle \eta \rangle = \eta_c \leq \eta_{mp} \ll \eta_{stall}. \tag{4.35}$$

In the limit of a soft obstacle, $kv_-/F_0\omega_r \ll 1$, the average force $\langle \eta \rangle$ approaches the most probable force $\langle \eta \rangle \approx \eta_{mp}$, whereas the mean field average force $\langle \eta \rangle$ is always smaller than the stall force η_{stall} in the absence of dynamic instability from eq. (2.14).

Finally, we discuss the limits of validity of the mean field approximation. The mean field approximation is based on the existence of a pronounced maximum in the stationary MT length distribution $P(x)$, which contains most of the weight of the probability density $P(x)$. It breaks down if this maximum broadens or vanishes, such that a considerable amount of probability density is shifted below x_0 into the regime of force-free growth. Then the MT typically shrinks into the force-free region $x < x_0$ during phases of shrinkage such that the growing phase explores the whole range of forces starting from $\eta = 0$ up to $\eta > \langle \eta \rangle$, and the approximation of a constant average force $\eta \approx \langle \eta \rangle$ during growth is no longer fulfilled. For small spring constants k or large values of ω_r, the length distribution $P(x)$ assumes a Gaussian shape with width σ, see eqs. (4.29) and (4.30). When k is increased for a fixed combination of ω_{on} and ω_r, the average length $\langle x \rangle$ approaches x_0 as $\langle x \rangle - x_0 \propto 1/k$, whereas the width σ of the length distribution only decreases as $\sigma \propto 1/\sqrt{k}$ in the regime of a soft obstacle $kv_-/F_0\omega_r \ll 1$, as can be seen from eq. (4.30). Therefore, an increasing amount of probability density is shifted below x_0, where no force is acting on the MT ensemble (see Figs. 4.8(a) and 4.9). The mean field approximation is only valid for spring constants k which fulfill $\langle x \rangle - x_0 \gg \sigma/2$ for given parameters ω_{on} and ω_r.

With $\langle\eta\rangle = (k/F_0)(\langle x\rangle - x_0)$ this is equivalent to a condition

$$\langle\eta\rangle \gg \frac{k\sigma}{2F_0} \approx \frac{1}{2}\left(1+\frac{2F_0\omega_\mathrm{r}}{kv_-}\right)^{-1/2} \tag{4.36}$$

according to eq. (4.30). This condition can only be fulfilled in the limit of a *soft* obstacle with $kv_-/F_0\omega_\mathrm{r} \ll 1$. For the validity of the mean field approximation we therefore recover the condition that the average length loss during a period of shrinkage, v_-/ω_r, is much smaller than the typical displacement F_0/k of the elastic obstacle under the characteristic force F_0. Then the MT tip always remains in the region $x > x_0$ under the influence of the force.

4.3.2.3 Dilution dynamics

Within the mean field approach we can also derive an analytical time evolution of the average time-dependent force $\langle\eta\rangle(t)$. The time evolution is based on eq. (4.31), which gives a mean field approximation for the average MT velocity $v(\langle\eta\rangle)$ as a function of the average force. On the other hand, the average MT growth velocity is related to the time derivative of the average force by

$$\frac{d}{dt}\langle\eta\rangle = \frac{k}{F_0}\frac{d}{dt}\langle x\rangle = \frac{k}{F_0}v(\langle\eta\rangle). \tag{4.37}$$

Using eq. (4.31) for $v(\langle\eta\rangle)$, this gives a mean field equation of motion for $\langle\eta\rangle(t)$ similar to eq. (4.15) in the absence of rescue events. Integrating this equation numerically we obtain mean field trajectories for the average force $\langle\eta\rangle(t)$ as a function of time t. Figs. 4.12 shows such trajectories for $k = 10^{-7}\mathrm{N/m}$ and a initial condition $\langle\eta\rangle(0) = 0$ at $t = 0$. Also shown in Figs. 4.12 are results from stochastic simulations, which show excellent agreement with the mean field trajectories.

We now address the question of how fast a single MT responds to external changes of one of its growth parameters. Here we focus on fast dilution of the tubulin concentration, which is directly related to the tubulin on-rate ω_on. *In vivo*, the tubulin concentration can be changed by tubulin binding proteins like stathmin [28], while in *in vitro* experiments, the tubulin concentration can be diluted within seconds [84]. In the following we give a mean field estimate of the typical time scale, which governs the return dynamics of the MT back to a new steady state after the tubulin on-rate is suddenly decreased. In the initial steady state the average velocity $v(\langle\eta\rangle_i)$ vanishes and the average polymerization force $\langle\eta\rangle_i$ (and, thus, the average length $\langle x\rangle_i$) can be calculated from the condition $v_+(\langle\eta\rangle_i)\omega_\mathrm{r} = v_-\omega_\mathrm{c}(\langle\eta\rangle_i)$, cf. eq. (4.32), for a given combination of ω_on and ω_r. If ω_on is suddenly decreased this leads to a sudden decrease in the growth velocity to $\widetilde{v}_+(\eta) < v_+(\eta)$ and an increase of the catastrophe rate to $\widetilde{\omega}_\mathrm{c}(\eta) > \omega_\mathrm{c}(\eta)$, resulting in a negative average velocity

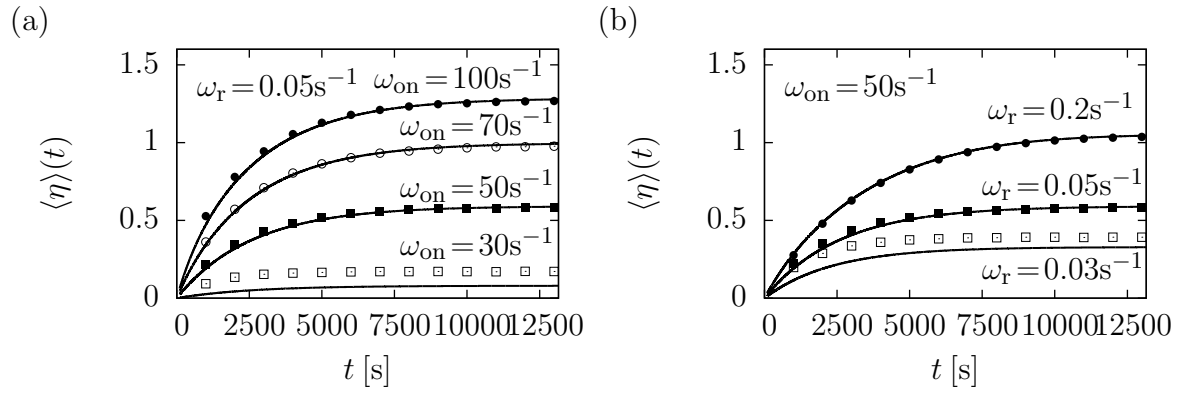

Figure 4.12: (a): Average force $\langle\eta\rangle(t)$ as a function of time t for $k = 10^{-7}\,\text{N/m}$, $\omega_r = 0.05\,\text{s}^{-1}$, and $\omega_{on} = 30, 50, 75, 100\,\text{s}^{-1}$. Symbols: time-dependent average force $\langle\eta\rangle(t)$ measured in simulations. Solid lines: time-dependent average force trajectories calculated from eq. (4.37). (b): Average force $\langle\eta\rangle(t)$ as a function of time t for $k = 10^{-7}\,\text{N/m}$, $\omega_{on} = 50\,\text{s}^{-1}$, and $\omega_r = 0.03, 0.05, 0.2\,\text{s}^{-1}$. Symbols: time dependent average force $\langle\eta\rangle(t)$ measured in simulations. Solid lines: time-dependent average force trajectories calculated from eq. (4.37).

$v(\langle\eta\rangle) = [\tilde{v}_+(\langle\eta\rangle)\omega_r - v_-\tilde{\omega}_c(\langle\eta\rangle)]/[\omega_r + \tilde{\omega}_c(\langle\eta\rangle)] < 0$ according to eq. (4.31). Consequently, the MT starts to shrink with an average velocity $v(\langle\eta\rangle) < 0$. This relaxes the force from the elastic obstacle, i.e., $\langle\eta\rangle(t)$ starts to decrease from the initial value $\eta_i \equiv \langle\eta\rangle_i$. With decreasing average force $\langle\eta\rangle(t)$, the average growth velocity $v(\langle\eta\rangle(t))$ increases again (because $\tilde{v}_+$ increases and $\tilde{\omega}_c$ decreases) until the steady state condition $\tilde{v}_+(\langle\eta\rangle_f)\omega_r = v_-\tilde{\omega}_c(\langle\eta\rangle_f)$ holds again and a new steady state force $\langle\eta\rangle_f < \langle\eta\rangle_i$ is reached (see Fig. 4.13).

The relaxation dynamics to the new steady state after tubulin dilution is therefore governed by the average velocity $v(\langle\eta\rangle)$ given by eq. (4.31). To extract a characteristic relaxation time scale, we expand the average velocity $v(\langle\eta\rangle)$ to first order around the final steady-state polymerization force $\eta_f \equiv \langle\eta\rangle_f$, which is the solution of eq. (4.32) with ω_r and the decreased tubulin on-rate ω_{on}, which takes its dilution value. Using $v(\eta_f) = 0$ one finds in first order

$$v(\langle\eta\rangle) \approx -\left[\frac{v_+(\eta_f)\omega_r + v_-\omega_c'(\eta_f)}{\omega_r + \omega_c(\eta_f)}\right](\langle\eta\rangle - \eta_f) \tag{4.38}$$

where the prime denotes the derivative with respect to the force η. In the last approximation we used the mean field condition eq. (4.32) and $v_+[\eta(x)] \approx v_+(0)e^{-\eta(x)}$, which is valid for $\omega_{on} \gg \omega_{off}$ [see eq. (2.13)]. This expansion is only valid for average forces close to the new average polymerization force η_f. Using this expansion, the time evolution (4.37) of the average force after dilution exhibits an exponential decay

$$\langle\eta\rangle(t) = \eta_f + (\eta_i - \eta_f)e^{-t/\tau_d} \tag{4.39}$$

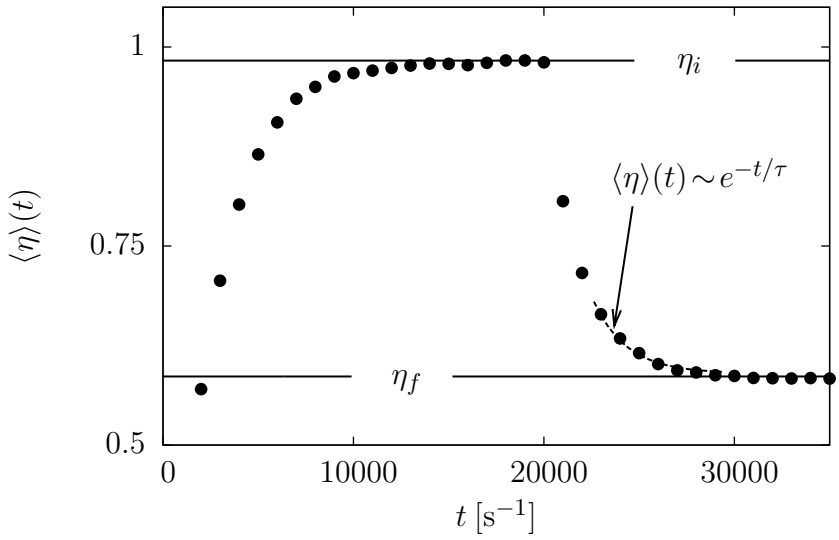

Figure 4.13: Average force $\langle\eta\rangle(t)$ as a function of time t. Symbols are results obtained from simulations. We set $k = 10^{-7}\,\mathrm{N/m}$, $\omega_\mathrm{r} = 0.05\,\mathrm{s}^{-1}$ and $\omega_\mathrm{on} = 75\,\mathrm{s}^{-1}$. At $t = 20000\,\mathrm{s}$, ω_on is diluted down to $\omega_\mathrm{on} = 50\,\mathrm{s}^{-1}$. Dashed line represents a fit with an exponential decay (4.39) to the simulated data with fit parameter $\tau_\mathrm{d} \approx 1762\,\mathrm{s}$. Solid lines indicate the average force in the initial state η_i before dilution and in the new final state η_f after dilution.

with a characteristic dilution time scale

$$\tau_\mathrm{d} = \frac{F_0}{k}\frac{\omega_\mathrm{r} + \omega_\mathrm{c}(\eta_\mathrm{f})}{v_+(\eta_\mathrm{f})\omega_\mathrm{r} + v_-\omega_\mathrm{c}'(\eta_\mathrm{f})} \approx \frac{F_0}{k}\frac{\omega_\mathrm{r} + \omega_\mathrm{c}(\eta_\mathrm{f})}{2v_-\omega_\mathrm{c}(\eta_\mathrm{f})} \tag{4.40}$$

where we approximated the catastrophe rate by an exponential $\omega_\mathrm{c}[\eta(x)] \approx \omega_\mathrm{c}(0)e^{\eta(x)}$ according to eq. (2.37), and we used the mean field condition eq. (4.32). In the limit $\omega_\mathrm{c}(\eta_\mathrm{f}) \gg \omega_\mathrm{r}$, i.e., at forces $\eta_\mathrm{f} \gg 1$, we obtain the simple result $\tau_\mathrm{d} \approx F_0/2v_-k$. In general, the relaxation time τ_d is proportional to the square σ^2 of the width of the stationary distribution, cf. eq. (4.30). A narrow length distribution gives rise to fast relaxation to the new average force.

A fit of eq. (4.39) to simulated data results in $\tau_\mathrm{d} \approx 1762\,\mathrm{s}$ (see Fig. 4.13), while eq. (4.40) yields $\tau_\mathrm{d} \approx 2766\,\mathrm{s}$. Results for τ_d match well in their order of magnitude, but slightly differ in their absolute values, due to the exponential approximation of $v_+(\eta)$ and $\omega_\mathrm{c}(\eta)$.

4.4 Experimental and linear catastrophe model

So far we have employed the catastrophe rate derived by Flyvbjerg *et al.*, to which we will refer as $\omega_\mathrm{c,Flyv}$ in the following. This expression for the catastrophe rate was based on theoretical calculations of the inverse passage time to a state with a vanishing GTP-cap, see Sec. 2.3 and eq. (2.35). In order to investigate the robustness of our results with

respect to changes of the catastrophe model, we now investigate two alternative expression for the catastrophe rate, the experimental catastrophe rate $\omega_{\mathrm{c,Jans}}$ by Janson *et al.* (see Sec. 2.3) and the linear catastrophe rate $\omega_{\mathrm{c,lin}}$ (see Sec. 2.3). Throughout this section, we focus on the third confinement scenario of an elastic obstacle, and we compare results from the different catastrophe models for zero rescue rate $\omega_{\mathrm{r}} = 0$ and non-zero rescue rate $\omega_{\mathrm{r}} > 0$.

We start with the catastrophe model by Janson *et al.* (Sec. 4.4.1) and subsequently discuss the linear catastrophe model (Sec. 4.4.2).

4.4.1 Experimental catastrophe model by Janson *et al.*

4.4.1.1 Vanishing rescue rate

We begin with the case $\omega_{\mathrm{r}} = 0$ without rescue events, and we calculate the average maximal polymerization force within the experimental catastrophe model using the self-consistent mean field eq. (4.18), which holds independently of the choice of catastrophe model (see Sec. 4.3.1). As for the catastrophe by Flyvbjerg *et al.*, we have $\omega_{\mathrm{c,Jans}}\tau \gg 1$ for realistic parameter values and $v_+(\langle\eta\rangle) < -b/a$, and eq. (4.18) can be solved explicitly for $\langle\eta_{\max}\rangle$ in this limit. We find an average maximal polymerization force

$$\langle\eta_{\max}\rangle \approx \ln\left(\left[\left(A^2+B\right)^{1/2} - A\right]\right) \tag{4.41}$$

with

$$A \equiv \frac{(\omega_{\mathrm{on}}/\omega_{\mathrm{off}} - 1)ad\omega_{\mathrm{off}} - (\omega_{\mathrm{on}}/\omega_{\mathrm{off}} - 1)b - \tau}{2\tau}$$
$$B \equiv \frac{(\omega_{\mathrm{on}}/\omega_{\mathrm{off}} - 1)ad\omega_{\mathrm{on}}}{\tau}.$$

Since $\omega_{\mathrm{on}}/\omega_{\mathrm{off}} \gg 1$, eq. (4.41) can be approximated by

$$\langle\eta_{\max}\rangle \approx \ln\left(\omega_{\mathrm{on}}/\omega_{\max}\right) \tag{4.42}$$

with

$$\omega_{\max} \equiv \frac{2\tau\omega_{\mathrm{off}}}{\left[\left(ad\omega_{\mathrm{off}} - b\right)^2 + 4ad\omega_{\mathrm{off}}\tau\right]^{1/2} - \left[ad\omega_{\mathrm{off}} - b\right]} \tag{4.43}$$

and $\tau = F_0/(dk\omega_{\mathrm{off}})$ as in Sec. 4.3.1. For realistic parameter values, we have $\tau \gg ad\omega_{\mathrm{off}} \geq b$, and recover the expression (4.20) derived using the Flyvbjerg catastrophe model:

$$\langle\eta_{\max}\rangle \approx \frac{1}{2}\ln\left(\frac{\omega_{\mathrm{on}}^2 ad}{\omega_{\mathrm{off}}\tau}\right) \approx \frac{1}{2}\ln\left(\frac{\omega_{\mathrm{on}} dk}{F_0\omega_{\mathrm{c,Jans}}(0)}\right). \tag{4.44}$$

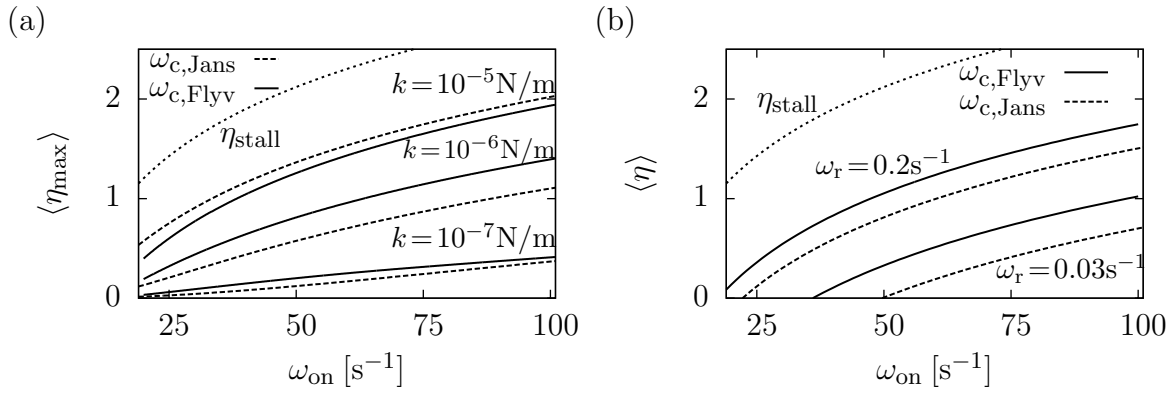

Figure 4.14: (a): Average maximal polymerization force $\langle \eta_{max} \rangle$ as a function of ω_{on} and $\omega_r = 0$ for $k = 10^{-7}$ N/m, 10^{-6} N/m and 10^{-7} N/m (top to bottom). Dotted line: dimensionless stall force η_{stall}. Solid lines: $\langle \eta_{max} \rangle$ obtained with $\omega_{c,Flyv}$ [eq. (4.18)]. Dashed lines: $\langle \eta_{max} \rangle$ obtained with $\omega_{c,Jans}$ [eq. (4.41)]. (b): Average steady state force $\langle \eta \rangle$ as a function of ω_{on}. We set $k = 10^{-7}$ N/m, $\omega_r = 0.2\,s^{-1}$ (top) and $\omega_r = 0.03\,s^{-1}$(bottom). Solid lines: $\langle \eta \rangle$ obtained with $\omega_{c,Flyv}$ [eq. (4.32)]. Dashed lines: $\langle \eta \rangle$ obtained with $\omega_{c,Jans}$ [eq. (4.45)]. Dotted line: dimensionless stall force η_{stall}.

In Fig. 4.14 (a), $\langle \eta_{max} \rangle$ as obtained from eq. (4.18) with the Flyvbjerg catastrophe model and eq. (4.41) with the experimental catastrophe model are shown as a function of ω_{on}. Results match qualitatively and quantitatively well, although they are obtained from two different catastrophe models. The maximal polymerization force $\langle \eta_{max} \rangle$ always remains smaller than the stall force η_{stall}.

4.4.1.2 Non-zero rescue rate

We calculate the OPDF $P(x)$ in the steady state from eq. (4.23) with the experimental catastrophe rate $\omega_{c,Jans}(\eta)$ given by eq. (2.38). In Fig. 4.15 results for $\omega_r = 0.2\,s^{-1}$, $k = 10^{-7}$ N/m and $\omega_{on} = 25, 50, 75, 100\,s^{-1}$ are shown.

For a soft spring constant $k = 10^{-7}$ N/m the OPDFs are sharply peaked. In Sec. 4.3.2 we discussed the characteristics of this sharply peaked OPDFs in detail within the context of the catastrophe model by Flyvbjerg *et al.* In particular, for a soft spring constant k, results from full stochastic calculations can be reproduced by a simplified mean field theory (see Sec. 4.3.2.2). This mean field approach is based on a pronounced maximum in the stationary MT length distribution $P(x)$. As we find sharply peaked OPDFs for the experimental catastrophe rate $\omega_{c,Jans}$ by Janson *et al.*, we restrict our further analysis to mean field results.

For the experimental catastrophe rate [eq. (2.38)], the mean field equation (4.32) can be solved explicitly, and the average steady-state force $\langle \eta \rangle$ is given by

$$\langle \eta \rangle = \ln(\omega_{on}/\omega_{av}), \tag{4.45}$$

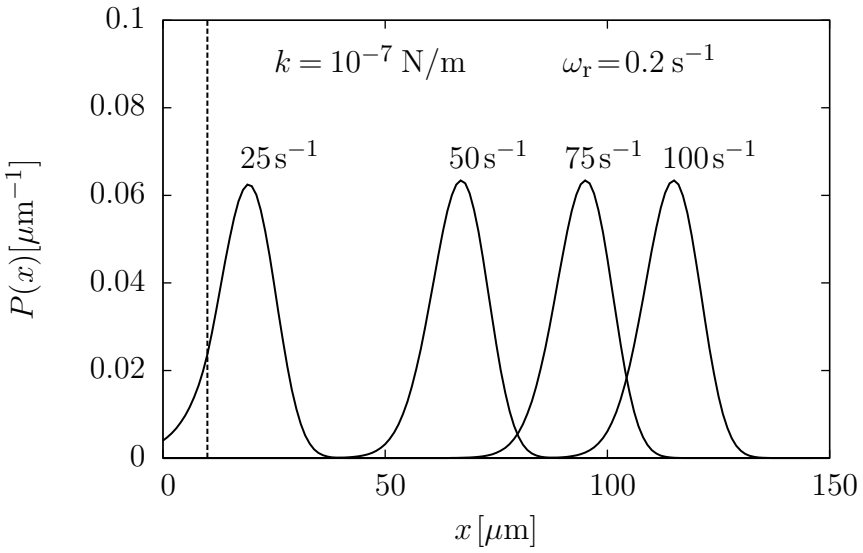

Figure 4.15: Stationary MT length distribution $P(x)$ for growth against an elastic obstacle from eq. (4.23) and with the experimental catastrophe rate $\omega_{\mathrm{c,Jans}}$ [eq. (2.38)]. We set $k = 10^{-7}\,\mathrm{N/m}$, $x_0 = 10^{-5}\,\mathrm{m}$ (dashed line) and $\omega_\mathrm{r} = 0.2\,\mathrm{s}^{-1}$. Results for $\omega_\mathrm{on} = 25\,\mathrm{s}^{-1}, 50\,\mathrm{s}^{-1}, 75\,\mathrm{s}^{-1}, 100\,\mathrm{s}^{-1}$ are shown.

with

$$\omega_\mathrm{av} \equiv \left[\left(\frac{b}{2ad}\right)^2 + \frac{v_-}{\omega_\mathrm{r} a d^2}\right]^{1/2} - \frac{b}{2ad} + \omega_\mathrm{off} \tag{4.46}$$

Again $\langle\eta\rangle < \eta_\mathrm{stall}$ since $\omega_\mathrm{av} > \omega_\mathrm{off}$. Fig. 4.14 (b) show $\langle\eta\rangle$ as a function of ω_on. For realistic parameter values, we have $v_-/\omega_\mathrm{r} \gg b^2/a$ and $(v_-/\omega_\mathrm{r} a d^2)^{1/2} \gg \omega_\mathrm{off}$, and we recover the expression (4.34) derived using the Flyvbjerg catastrophe model:

$$\langle f\rangle \approx \frac{1}{2}\ln\left(\frac{\omega_\mathrm{on}^2 \omega_\mathrm{r} a d^2}{v_-}\right) \approx \frac{1}{2}\ln\left(\frac{v_+(0)\omega_\mathrm{r}}{v_-\omega_{\mathrm{c,Jans}}(0)}\right). \tag{4.47}$$

In Fig. 4.14(b), results for $\langle\eta\rangle$ from both catastrophe models are shown as a function of on-rate ω_on. The average steady state force obtained from $\omega_{\mathrm{c,Flyv}}$ is always slightly larger than $\langle\eta\rangle$ obtained from $\omega_{\mathrm{c,Jans}}$, since $\omega_{\mathrm{c,Jans}}(\eta) > \omega_{\mathrm{c,Flyv}}(\eta)$ for forces smaller than or comparable to F_0. Otherwise, both results agree qualitatively and quantitatively well.

4.4.2 Linear catastrophe model

Now results obtained with the linear catastrophe rate $\omega_{\mathrm{c,lin}}$ are discussed. All calculations are carried with the catastrophe rate parameters $\widetilde{a} = 0.005\,\mathrm{s}$ and $\widetilde{b} = 8 \times 10^4\,\mathrm{m}^{-1}$. Since $\widetilde{a}$ and $\widetilde{b}$ are determined from experimental data, which do not support a linear catastrophe rate, the choice of $\widetilde{a}$ and $\widetilde{b}$ is rather arbitrary. We want to stress out that, another choice of $\widetilde{a}$ and $\widetilde{b}$ may affect the validity of approximations and lead to essential differences in the final results.

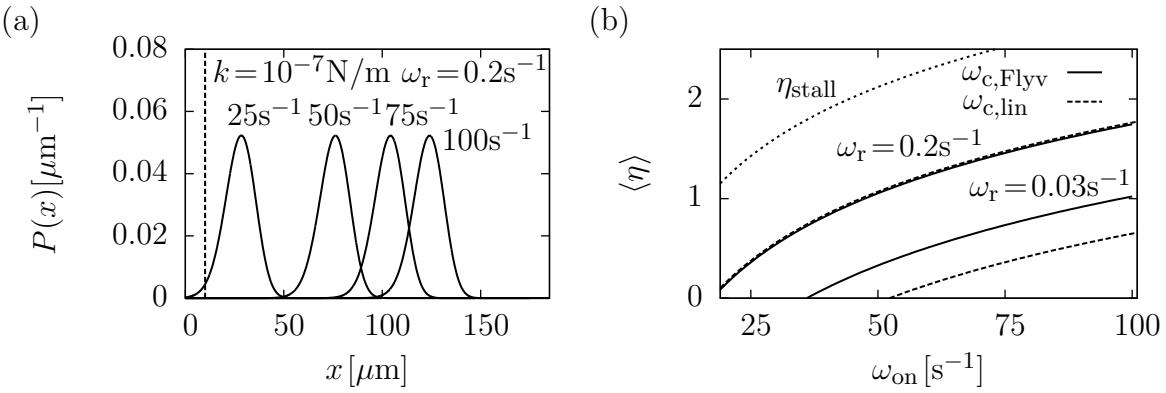

Figure 4.16: (a): Stationary MT length distribution $P(x)$ for growth against an elastic obstacle from eq. (4.23) and with the linear catastrophe rate $\omega_{\mathrm{c,lin}}$ (see eq. (2.40)). We set $k=10^{-7}\,\mathrm{N/m}$, $x_0=10^{-5}\,\mathrm{m}$ (dashed line) and $\omega_\mathrm{r}=0.2\,\mathrm{s}^{-1}$. Results for $\omega_\mathrm{on}=25\,\mathrm{s}^{-1},50\,\mathrm{s}^{-1},75\,\mathrm{s}^{-1},100\,\mathrm{s}^{-1}$ are shown. (b): Average steady state force $\langle\eta\rangle$ as a function of ω_on. We set $k=10^{-7}\,\mathrm{N/m}$, $\omega_\mathrm{r}=0.2\,\mathrm{s}^{-1}$ (top) and $\omega_\mathrm{r}=0.03\,\mathrm{s}^{-1}$(bottom). Solid lines: $\langle\eta\rangle$ obtained with $\omega_{\mathrm{c,Flyv}}$ [eq. (4.32)]. Dashed lines: $\langle\eta\rangle$ obtained with $\omega_{\mathrm{c,lin}}$ [eq. (4.48)]. Dotted line: dimensionless stall force η_stall.

4.4.2.1 Vanishing rescue rate

We start with $\omega_\mathrm{r}=0$, and we calculate the average maximal polymerization force within the linear catastrophe model using the self-consistent mean field eq. (4.18), which holds independently of the choice of catastrophe model (see Sec. 4.3.1). Equation (4.18) is solved numerically. For all investigated sets of parameter values, we find $\langle\eta_\mathrm{max}\rangle>\eta_\mathrm{stall}$. The average maximal polymerization force exceeds the stall force. This is an artifact of the linear catastrophe model, which does not increase exponentially for forces larger than the characteristic force F_0, but remains constant. Due to this fact, eq. (4.18) only yields a non-physical fixed point. We do not further discuss the linear catastrophe model in the absence of rescue events, but we want to stress out, that a different choice of the catastrophe parameters $\tilde{a}$ and $\tilde{b}$ may lead to more reasonable results.

4.4.2.2 Non-zero rescue rate

We calculate the OPDF $P(x)$ in the steady state from eq. (4.23) with the linear catastrophe rate $\omega_{\mathrm{c,lin}}(\eta)$ given by eq. (2.40). In Fig. 4.16 results for $\omega_\mathrm{r}=0.2\,\mathrm{s}^{-1}$, $k=10^{-7}\,\mathrm{N/m}$ and different values of ω_on are shown.

Again we find sharply peaked OPDFs and restrict further discussions to mean field results (see Sec. 4.3.2 and Sec. 4.4.1.2).

For the linear catastrophe rate [eq. (2.40)], the mean field equation (4.32) can be solved explicitly, and the average steady-state force $\langle\eta\rangle$ is given by

$$\langle\eta\rangle=\ln\left(\omega_\mathrm{on}/\omega_\mathrm{lin}\right), \tag{4.48}$$

with

$$\omega_{\text{lin}} = \frac{\widetilde{a}v_-}{d\left(\omega_{\text{r}} + \widetilde{b}v_-\right)} + \omega_{\text{off}}. \tag{4.49}$$

Again $\langle\eta\rangle < \eta_{\text{stall}}$ since $\omega_{\text{lin}} > \omega_{\text{off}}$. Fig. 4.16(b) shows $\langle\eta\rangle$ as a function of ω_{on}. For realistic parameter values, we have $\omega_{\text{on}}/\omega_{\text{off}} > 1$ and $\widetilde{b}v_-/\omega_{\text{r}} < 1$ and, as with the Flyvbjerg and the Janson model, we recover expression (4.34)

$$\langle\eta\rangle \approx \ln\left(\frac{v_+(0)\omega_{\text{r}}}{v_-\omega_{\text{c,lin}}(0)}\right), \tag{4.50}$$

except from a factor 1/2.

In Fig. 4.16(b), results for $\langle\eta\rangle$ obtained with $\omega_{\text{c,lin}}$ and $\omega_{\text{c,Flyv}}$ are shown as a function of on-rate ω_{on}. The average steady state force obtained from $\omega_{\text{c,lin}}$ is always slightly smaller than $\langle\eta\rangle$ obtained from $\omega_{\text{c,Flyv}}$, but approaches $\langle\eta\rangle$ obtained from $\omega_{\text{c,Flyv}}$ for large rescue rates. Again both results agree qualitatively and quantitatively well.

4.5 Generalized force-velocity relation

We now discuss the influence of the force-velocity relation on the MT dynamics. A change in the force-velocity relation directly modifies the velocity of growth $v_+(\eta)$, but it also affects the catastrophe rate $\omega_{\text{c}}[v_+(\eta)]$, which are both crucial parts of the MT dynamics. In the following, we employ the more generalized force-velocity relation by Kolomeisky *et al.* (see Sec. 2.2). Throughout this section, we focus on the third confinement scenario of an elastic obstacle, and show that our results are robust with respect to this generalization. We discuss both cases of vanishing and non-vanishing rescue rate.

4.5.1 Vanishing rescue rate

We use the generalized force-velocity relation $v_+(\eta,\theta)$ given by eq. (2.15) and the catastrophe rate $\omega_{\text{c,Flyv}}(\eta)$ by Flyvbjerg *et al.* in order to calculate the average maximal polymerization force $\langle\eta_{\text{max}}\rangle$ from the self-consistent mean field eq. (4.18). In Fig. 4.17 (a), $\langle\eta_{\text{max}}\rangle$ is shown as a function of the load distribution factor θ for $k = 10^{-5}\,\text{N/m}$ and different values of ω_{on}. At $\theta = 1$, the maximal force $\langle\eta_{\text{max}}\rangle$ equals the maximal polymerization force obtained with $v_+(\eta)$ from eq. (2.13). With decreasing θ, $\langle\eta_{\text{max}}\rangle$ increases but remains below the dimensionless stall force. The growth velocity $v_+(\eta,\theta)$ increases with decreasing θ for a fixed force η and, therefore, the maximal polymerization force $\langle\eta_{\text{max}}\rangle$ increases. For high tubulin on-rates $\omega_{\text{on}} = (75-100)\,\text{s}^{-1}$ and small $\theta \approx 0,\ldots,0.2$, the maximal polymerization force $\langle\eta_{\text{max}}\rangle$ approaches the dimensionless stall force.

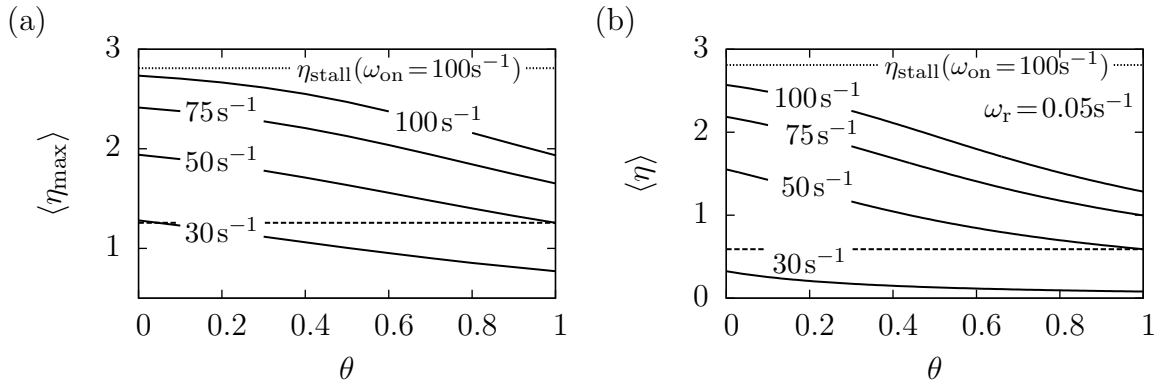

Figure 4.17: (a): Solid lines: Average maximal polymerization force $\langle\eta_{\max}\rangle$ as a function of θ for $k=10^{-5}\,\text{N/m}$ and different values of ω_{on}. Dotted line: Dimensionless stall force η_{stall} for $\omega_{\text{on}}=100\,\text{s}^{-1}$. Dashed line: $\langle\eta_{\max}\rangle$ for $\omega_{\text{on}}=50\,\text{s}^{-1}$ and $v_+(\theta=1)$ corresponding to eq. (2.11). (b): Solid lines: Average steady state force $\langle\eta\rangle$ as a function of θ for $k=10^{-7}\,\text{N/m}$, $\omega_{\text{r}}=0.05\,\text{s}^{-1}$ and different values of ω_{on}. Dotted line: Dimensionless stall force η_{stall} for $\omega_{\text{on}}=100\,\text{s}^{-1}$. Dashed line: $\langle\eta\rangle$ for $\omega_{\text{on}}=50\,\text{s}^{-1}$ and $v_+(\theta=1)$ corresponding to eq. (2.11).

4.5.2 Non-zero rescue rate

We calculate the OPDF $P(x)$ in the steady state from eq. (4.23) with the force-velocity relation $v_+(\eta,\theta)$ [eq. (2.15] and the catastrophe rate $\omega_{\text{c,Flyv}}(\eta)$ by Flyvbjerg *et al.* [eq. (2.35)]. In Fig. 4.18 results for $\omega_{\text{on}}=50\,\text{s}^{-1}$, $\omega_{\text{r}}=0.05\,\text{s}^{-1}$ and $k=10^{-7}\,\text{N/m}$ are shown. Again we find sharply peaked OPDFs and restrict further discussions to mean field results (see Sec. 4.3.2 and Sec. 4.4.1.2).

For non-zero rescue rate, the average steady state force $\langle\eta\rangle$ is calculated from the mean field eq. (4.32), where we use the force-velocity relation $v_+(\eta,\theta)$ [eq. (2.15)] and the catastrophe rate $\omega_{\text{c,Flyv}}(\eta)$ by Flyvbjerg *et al.* In Fig. 4.17(b), results for $\langle\eta\rangle$ are shown as a function of θ for $k=10^{-7}\,\text{N/m}$, $\omega_{\text{r}}=0.05\,\text{s}^{-1}$ and different values of ω_{on}. At $\theta=1$, $\langle\eta\rangle$ equals the average steady state force obtained with a velocity $v_+(\eta)$ taken from eq. (2.13). The average steady state force $\langle\eta\rangle$ increases with decreasing θ, as explained above. For high tubulin on-rates $\omega_{\text{on}}=(75-100)\,\text{s}^{-1}$ and small $\theta\approx 0,\ldots,0.2$, also the average steady state force $\langle\eta\rangle$ again approaches the dimensionless stall force but remains smaller.

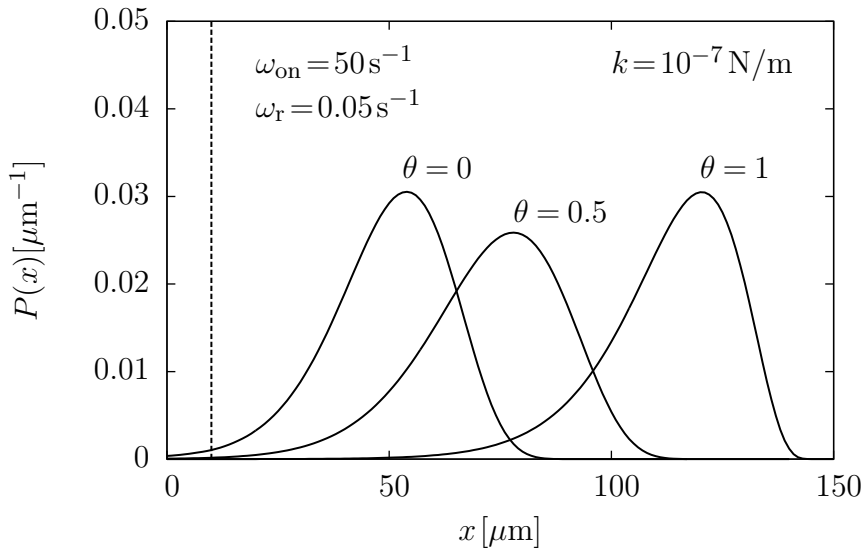

Figure 4.18: Stationary MT length distribution $P(x)$ for growth against an elastic obstacle from eq. (4.23), with the catastrophe rate $\omega_{\mathrm{c,Flyv}}$ [eq. (2.35)] and the generalized force-velocity relation by Kolomeisky *et al.* [eq. (2.15)]. We set $k = 10^{-7}\,\mathrm{N/m}$ and $x_0 = 10^{-5}\,\mathrm{m}$ (dashed line). Results for $\omega_{\mathrm{on}} = 50\,\mathrm{s}^{-1}$, $\omega_{\mathrm{r}} = 0.05\,\mathrm{s}^{-1}$ and $\theta = 0, 0.5, 1$ are shown.

Chapter 5

First conclusion [1]

We studied single MT dynamics in three different confining scenarios: (i) confinement by fixed rigid walls (Sec. 4.1), (ii) an open system under constant force (Sec. 4.2), and (iii) MT growth against an elastic obstacle with a force that depends linearly on MT length (Sec. 4.3). These three scenarios represent generic confinement scenarios in living cells or geometries, which can be realized experimentally *in vitro*. For all three scenarios, we are able to quantify the MT length distributions as a function of growth parameters and the load force.

The parameter λ, see eq. (2.4) governs the MT length distributions in confinement by fixed rigid walls. For confinement by rigid walls we introduced a realistic model for wall-induced catastrophes, which in most cases can been seen as instantaneous. There is a transition from exponentially increasing ($\lambda > 0$) to exponentially decreasing ($\lambda < 0$) length distributions if λ changes sign. The average MT length is increasing for increasing on-rate ω_{on} and increasing rescue rate ω_{r}, as shown in Figs. 4.2. Wall-induced catastrophes lead to an overall increase in the average catastrophe frequency, which we quantify within the model.

The parameter $\lambda(\eta)$, see eq. (4.11), governs the MT length distributions for growth under constant force. For MT growth under a constant force, there exists a transition between bounded and unbounded growth as in the absence of force, with exponentially decaying and Gaussian-shaped OPDFrespectively. This transition takes place where the parameter $\lambda(\eta)$ changes sign and determines the critical force η_{c}. We determined the critical force η_{c} as function of the on-rate ω_{on} and the rescue rate ω_{r} (see Fig. 4.4). Under force, the transition to unbounded growth is shifted to higher values of ω_{on} or higher rescue rates (see Figs. 4.5).

In scenario of an elastic obstacle, stochastic MT growth also gives rise to a stochastic force. For this model, we also quantify the average polymerization force generated by the MT in the presence of the dynamic instability. MT growth under a MT length-dependent linear

[1] Parts of the text have been published in reference [55] and is ©2012 American Physical Society. http://publish.aps.org/copyrightFAQ.html

elastic force allows for regulation of the generated polymerization force by experimentally accessible parameters such as the on-rate, the rescue rate or the stiffness of the elastic barrier. The force is no longer fixed but a stochastically fluctuating quantity because the MT length is a stochastic quantity.

For zero rescue rate, i.e., in the absence of rescue events, we find that the average maximal polymerization force $\langle \eta_{\max} \rangle$ before a catastrophe depends logarithmically on the tubulin concentration and is always smaller than the stall force in the absence of dynamic instability as shown in Fig. 4.7. The average maximal polymerization force and its logarithmic dependency on the tubulin concentration should be accessible in *in vitro* experiments.

For a non-zero rescue rate, we find a steady state length distribution, which becomes increasingly sharply peaked for increasing rescue rate and is tightly controlled by microtubule growth parameters, see Figs. 4.8. Interestingly, the average microtubule length self-organizes such that the average steady state polymerization force $\langle \eta \rangle$ equals the critical force for the boundary of bounded and unbounded growth, $\langle \eta \rangle = \eta_c$. Because of the sharply peaked MT length distribution, the average polymerization force $\langle \eta \rangle$ can be calculated rather accurately within a mean field approach as can be seen in Figs. 4.10 and 4.11. The average polymerization force is always smaller than the stall force in the absence of dynamic instability. Results from mean field theory remain valid, as long as the OPDF is sharply peaked. With increasing stiffness k of the elastic barrier, the average MT length approach results from confinement between rigid walls.

Within this mean field approach, we can also describe the dynamics of the average force, see Figs. 4.12. This might be useful in modeling dilution experiments, where the response to sudden changes in the on-rate is probed. For this type of experiment, we estimate typical polymerization force relaxation times. After dilution we find an exponential decaying return dynamics to the new steady state with a characteristic timescale τ_{d}, governed by growth parameters and the stiffness of the elastic barrier.

We show that our findings are robust against changes of the catastrophe model (Figs. 4.14) as long as the catastrophe rate increases exponentially and the growth velocity decreases exponentially above a characteristic force. For vanishing and non-vanishing rescue rate the catastrophe models by Flyvbjerg *et al.* and Janson *et al.* yield similar results. With the linear catastrophe model, results could only be reproduced for non-vanishing rescue rate (Figs. 4.16). For zero rescue rate, the dynamical mean field theory does not provide reasonable results, due to the missing exponentially increase of the catastrophe rate above the characteristic force.

Finally we show that results are also robust against variations of the relation between force and polymerization velocity in the growing phase (Figs. 4.17), which are obtained by introducing a load distribution factor.

Chapter 6

Microtubule ensembles [1]

In this section we present the model for MT ensemble dynamics. We focus on the growth against an elastic obstacle (see Sec. 4.3), introduce force sharing between simultaneously pushing MTs and extend the basic notation.

6.1 Model for microtubule ensemble dynamics

We consider an ensemble of N parallel MTs, directed along the x-direction. The ensemble is growing in a positive x-direction and pushing against an elastic barrier, as shown in Fig. 6.1. Each single MT is modelled as described in Chap. 2. The cooperative dynamics is governed by the number $n_+ \leq N$ of leading MTs.

The elastic barrier is modelled as a spring with equilibrium position x_0 and a spring constant k. Barrier displacement by the n_+ leading MTs with their tips positioned at $x > x_0$ causes a force $F = F(x) = k(x - x_0)$ resisting further growth; for $x < x_0$ there is a force-free region (see Sec. 4.3). We assume that the force F is equally shared between all n_+ leading MTs such that each leading MT is subject to a force F/n_+. Force-sharing is the only coupling between the MTs. In the presence of rescue events, i.e., for nonzero rescue rate, we force MTs shrinking to $x = 0$ to undergo rescue. This corresponds to a reflecting boundary condition at $x = 0$.

Under a shared force F/n_+, the growth velocity of a MT reduces to

$$v_+(F/n_+) = d\left(\omega_{\text{on}} e^{-F/n_+ F_0} - \omega_{\text{off}}\right) \tag{6.1}$$

with the characteristic force $F_0 = k_{\text{B}}T/d$ [see eq. (2.11)]. In the following we change the notation compared to Sec. 2.2. From now on we use F/F_0 instead of η to describe the force acting on a single MT. Although this is just a change of name, this notation simplifies the calculation of scaling relationships (see Secs. 8.2.3 and 8.2.5).

[1] Parts of the text have been published in reference [54] and are ©2012 American Physical Society. http://publish.aps.org/copyrightFAQ.html

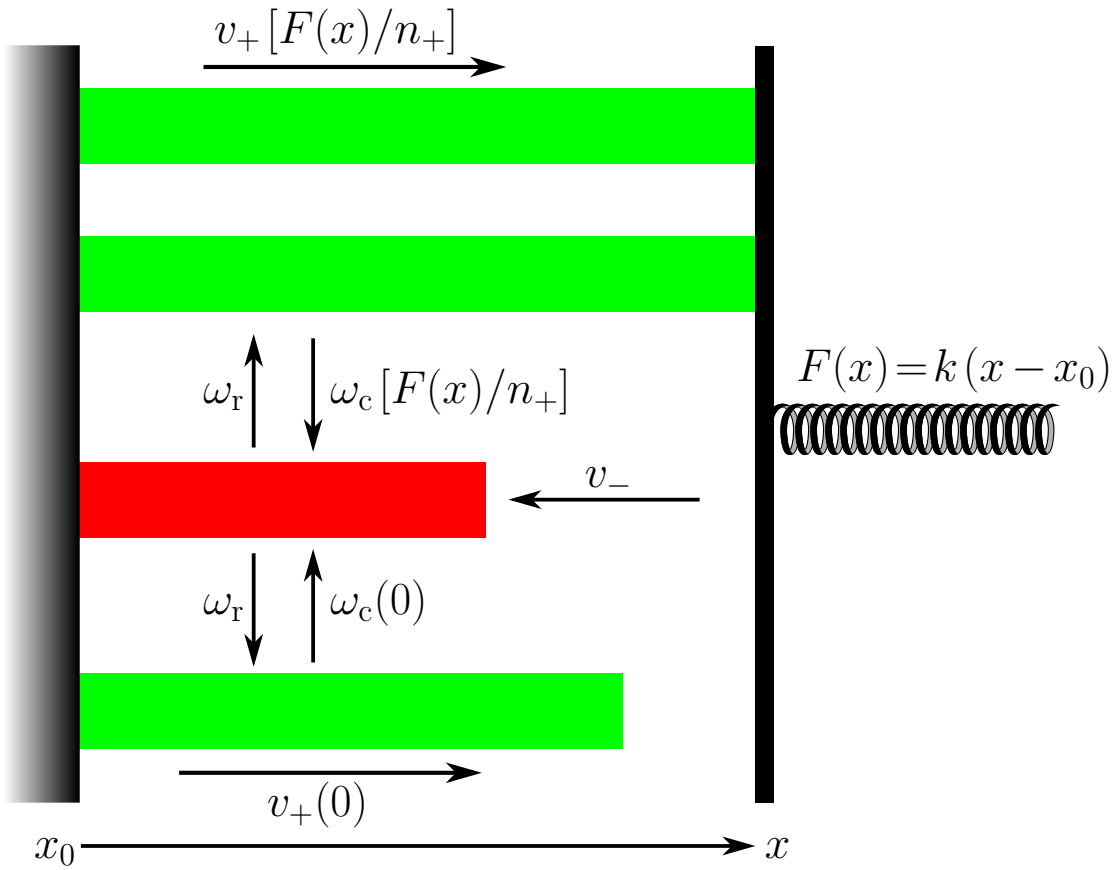

Figure 6.1: Schematic representation of an ensemble with $N = 4$ MTs growing against an elastic obstacle with spring constant k. From top to bottom: $n_+ = 2$ simultaneously pushing MTs (green) with velocity $v_+\,[F(x)/n_+]$ under a shared force $F(x)/n_+$. MT in a state of shrinkage (red) with velocity v_-. MT growing (green) under zero force with velocity $v_+(0)$.

The force-dependent growth velocity also gives rise to a catastrophe rate $\omega_c = \omega_c[v_+(F/n_+)]$ increasing with force. All non-leading MTs grow with the higher zero force velocity $v_+(0) > v_+(F/n_+)$ in their growing state and switch to the state of shrinkage with the zero force catastrophe rate $\omega_c(0) \ll \omega_c(F/n_+)$. Therefore, non-leading MTs which grow force free and fast, "catch up" leading MTs, which grow under force with reduced velocity. This mechanism supports a state of collective growth, where a relatively large number n_+ of MTs are pushing cooperatively. We assume that the shrinking velocity v_- is independent of force.

This model for the dynamics of the MT ensemble is very similar to the model underlying the simulations in Ref. [53]. In particular, we use the same rules for the coupling between MTs by the load force. The most important difference is that we include rescue events in the single MT dynamics, which have not been considered in Ref. [53], and, in addition, we do not employ an artificially increased catastrophe rate (see Sec. 1.4).

Chapter 7

Simulation of microtubule ensembles [1]

In this chapter we present the simulation model for microtubule ensemble dynamics. The single MT simulation model (see Chap. 3) is extended to an ensemble of N MTs, parallelly growing against an elastic obstacle (see Chap. 6). As in Chap. 3, we specify simulation parameters, parameter ranges and characteristic observables.

7.1 Microtubule ensemble simulation model

In the simulation we solve the Langevin-like equations of motion for the length $x_i(t)\,(i = 1,\ldots,N)$ of each single MT within the ensemble. There are N equations of motions, coupled via force-sharing of the n_+ leading MTs. At $t = 0$ all MTs have zero length $x_i(0) = 0$ and are in a state of growth, such that $n_+ = N$. Each single MT is simulated as described in Chap. 3.

In each time step, we have to determine the number n_+ of the leading force-sharing MTs. This is done by regarding all growing MTs within a distance $v_+(F/n_+)\Delta t$ of the leading MTs as leading for the next time step.

In a growing state and under the shared force F/n_+ the velocity of growth $v_+(F/n_+)$, for the n_+ leading MTs, is calculated from eq. (6.1). All non-leading MTs grow with the higher zero force velocity $v_+(0)$ given by eq. (2.9). In a state of shrinkage each MT shrinks with average velocity $v_- = 3\times10^{-7}\,\mathrm{m/s}$ (see Table A.1).

The catastrophe rate ω_c is calculated from eq. (2.35) in the Flyvbjerg model and from eq. (2.38) in the Janson model.

The number N of MTs within the ensemble is varied in the range of $N = 2,\ldots,20$ and we simulate $N_\mathrm{ens} = 100 - 1000$ independent MT ensembles. Compared to simulations of single MTs (see Chap. 3), the number of independent MT ensembles is decreased to

[1] Parts of the text have been published in reference [54] and are ©2012 American Physical Society. http://publish.aps.org/copyrightFAQ.html

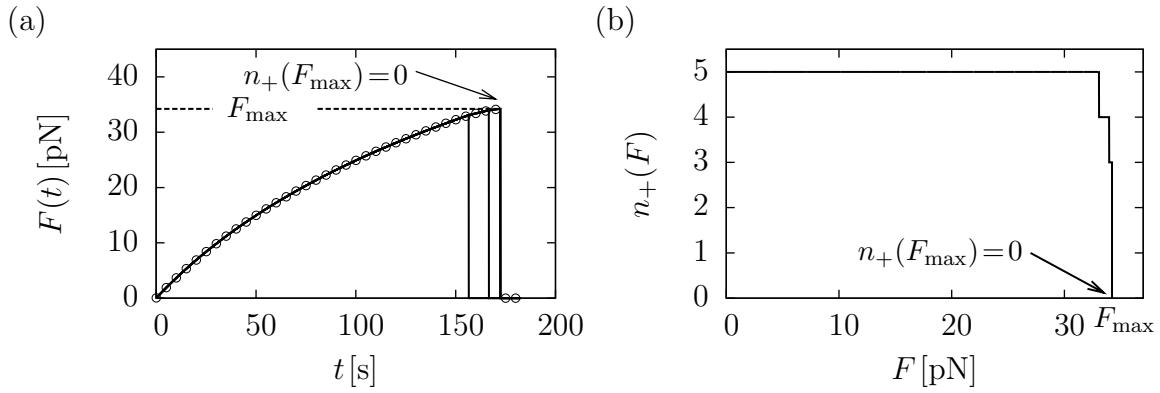

Figure 7.1: Sample trajectories for $N = 5$ MTs for vanishing rescue rate ω_r. We set $x_0 = 0$, $\omega_{on} = 70\,s^{-1}$ and $k = 10^{-5}\,N/m$. (a): Polymerization force $F(t)$ as a function of time t. Dots represent the position $x(t)$ of the elastic obstacle, which is equivalent to the position of the n_+ leading MTs. Solid lines are trajectories of single MTs. At the maximal polymerization force F_{max} ($t \approx 175\,s$) all MTs are in a state of shrinkage and the dynamics stops due to missing rescue events. (b): $n_+(F)$ as a function of the polymerization force F. The maximal polymerization force is obtained from the condition $n_+(F_{max}) = 0$ ($F \approx 34\,pN$).

reduce simulation time. This does not lead to significant measurement inaccuracies in the numerical results.

As outlined in Chap. 3 we vary ω_{on} in the range $\omega_{on} = (30 - 100)\,s^{-1}$ and ω_r in the range $\omega_r = (0.03 - 0.2)\,s^{-1}$.

The most important observables are the position of the elastic obstacle $x(t)$, which is equivalent to the position of the n_+ leading MTs, and corresponds to a force $F(t) = (x(t) - x_0)$, and the number n_+ of simultaneously pushing MTs between the resisting force is shared equally.

In order to determine the characteristic observables for the dynamics of MT ensembles, we have to anticipate numerical results from Secs. 8.1 and 8.2. We present two types of stochastic trajectories and clarify how observables are determined from numerical data. Both types of stochastic trajectories are described in detail later (see Sec. 8.1 for $\omega_r = 0$ and Sec. 8.2 for $\omega_r > 0$).

7.1.1 Vanishing rescue rate

For vanishing rescue rate $\omega_r = 0$ we set $x_0 = 0$. Figure 7.1(a) shows the stochastic time evolution of $N = 5$ MTs. The MT bundle polymerizes against the elastic obstacle until the maximal polymerization force F_{max} is reached. At F_{max} all MTs within ensemble have switched into a state of shrinkage, such that $n_+ = 0$ [see Fig. 7.1(b)] and the dynamics stops due to missing rescue events. The maximal polymerization force F_{max} is therefore determined by the condition $n_+(F_{max}) = 0$. Since F_{max} is a stochastic quantity we perform ensemble-averages, via eq. (3.3), over N_{ens} independent simulation runs.

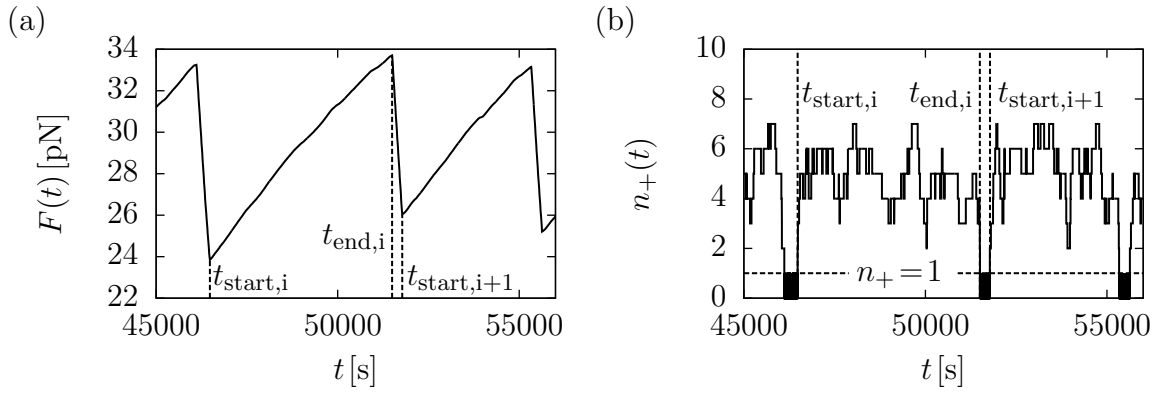

Figure 7.2: (a) Polymerization force $F(t)$ as a function of time t for $N = 10$ MTs and non-zero rescue rate $\omega_\mathrm{r} = 0.05\,\mathrm{s}^{-1}$. We set $x_0 = 10^{-5}\,\mathrm{m}$, $\omega_\mathrm{on} = 70\,\mathrm{s}^{-1}$ and $k = 10^{-7}\,\mathrm{N/m}$. Vertical dashed lines mark the begin ($t \approx 47000\,\mathrm{s}$) and the end ($t \approx 52000\,\mathrm{s}$) of a phase of collective growth. (b) The number of simultaneously pushing MTs $n_+(t)$ as a function of time, corresponding to the polymerization force $F(t)$ shown in Fig. 7.2(a). Vertical dashed lines mark the begin ($t \approx 47000\,\mathrm{s}$) and the end ($t \approx 52000\,\mathrm{s}$) of a phase of collective growth. Horizontal dashed line represents $n_+ = 1$.

7.1.2 Non-zero rescue rate

For a non-vanishing rescue rate $\omega_\mathrm{r} > 0$ we set $x_0 = 10^{-5}\,\mathrm{m}$. Figure 7.2(a) shows the stochastic time evolution of $N = 10$ MTs. In contrast to Sec. 7.1.1 rescue events lead to a steady state of the cooperative dynamics. In the steady state the MT ensemble alternates between phases of collective growth and phases of collective shrinkage [see Fig. 7.2(a)]. This gives rise to oscillations in the polymerization force $F(t) = (x(t) - x_0)$ around its mean value $F_\mathrm{s,N}$. First we perform a time-dependent ensemble average over N_ens independent simulations runs via eq. (3.3). In the steady state, which is determined by visual inspection of sample trajectories, we run an additional time-average via eq. (3.3) and obtain the ensemble averaged polymerization force $F_\mathrm{s,N}$ in the steady state.

From numerical data we can also determine the average length of phases of collective growth and shrinkage. Phases of collective growth are characterised by a stable number of simultaneously pushing MTs with $n_+ > 1$. In a collective catastrophe all MT switch into a state of shrinkage and n_+ drops down to zero. The system enters a state of collective shrinkage with $n_+ = 0 - 1$.

We therefore define the begin t_start of a phase of collective growth by $n_+(t_\mathrm{start}) > 1$ and the end t_end by $n_+(t) = 0$ [see Fig. 7.2(b)]. The length of a phase of collective growth is than given by $T_+ = t_\mathrm{end} - t_\mathrm{start}$. Since the ensemble alternates between collective growth and shrinkage, the length of a phase of collective shrinkage is calculated from the time difference of two successive periods of collective growth and is given by $T_- = t_{\mathrm{start},i+1} - t_{\mathrm{end},i}$. Here i denotes the sequence of phases of collective growth (see Fig. 7.2).

In phases of collective shrinkage and for high forces $F(t)$, n_+ is subject to considerable fluctuations. Especially for large values of ω_on and ω_r, the begin of a phase of collective

growth can not be captured by the condition $n_+(t_{\text{start}}) > 1$ since even fluctuations leading to $n_+ = 2-3$ do not initiate a phase of collective growth. The condition $n_+(t_{\text{start}}) > 1$ is adjusted to $n_+(t_{\text{start}}) > 2-3$ depending on the parameter set. This is done by visual inspection of sample trajectories. However, for most parameter values $n_+ > 1$ is sufficient to indicate the begin of a phase of collective growth.
With t_{start} and t_{end} we can now determine the mean number $\overline{n_+}$ of simultaneously pushing MTs averaged over a phase of collective growth by

$$\overline{n_+} = T_+^{-1} \sum_{t_{\text{start}}}^{t_{\text{end}}} n_+(t). \tag{7.1}$$

Since $\overline{n_+}$ is still a stochastic quantity we also perform an ensemble average of typically 1000-10000 successive phases of growth and obtain the time- and ensemble averaged number $\langle \overline{n_+} \rangle$ of pushing MTs in the steady state.

Chapter 8

Microtubule ensemble dynamics [1]

In this chapter we present the results for MT ensemble dynamics for zero and non-zero rescue rate.

Sec. 8.1 deals with MT bundles polymerizing against an elastic force in the absence of rescue events. This scenario is close to the optical trap experiments by Laan *et al.*[53] (see Sec. 1.4). We develop a dynamical mean field theory and quantify the cooperative dynamics of MT in terms of the mean force $\langle F \rangle$ and the mean number of simultaneously pushing MTs $\langle n_+ \rangle$. The maximal polymerization force $F_{\max}$ is calculated as a function of the number of MTs N, the stiffness of the barrier k, and the tubulin on-rate ω_{on}. In addition we show that our results are robust with respect to changes in the catastrophe model and are in good agreement with available experimental data for small N or a stiff elastic barrier [53].

Sec. 8.2 deals with MT bundles polymerizing against an elastic force in the presence of rescue events. We present results from full stochastic simulations (Sec. 8.2.1) and discuss the cooperative dynamics, in particular collective catastrophes and collective rescues.

In Sec. 8.2.2 the dynamic mean-field theory is extended by rescue events of single MTs. The oscillatory mean-field dynamics is discussed, based on the nullclines of the mean-field equations (Sec. 8.2.3). We calculate the critical mean-field force F_{c}, the average polymerization force $F_{s,N}$ and the average number of pushing MTs as functions of the system parameters. Additionally we show that our results are robust with respect to changes in the catastrophe model (Sec. 8.2.4). In Sec. 8.2.5 fluctuations in the number of pushing MTs are included into the dynamical mean-field theory. In Sec. 8.2.6 we develop a semi-stochastic approach to the stochastic dynamics of the leading MTs and investigate the validity and limits of the dynamical mean-field theory.

[1] Parts of the text have been published in reference [54] and are ©2012 American Physical Society. http://publish.aps.org/copyrightFAQ.html

8.1 Microtubule bundle dynamics at zero rescue rate

We start the analysis with the case of zero rescue rate because this case is conceptually simpler to understand as rescue events are absent, and there are only collective catastrophes to be discussed. Furthermore, this case is particularly important because experimental data are available: In recent experiments, Laan *et al.* [53] showed that MT ensembles exhibit phases of collective growth followed by collective catastrophes, where all leading MT nearly simultaneously undergo a catastrophe. The experiments were performed on short time scales such that no rescue events occur. It was also observed that the maximal polymerization force before catastrophes grows linearly in N. We quantify these features based on a dynamical mean-field theory.

In an ensemble of N MTs the dynamic instability of individual MTs leads to stochastic fluctuations in the number n_+ of leading MTs. The force F changes by filament growth according to $\dot{F} = k\dot{x}$ with $\dot{x} = v_+(F/n_+)$ if the ensemble grows ($n_+ \geq 1$) and $\dot{x} = -v_-$ if all MTs shrink ($n_+ = 0$). In a state of collective growth, a stable mean number of MTs are pushing cooperatively, while the force F is increasing by growth against the elastic barrier. If the number n_+ of pushing MTs is reduced by an individual catastrophe, the force on the remaining $n_+ - 1$ leading MTs increases and, thus, their catastrophe rate $\omega_c(F/n_+)$ increases. A cascade of individual catastrophes, a *collective catastrophe*, can be initiated until a state $n_+ = 0$ is reached with all MTs shrinking. This is the final absorbing state of the system in the absence of rescue events.

The stochastic dynamics of n_+ in a growing phase in the absence of rescue events is described by a one-step master equation with backward rate $r_{n_+} = n_+\omega_c(F/n_+)$ for decreasing n_+ by one, which derives from the catastrophe rate of individual MTs under force sharing. In a mean-field approach, we replace the stochastic variables F and n_+ by their time-dependent mean values $\langle F\rangle$ and $\langle n_+\rangle$, averaged over many realizations of the stochastic n_+- and F-dynamics, and neglect all higher-order correlations, e.g. set $\langle F/n_+\rangle = \langle F\rangle/\langle n_+\rangle$. In the growing phase, we then obtain two coupled mean-field equations,

$$d\langle n_+\rangle/dt = -\langle n_+\rangle\omega_c\left(\langle F\rangle/\langle n_+\rangle\right), \tag{8.1}$$

$$d\langle F\rangle/dt = kv_+\left(\langle F\rangle/\langle n_+\rangle\right). \tag{8.2}$$

In the mean-field approximation we can calculate the maximal polymerization force $F_{\max}$, again averaged over many realizations, that is reached during the mean first-passage time from $n_+ = N$ to $n_+ = 0$ by solving

$$\frac{d\langle F\rangle}{d\langle n_+\rangle} = \frac{d\langle F\rangle/dt}{d\langle n_+\rangle/dt} = -\frac{kv_+\left(\langle F\rangle/\langle n_+\rangle\right)}{\langle n_+\rangle\omega_c\left(\langle F\rangle/\langle n_+\rangle\right)}. \tag{8.3}$$

with initial conditions $\langle F\rangle = 0$ for $\langle n_+\rangle = N$ in order to find $\langle F\rangle = F_{\max}$ at $\langle n_+\rangle \approx 0$. Above the characteristic force F_0, the ratio $v_+(F)/\omega_c(F)$ decays exponentially because $v_+(F)$ decreases exponentially and $\omega_c[v_+(F)]$ increases exponentially. Therefore, we can solve in two steps: (i) As long as the shared force is small compared to F_0, $\langle F\rangle/\langle n_+\rangle \ll F_0$, we neglect the force and find $\langle F\rangle \approx kv_+(0)/\omega_c(0)\ln(N/\langle n_+\rangle)$. (ii) For $\langle F\rangle/\langle n_+\rangle \gg F_0$, on the other hand, the catastrophe frequency increases exponentially, and we can assume that $d\langle F\rangle/d\langle n_+\rangle \approx 0$ and $\langle F\rangle$ remains constant.

The boundary between regimes (i) and (ii) is determined by the condition $\langle F\rangle/\langle n_+\rangle = F_0$: Regime (i) applies for $\langle n_+\rangle > n_0$ with $n_0 = \alpha W(N/\alpha)$, where $W(x)$ is the Lambert W-function, which is the solution of $x = We^W$ (for $W \geq -1$). The parameter

$$\alpha \equiv kv_+(0)/\omega_c(0)F_0 \tag{8.4}$$

is a dimensionless measure for the stiffness of the elastic barrier. Because $\langle F\rangle$ remains constant for $\langle n_+\rangle < n_0$, the resulting maximal polymerization force is given by

$$F_{\max} = n_0 F_0 = F_0 \alpha W(N/\alpha), \tag{8.5}$$

with a logarithmic asymptotic $F_{\max} \approx F_0\alpha\ln(N/\alpha)$ for large $N \gg \alpha$ [85] or a soft barrier and a quasilinear behavior $F_{\max} \approx F_0 N(1 - N/\alpha)$, which is *independent* of α to leading order, for small $N \ll \alpha$ or a stiff barrier. The mean-field result from eq. (8.5) agrees with numerical solutions of the mean field dynamics as given by eqs. (8.1) and (8.2) and full stochastic simulations both for soft and stiff barriers, as can be seen in Fig. 8.1.

The parameter α can also be interpreted as a measure for the relative speed of the initial $\langle n_+\rangle$ and $\langle F\rangle$ dynamics according to the mean-field equations (8.1) and (8.2), which allows us to give simple arguments for the maximal polymerization force $F_{\max}$: For $\alpha \ll N$ (the case of a soft barrier), the $\langle n_+\rangle$ dynamics is fast compared to the $\langle F\rangle$ dynamics. Therefore, $\langle n_+\rangle$ decays approximately force free in a time $t_c \sim 1/\omega_c(0)\ln N$ from $\langle n_+\rangle = N$ to $\langle n_+\rangle = 1$. During this time, the force reaches a value $F_{\max} \sim kv_+(0)t_c \sim F_0\alpha\ln N$. For $\alpha \gg N$ (the case of a stiff barrier), the $\langle n_+\rangle$-dynamics is initially slow compared to the $\langle F\rangle$-dynamics and $\langle n_+\rangle \approx N$ until the characteristic force F_0 per MT is reached and the catastrophe rate increases exponentially. Up to this point, essentially N MTs share the force such that F increases up to $F_{\max} \sim F_0 N$ until catastrophes set in. This takes a time $t_c \sim NF_0/kv_+(0)$ and $\Delta\langle n_+\rangle \sim \langle\dot{n}_+\rangle t_c \sim N/\alpha \ll 1$ is indeed small such that the assumption $\langle n_+\rangle \approx N$ is consistent.

In the experiments in Ref. [53], the spring stiffness was $k \simeq 10^{-5}$ N/m, which gives $\alpha \simeq 27$ such that these experiments were performed in the quasilinear regime of a stiff barrier, where we predict $F_{\max} \approx F_0 N$ for all experimentally accessible N (see the upper lines in Fig. 8.1). This linear increase is in agreement with the experimental results but the ratio $F_{\max}/N$ is only of the order of 3 pN experimentally, while $F_0 \simeq 7$ pN. This hints at a

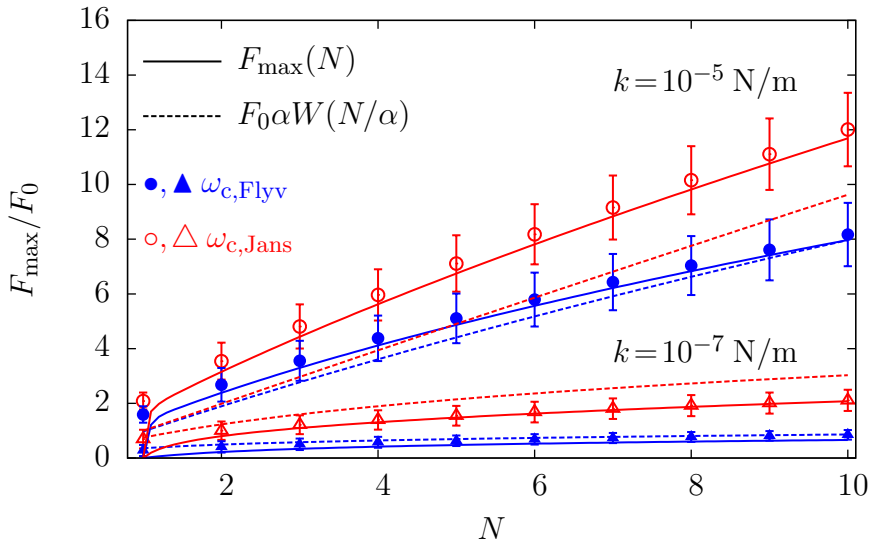

Figure 8.1: $F_{\max}/F_0$ as a function of N for zero rescue rate, $\omega_{on} = 70\,s^{-1}$, and $k = 10^{-7}$ N/m ($\alpha \simeq 0.27$, soft barrier) and $k = 10^{-5}$ N/m ($\alpha \simeq 27$, stiff barrier). We compare results for the catastrophe models of Flyvbjerg (blue, solid symbols) and Janson (red, open symbols). Data points are simulation results; error bars represent the standard deviation of the stochastic quantity $F_{\max}/F_0$. Solid lines are numerical solution of the mean field dynamics [see eq. (8.1) and eq. (8.2)]. Dashed lines are analytical estimates according to eq. (8.5).

lower value for F_0 in the force-polymerization velocity relation for MTs; experimentally, a value $F_0 \simeq 2$ pN has been measured in Ref. [86], which is indeed compatible with the experimental results of Ref. [53].

In Fig. 8.1, we compare mean-field theory and simulation results for the Flyvbjerg and the Janson catastrophe model for both soft and stiff barriers. For both models, we find agreement between mean-field theory and simulations and, moreover, both models give comparable values for generated forces. This demonstrates that results for the cooperative force generation at zero rescue rate are robust with respect to details of the single-MT catastrophe model. The essential feature entering the mean-field theory is the exponential increase of the catastrophe frequency with force above the characteristic force F_0.

8.2 Microtubule bundle dynamics at non-zero rescue rate

We now consider force generation in the presence of rescue events. Rescue events were not included in the simulation model in Ref. [53]. Also experiments in Ref. [53] were performed on short time scales such that no rescue events occurred. However, rescue events are an essential part of MT dynamics, and their influence on force generation and MT dynamics needs to be addressed.

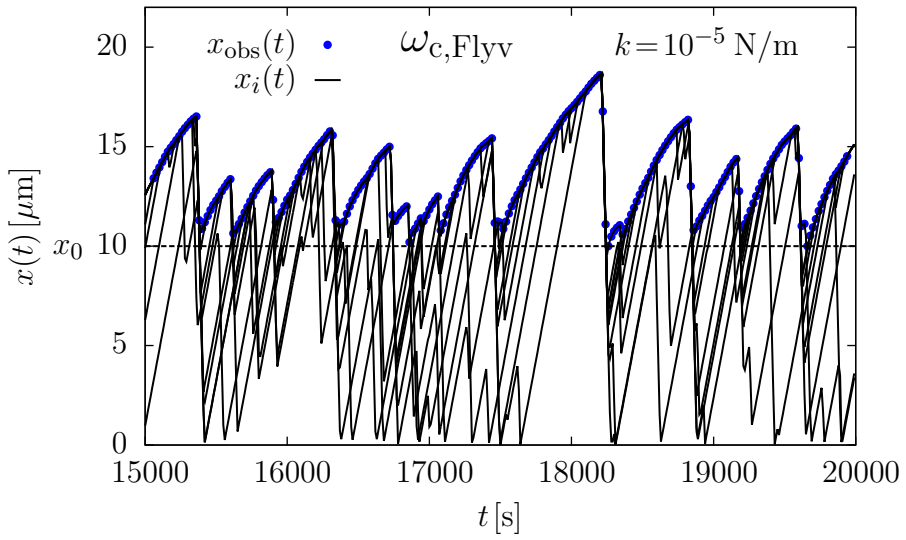

Figure 8.2: Typical simulation trajectories for $N = 10$ MTs, $\omega_{\mathrm{on}} = 70\,\mathrm{s}^{-1}$, $\omega_{\mathrm{r}} = 0.05\,\mathrm{s}^{-1}$ and a stiff obstacle with $k = 10^{-5}$ N/m. We use the Flyvbjerg catastrophe model with $F_0 \simeq 7\,\mathrm{pN}$. Dashed line represents $x_0 = 10\,\mu\mathrm{m}$. Solid lines: Positions of all MTs as a function of time t. Blue, filled dots: The obstacle position $x_{\mathrm{obs}}(t)$ is the position of the leading MTs (only every 1000th data point shown). In the force free region $x < x_0$, MTs decouple.

In the presence of rescue events, the dynamics will not change considerably for $N \ll \alpha$, i.e., for a stiff barrier because this limit corresponds to a *slow* $\langle n_+ \rangle$-dynamics, which cannot benefit from additional rescue events. Moreover, because the $\langle F \rangle$-dynamics is fast, rescues will not happen before the force-free region $x < x_0$ is reached, where MTs decouple (see Fig. 8.2).

Therefore, we focus on the influence of rescue events for $N \gg \alpha$ or a soft barrier corresponding to a *fast* $\langle n_+ \rangle$ dynamics.

We begin our discussion with simulation results and discus characteristic steady-state trajectories.

8.2.1 Simulation results

In the regime of a soft barrier, the collective dynamics becomes strongly modified. Apart from collective catastrophes also collective rescue events occur: After a collective catastrophe the system is in a state $n_+ = 0$ with all MTs shrinking. Individual rescue events lead to $n_+ = 1$, but a single MT bearing the whole force undergoes an immediate catastrophe again with high probability. Therefore, a cascade of rescue events a *collective rescue* is necessary to increase n_+ back to a number sufficient to maintain stable collective growth. Snapshots from stochastic simulations, corresponding to characteristic phases of collective growth are shown in Fig. 8.5.

Alternating collective catastrophes and collective rescue events give rise to oscillations in

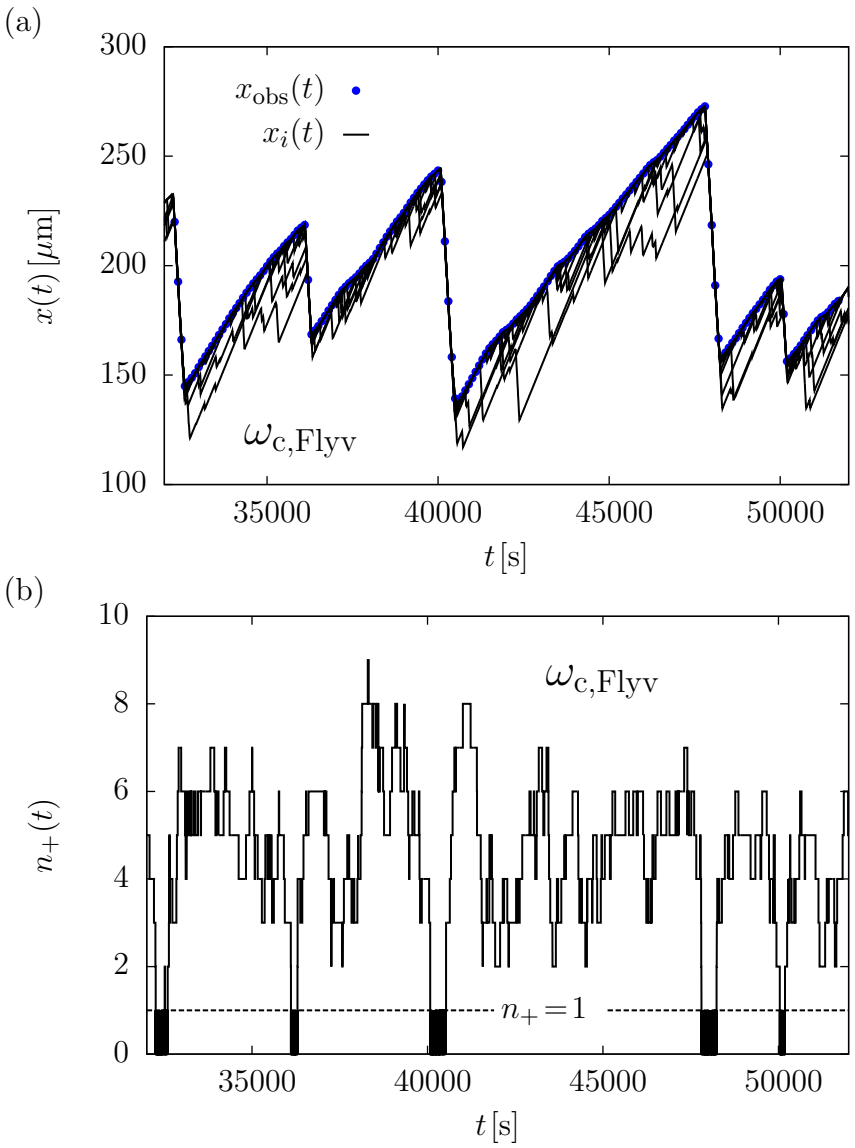

Figure 8.3: Typical simulation trajectories for $N = 10$ MTs, $\omega_{\rm on} = 70\,{\rm s}^{-1}$, $\omega_{\rm r} = 0.05\,{\rm s}^{-1}$ and for the Flyvbjerg catastrophe model with $F_0 \simeq 7\,{\rm pN}$. (a): Positions of all MTs as a function of time t (solid lines); the obstacle position $x_{\rm obs}(t)$ (blue, filled dots) is the position of the leading MT (only every 1000th data point shown). (b): The number n_+ of leading MTs as a function of time t. Collective catastrophes and collective rescue events can clearly be recognized: In a collective catastrophe n_+ drops to $n_+ = 1$ and $x(t)$ of the leading MTs starts to shrink; after a collective rescue n_+ starts to increase again to values $n_+ > 1$, and $x(t)$ of the leading MTs start to grow.

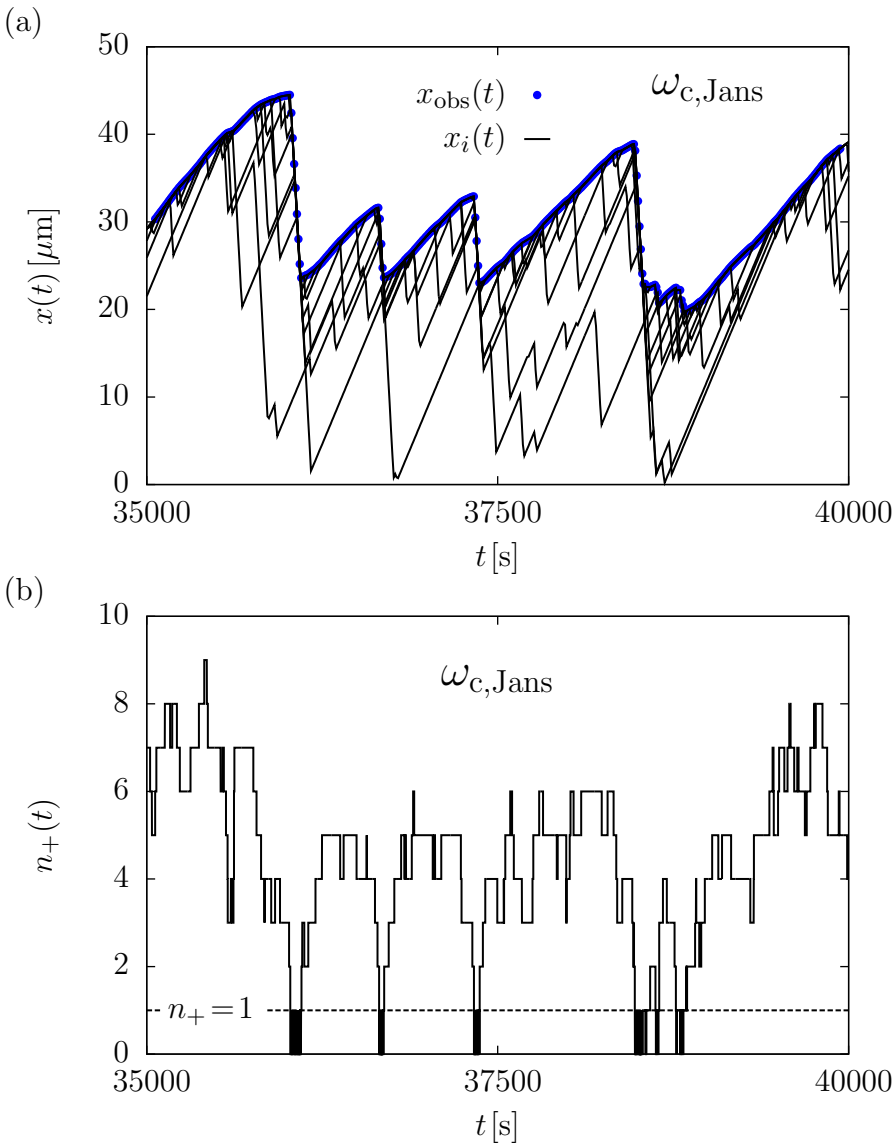

Figure 8.4: Typical simulation trajectories for $N = 10$ MTs, $\omega_{\mathrm{on}} = 70\,\mathrm{s}^{-1}$, $\omega_{\mathrm{r}} = 0.05\,\mathrm{s}^{-1}$ and for the Janson catastrophe model with $F_0 \simeq 0.8\,\mathrm{pN}$. (a): Positions of all MTs as a function of time t (solid lines); the obstacle position $x_{\mathrm{obs}}(t)$ (blue, filled dots) is the position of the leading MT (only every 100th data point shown). (b): The number n_+ of leading MTs as a function of time t. Collective catastrophes and collective rescue events can clearly be recognized: In a collective catastrophe n_+ drops to $n_+ = 1$ and $x(t)$ of the leading MTs starts to shrink; after a collective rescue n_+ starts to increase again to values $n_+ > 1$, and $x(t)$ of the leading MTs start to grow.

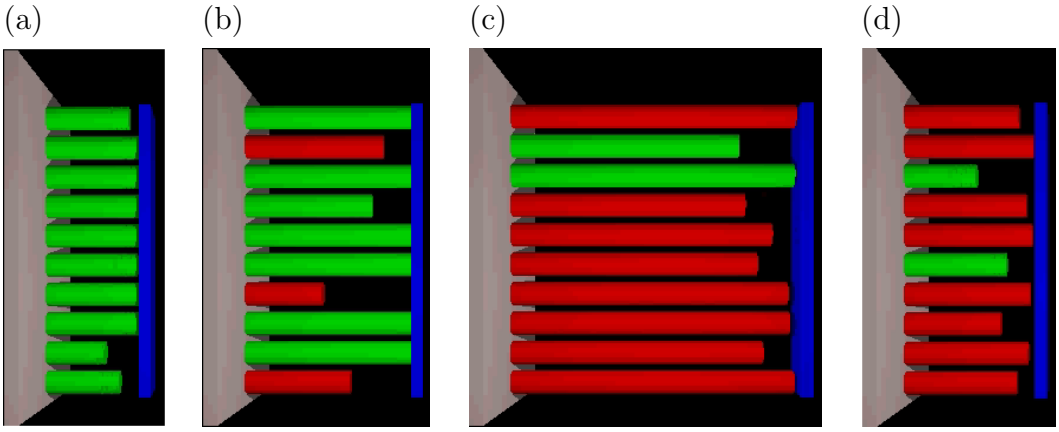

Figure 8.5: Snapshots from stochastic simulations for $N = 10$ MTs, $\omega_{\text{on}} = 70\,\text{s}^{-1}$, $\omega_{\text{r}} = 0.05\,\text{s}^{-1}$ and $k = 10^{-7}$ N/m. MT configurations corresponding to characteristic phases of the collective dynamics for growth against an elastic obstacle (blue): (a) MT ensemble shortly after an collective rescue. All MTs are in a state of growth (green), with $n_+ = 7$ simultaneously pushing MTs and three MTs growing under no force. (b) MT ensemble in a state of collective growth with $n_+ = 6$ simultaneously pushing MTs, three MTs shrinking (red) and one MT growing under no force. (c) MT ensemble shortly after an collective catastrophe, with nine MTs shrinking and, caused by a stochastic rescue event, $n_+ = 1$ pushing MTs. (d) MT ensemble in a state of collective shrinkage, with eight MTs shrinking and two MTs growing under no force.

the steady-state polymerization force or, equivalently, the position x_{obs} of the obstacle. Such oscillations with alternating collective catastrophes and collective rescue events can clearly be seen in the stochastic simulation trajectories for the positions x of the MTs [see Figs. 8.3(a) and 8.4(a)] and the number n_+ of leading MTs [see Figs. 8.3(b) and 8.4(b)] as a function of time t. The simulation trajectories also show that this phenomenon is robust with respect to the catastrophe model and can be observed both for the Flyvbjerg and the Janson catastrophe models, which are shown in Figs. 8.3 and 8.4 respectively, and exhibit qualitatively very similar behavior. Similar oscillations have been observed in the simulations in Ref. [53] in the presence of MT renucleation instead of MT rescue and for a constant force.

Here we want to stress that there are major differences between oscillations presented here and observed by Laan *et al.* Laan *et al.* used a small constant force in their simulations, whereas we use an elastic force, that allows the system to find its steady-state force without external restrictions. We find oscillatory behavior at much larger forces then used by Laan *et al.* Another major difference is renucleation of MTs instead of rescue events of single MTs. From our point of view renucleation and rescue events do not lead to the same type of oscillatory behavior. In the absence of rescue events MTs shrink back to zero length after a catastrophe and restart to grow after a characteristic time, that is the inverse nucleation rate. Since renucleation of single MTs is independent of other nucleation events, single MTs decouple and renucleation does not lead to synchronous MT growth. However, spontaneous renucleation of two or more MTs is possible and

causes a temporary synchronization of MT growth. This synchronization is not based on a cooperative mechanism and is lost on long time scales. In contrast, including rescue events we find stable synchronous MT oscillations on long time scales (see Figs. 8.3 and 8.4). Rescue events and an elastic resisting force enable the system to organize itself into a stable cooperative dynamics, in particular a stable oscillation of phases with simultaneous growth, ended by collective catastrophes, and phases of simultaneous shrinkage, ended by collective rescues.

In the simulations we measure the polymerization force $F_{\mathrm{s,N}} = \overline{\langle F \rangle}$, which is averaged over time and many realizations as a function of MT number N and on-rate ω_{on}. This time-averaged polymerization force is also the stall force of the MT ensemble. The results are shown in Fig. 8.6(a) for the Flyvbjerg catastrophe model and in Fig. 8.6(b) for the Janson catastrophe model. The main finding of the simulations is an approximately *linear* increase of the polymerization force $F_{\mathrm{s,N}}$ with the number N of MTs [see Fig. 8.6(a) and 8.6(b)]. This shows that for large MT ensembles, rescue events give rise to much higher polymerization forces as compared to the logarithmic N dependence derived in the previous section in the absence of rescue events for a soft barrier ($N \gg \alpha$). Simulations also show an approximately linear increase of the polymerization force with the on-rate ω_{on} [see Figs. 8.7(a) and 8.7(b)].

We also show numerical results for the time-averaged pushing fraction $\overline{\nu_+} = \langle \overline{n_+} \rangle / N$ of MTs as a function of the on-rate ω_{on} in Figs. 8.8(a) and 8.8(b). The pushing fraction increases with on-rate, which demonstrates an increasing tendency of MTs to push *synchronously* at higher on-rates, where larger forces are generated.

Simulation results for the Flyvbjerg model and the Janson model show a very similar linear increase for the polymerization force $F_{\mathrm{s,N}}$ with N [see Figs. 8.6(a) and 8.6(b)] and very similar results for the time-averaged pushing fraction $\overline{\nu_+}$ of MTs [see Figs. 8.8(a) and 8.8(b)], which is in accordance with the qualitatively similar simulation trajectories shown in Figs. 8.3 and 8.4 for both catastrophe models. This further supports that our results are robust with respect to the catastrophe model.

The absolute values of typical forces in Figs. 8.6(a), 8.6(b), 8.7(a), and 8.7(b) and, similarly, between typical MT lengths in Figs. 8.3(a) and 8.4(a) differ, however, between the two catastrophe models. The reason is that the basic force scale of the problem is the characteristic force F_0, above which the catastrophe rate increases exponentially, as will be shown below. We have chosen the theoretical value $F_0 = k_{\mathrm{B}}T/d \simeq 7$ pN for the Flyvbjerg model and the much smaller value $F_0 = 0.8$ pN according to Ref. [53] with the Janson model. In units of the characteristic force F_0, typical forces are very similar [see Figs. 8.6(a), 8.6(b), 8.7(a), and 8.7(b) right scale].

Here we want to refer to a closely related biophysical model system: a cluster of molecular bonds. In the following, we illustrate similarities of the dynamics of molecular bonds under a constant force and the cooperative dynamics of a MT ensemble, and point out major

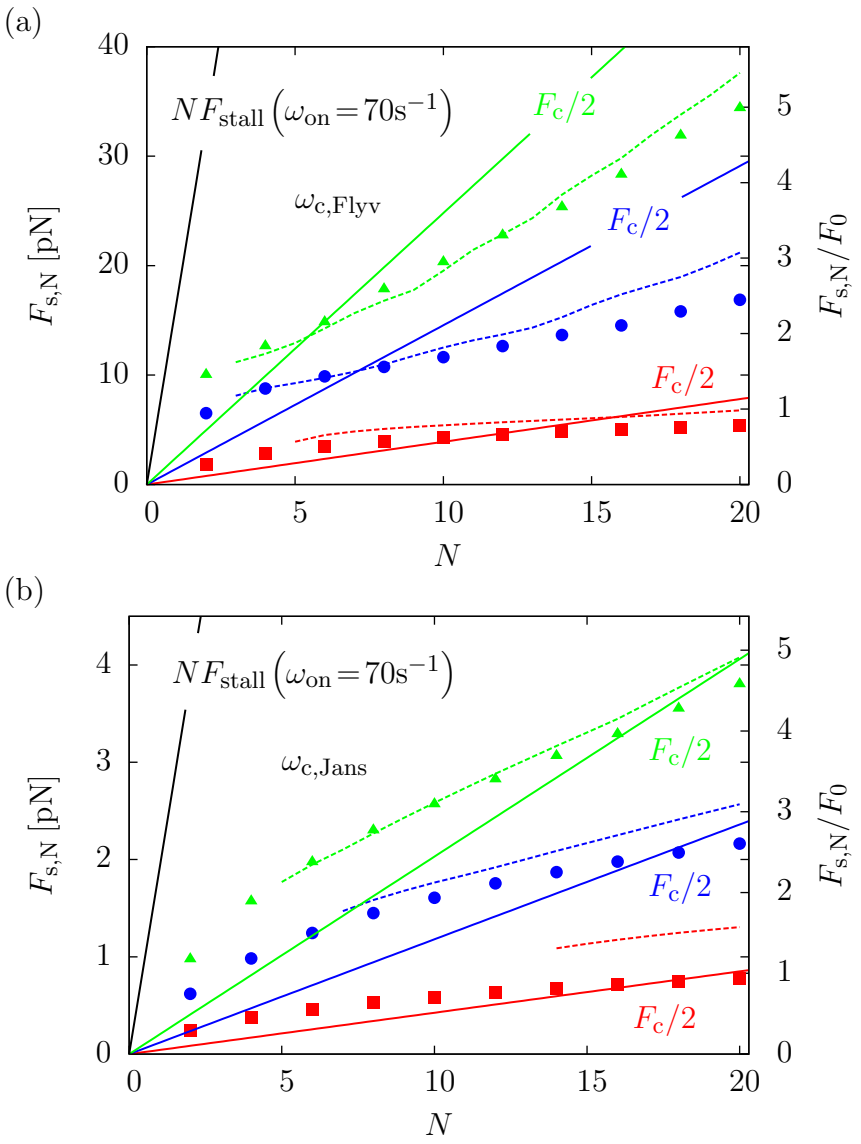

Figure 8.6: Average polymerization force $F_{\mathrm{s,N}}$ as a function of microtubule number N for $\omega_{\mathrm{r}} = 0.05\,\mathrm{s}^{-1}$ and a soft barrier with $k = 10^{-7}$ N/m. Data points: Simulation results for different on-rates $\omega_{\mathrm{on}} = 30\,\mathrm{s}^{-1}$ (■), $50\,\mathrm{s}^{-1}$ (●), and $70\,\mathrm{s}^{-1}$ (▲) Solid lines: Mean field estimate $F_{s,N} = F_c/2$, see eq. (8.22) (neglecting F_{min}). Dashed lines: Numerical mean field solution including stochastic effects. Black solid line: N-fold single-MT stall force $F_{\mathrm{s,N}} = NF_{\mathrm{stall}}$ for $\omega_{\mathrm{on}} = 70\,\mathrm{s}^{-1}$. (a): Simulation and analytical results using the Flyvbjerg catastrophe model with $F_0 \simeq 7$ pN. (b): Simulation and analytical results using the Janson catastrophe model with $F_0 \simeq 0.8$ pN.

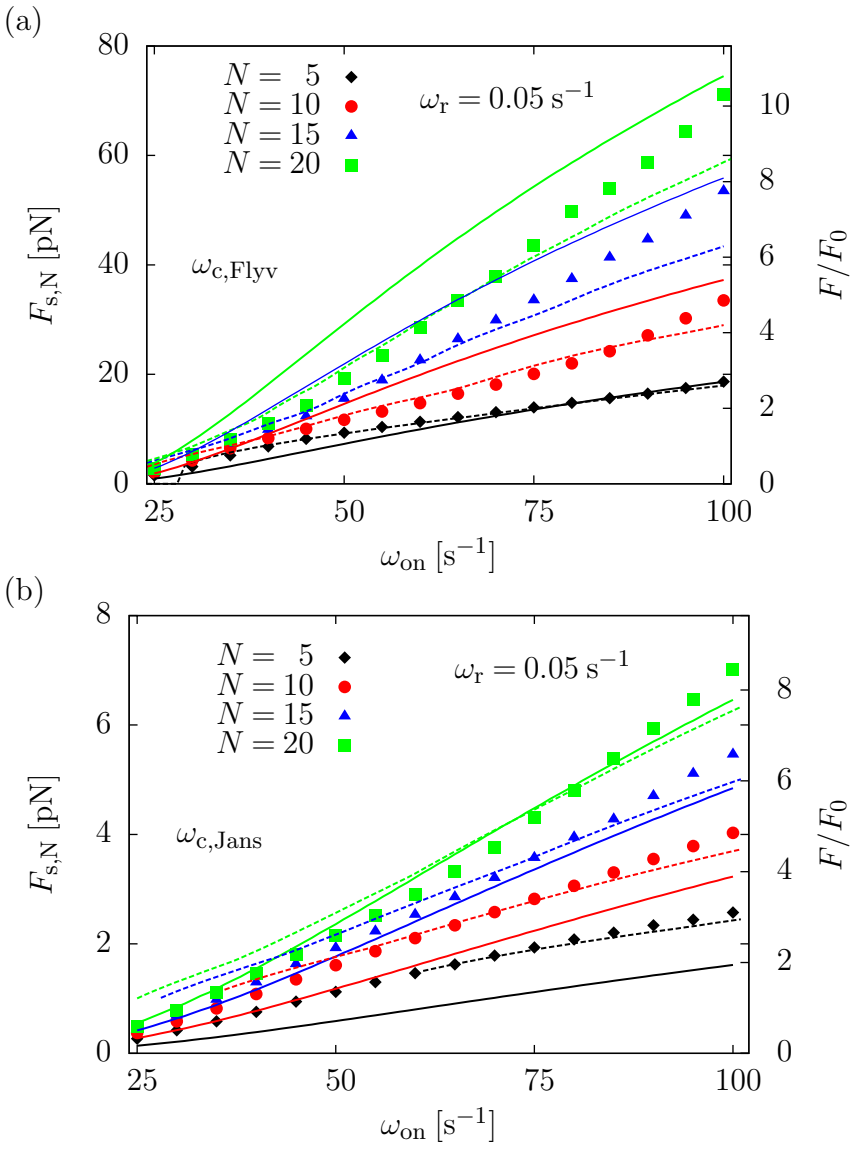

Figure 8.7: Average polymerization force $F_{s,N}$ as a function of the on-rate ω_{on} for $\omega_r = 0.05\ s^{-1}$ and a soft barrier with $k = 10^{-7}$ N/m. Data points: Simulation results for different MT number $N = 5$ (◆), 10 (●), 15 (▲), 20 (■). Solid lines: Mean field estimate $F_{s,N} = F_c/2$, see eq. (8.22) (neglecting F_{min}). Dashed lines: Numerical mean field solution including stochastic effects. (a): Simulation and analytical results using the Flyvbjerg catastrophe model with $F_0 \simeq 7$ pN. (b): Simulation and analytical results using the Janson catastrophe model with $F_0 \simeq 0.8$ pN.

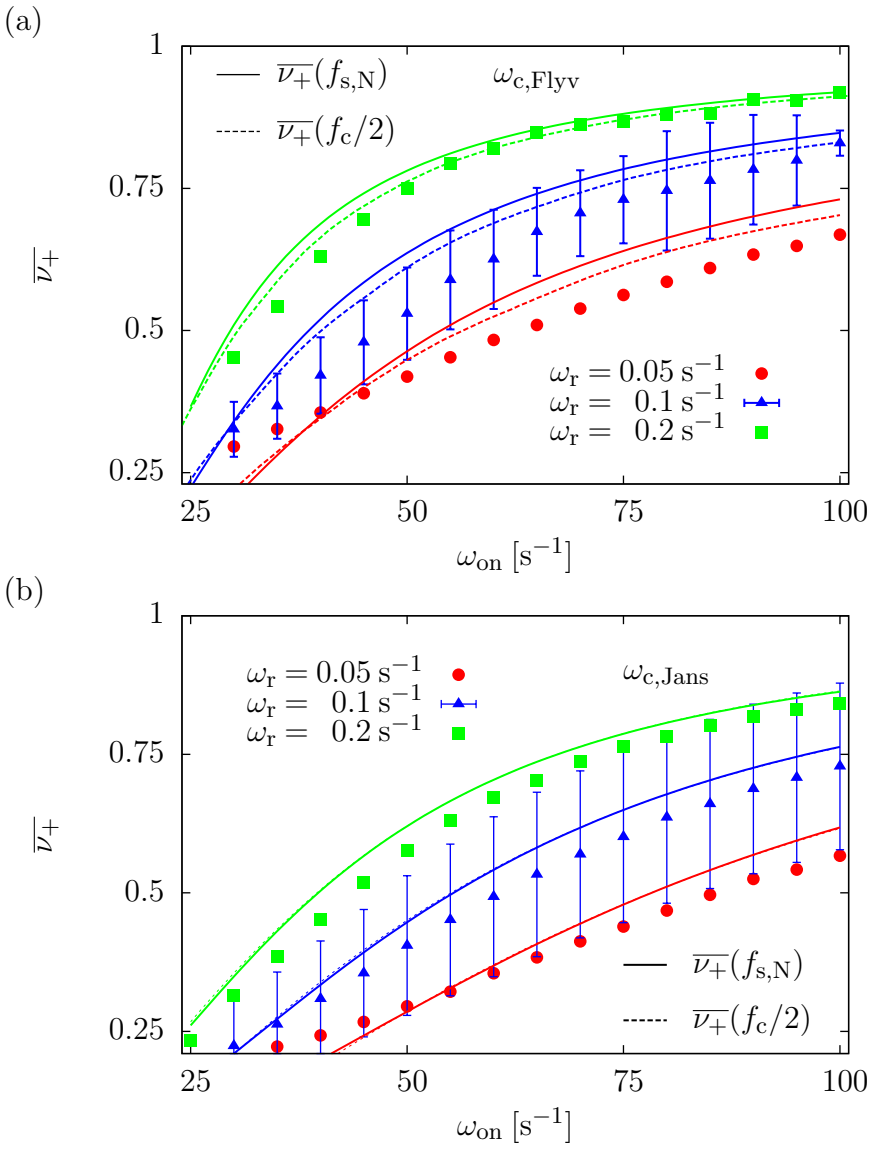

Figure 8.8: Time-averaged pushing fraction $\overline{\nu_+} = \langle\overline{n_+}\rangle/N$ of MTs as a function of ω_{on} for soft barrier with $k = 10^{-7}$ N/m. Data points: Simulation results for different rescue rates $\omega_r = 0.05\,\mathrm{s}^{-1}$ (●), $0.1\,\mathrm{s}^{-1}$ (▲), and $0.2\,\mathrm{s}^{-1}$ (■). Error bars represent the standard deviation of the stochastic quantity $\overline{\nu_+}$. For reasons of clarity we only show error bars for $\omega_r = 0.1\,\mathrm{s}^{-1}$. All other standard deviations are of the same magnitude. Solid lines: Solution of eq. (8.16) for $f = f_c/2$. Dashed lines: Solution of eq. (8.16) for $f = F_{\mathrm{s,N}}/N$ with $F_{\mathrm{s,N}}$ from the numerical mean-field solution including stochastic effects. (a): Simulation and analytical results using the Flyvbjerg catastrophe model with $F_0 \simeq 7$ pN. (b): Simulation and analytical results using the Janson catastrophe model with $F_0 \simeq 0.8$ pN.

differences between both systems. Erdmann *et al.* investigated the stochastic dynamics of clusters of molecular bonds under a constant force [87, 88]. They considered a cluster of N parallel bonds under a constant force F. Each bond can either be open or closed. The force F is shared equally between all closed bonds, so that each closed bond is subject to the force F/i, where i is the number of closed bonds. In the context of MT ensembles, a closed bond corresponds to one of the leading n_+ MTs and an open bond to a non-leading MT. The dissociation rate of a single bond under force is $k_{\mathrm{diss}} = k_0 \exp(F/F_0 i)$, which is equivalent to the exponential approximation of the catastrophe rate $\omega_{\mathrm{c}}(F/F_0 n_+) \sim \omega_{\mathrm{c}}(F=0)\exp(F/F_0 n_+)$ for $F/F_0 > 1$ and n_+ leading MTs [see eq. (2.37)]. The rebinding of a single bond corresponds to a rescue event of a single MT. After rebinding, single bonds instantaneously attach to the adhesion cluster. In contrast, single MTs have to catch up to the leading MTs, which continue to grow against the elastic obstacle. The inverse "catch-up" time is larger than the bare rescue rate and is a function of the force (see Sec. 8.2.2). Without rebinding the number i of closed bonds decays constantly until the absorbing boundary at $i = 0$ is reached. No steady state is reached. In the absence of rescue events, a decay of the number n_+ of simultaneously pushing MTs toward the absorbing boundary at $n_+ = 0$ is also observed in the dynamics of a MT ensemble. As in the case of molecular bonds no steady state is reached (see Sec. 8.1). Under a constant force both systems are described by the same linear one-step master equation [see eq. (8.36)]. In both systems the stochastic dynamics is governed by the number of bonds/MTs, the rebinding/rescue rate, and the dissociation/catastrophe rate. However, for a MT ensemble growing against an elastic obstacle, the dynamics of the resisting force F crucially affects the ensemble dynamics. This leads us to the major difference between both systems. The force acting on the bond cluster is constant, whereas in the case of the MT ensemble the force increases linearly with the length $x(t)$ of the leading MTs. The stochastic dynamics of the MT ensemble is coupled to the dynamics of the resisting force via $\dot{F} = k\dot{x}(t)$. For a soft obstacle and in the presence of rescue events, this leads to a remarkable difference in the cooperative dynamics between both systems. Under a constant force and even with rebinding the bond cluster exhibits a finite lifetime, before its complete dissociation. If all bonds are open, that is $i = 0$, the dynamics stops. This resembles a MT ensemble in a collective phase of growth, followed by a collective catastrophe. Here the complete dissociation of the bond cluster corresponds to a collective catastrophe with $n_+ = 0$ pushing MTs. But in contrast to the bond cluster, the MT ensemble dynamics does not stop, since n_+ corresponds to a collective phase of shrinkage. In a phase of collective shrinkage, the resisting force is reduced via $\dot{F} \sim -kv_-$, until a collective rescue induces a new phase of collective growth. The coupling of the stochastic MT dynamics to the force dynamics allows the system to organize itself into a steady state (see Sec. 8.2.1). To conclude, both systems are closely related to each other, but the additional force dynamics in the case of MT ensembles leads to major differences in

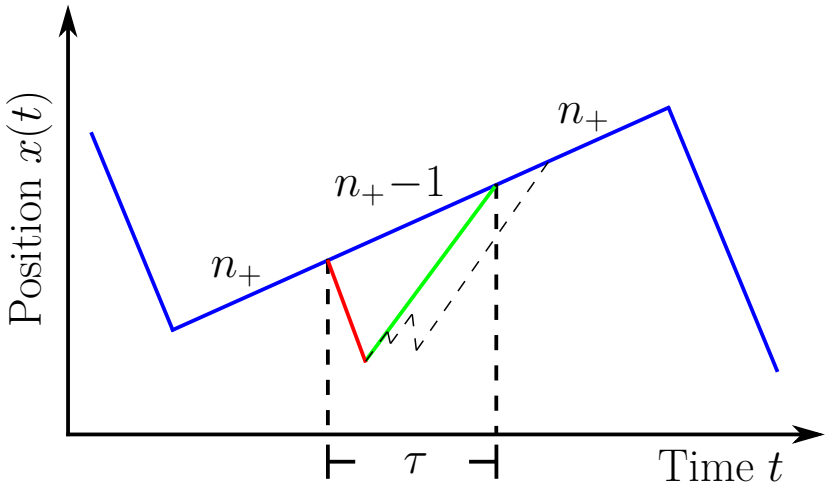

Figure 8.9: Illustration of time scale τ from eq. (8.7). Blue solid line: The obstacle position $x(t)$ is the position of the n_+ leading MTs. Red solid line: Single MT shrinking after catastrophe. Green solid line: Single MT growing force-free after rescue without additional catastrophe and rescue events [see eq. (8.7)]. Dashed black line: Single MT growing force-free after rescue with additional catastrophe and rescue events [see eq. (8.6)]. These more complex "catch-up" processes are not included in the description.

the cooperative dynamics, and allows the MT ensemble to reach a steady state.

8.2.2 Dynamical mean field theory

We will show that all simulation results and the robustness with respect to the catastrophe model can be explained based on a dynamical mean-field theory.

In the presence of rescue events, the mean-field equation (8.1) for $\langle n_+ \rangle$ becomes modified in the growing phase. The one-step master equation for n_+ in a growing phase also contains a forward rate $g_{n_+} = (N - n_+)\tau^{-1}$ for increasing n_+ by one. This forward rate is determined by a rescue and "catch-up"process for the $(N - n_+)$ MTs, which are not pushing: The time τ denotes the mean time that it takes for a MT to rejoin the group of n_+ pushing MTs after undergoing an individual catastrophe followed by rescue and force-free growth at a velocity $v_+(0)$ that is larger than the velocity $v_+(F/n_+)$ of the leading MTs under force (see Fig. 8.9).

After a rescue time $1/\omega_r$ the trailing MT has to "catch-up" a distance $[v_+(F/n_+) + v_-]/\omega_r$ to the leading MTs, which kept growing with velocity $v_+(F/n_+)$.

The force-free growing MT is still subject to dynamic instability, thus stochastic catastrophe and rescue events, and its dynamics is characterised by the force-free characteristic length parameter $\lambda(0)$ [see eq. (2.4)]. For $\lambda < 0$ the trailing MT shrinks, on average, back to zero length and does not return to the leading MT . We therefore focus on $\lambda(0) > 0$, which corresponds to an average force-free velocity of growth $\langle v(0) \rangle = J(0) > 0$ [see eq. (2.7)].

Given a velocity difference $\langle v(0)\rangle - v_+(F/n_+)$ to the leading MTs under force, the "catch-up" requires a time

$$\tau \approx \omega_r^{-1}\left[1+(v_+(F/n_+)+v_-)/(\langle v(0)\rangle - v_+(F/n_+))\right] \tag{8.6}$$

which is larger than the bare rescue time $1/\omega_r$ (see Fig. 8.9). We require $\langle v(0)\rangle > v_+(F/n_+)$ and focus on $\omega_r \gg \omega_c(0)$ and $v_+(0)\omega_r \gg v_-\omega_c(0)$. $\langle v(0)\rangle$ can than be approximated by $\langle v(0)\rangle \approx v_+(0)$ [see eq. (2.7)] and from eq. (8.6) follows:

$$\tau \approx \omega_r^{-1}\left[1+(v_+(F/n_+)+v_-)/(v_+(0) - v_+(F/n_+))\right]. \tag{8.7}$$

Geometrically this can be interpreted as a single rescue event followed by force-free growth with velocity $v_+(0)$ and no further catastrophe and rescue events. In Fig. 8.9, a sketch of a "catch-up" process is depicted.

Including "catch-up" processes into the description, results in a modified mean-field equation for $\langle n_+\rangle$,

$$d\langle n_+\rangle/dt = -\omega_c\left(\langle F\rangle/\langle n_+\rangle\right)\langle n_+\rangle + \langle\tau\rangle^{-1}\left(N - \langle n_+\rangle\right) \tag{8.8}$$

where we have to apply the mean field averaging also to $\langle\tau\rangle$ in eq. (8.7):

$$\langle\tau\rangle \approx \omega_r^{-1}\left[1+\frac{v_+(\langle F\rangle/\langle n_+\rangle)+v_-}{v_+(0)-v_+(\langle F\rangle/\langle n_+\rangle)}\right]. \tag{8.9}$$

Typically $\langle\tau\rangle$ is by a factor of 10 larger than the bare rescue time $1/\omega_r$.

8.2.3 Limit cycle oscillations and absence of bifurcations

For the further analysis of the mean-field dynamics it is advantageous to introduce new variables, the average force per MT f and the average fraction ν_+ of pushing MTs,

$$f \equiv \langle F\rangle/N, \quad \nu_+ \equiv \langle n_+\rangle/N \tag{8.10}$$

with $\langle F\rangle/\langle n_+\rangle = f/\nu_+$. Using these variables, the mean-field equations become

$$d\nu_+/dt = -\nu_+\omega_c\left(f/\nu_+\right) + \left(1-\nu_+\right)/\langle\tau\rangle \tag{8.11}$$

$$df/dt = kv_+\left(f/\nu_+\right)/N \tag{8.12}$$

From eqs. (8.11) and (8.12) we can estimate typical timescales of the corresponding dynamics and test the assumption of a fast ν_+-dynamics compared to the f-dynamics. With $\omega_c(f/\nu) \sim \omega_c(0)\exp(f/\nu)$ [eq. (2.37)] and $\tau^{-1}(f/\nu) \sim \omega_r/10$, the general solutions of eqs. (8.11) and (8.12) are given by:

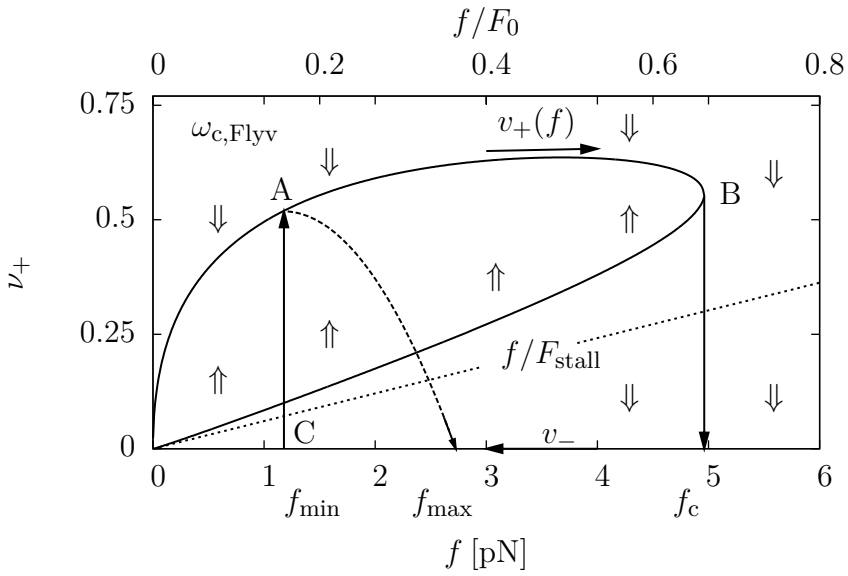

Figure 8.10: Nullclines of the mean-field equations for the Flyvbjerg model for $\omega_{on} = 70\,s^{-1}$, $\omega_r = 0.05\,s^{-1}$, and $k = 10^{-7}$ N/m (soft barrier). The nullclines of $\nu_+ \equiv \langle n_+\rangle/N$ are solutions of eq. (8.16) and assume a loop shape as a function of $f \equiv \langle F\rangle/N$. Open arrows indicate the mean-field flow of $\langle n_+\rangle$. The nullcline for f is a straight line $\nu_+ = f/F_{stall}$ (dotted). The critical force is $f_c = F_c/N \simeq 5$ pN for the Flyvbjerg model. Black arrows indicate the stable mean-field limit cycle; dashed line indicates effect of stochastic fluctuations.

$$\frac{t}{\tau_f} = F_0^{-1} \int \left[\exp(f/\nu_+) - \frac{\omega_{off}}{\omega_{on}}\right]^{-1} df + \text{const.} \tag{8.13}$$

$$\frac{t}{\tau_{\nu_+}} \approx \int \left[\frac{\omega_r}{10\omega_c(0)}(1-\nu_+) - \exp(f/\nu_+)\,\nu_+\right]^{-1} d\nu_+ + \text{const.} \tag{8.14}$$

with $\tau_f = F_0 N/(kd\omega_{on})$ and $\tau_{\nu_+} = \omega_c(0)$. For $k = 10^{-7}$ N/m, $F_0 \simeq 7$ pN and typical values of N and ω_{on}, we find $\tau_f \approx 10^4$ s and $\tau_{\nu_+} \approx 10^3$ s. In general, the ν_+-dynamics is by a factor of 10 faster than the f-dynamics, which agrees to the assumption of a fast ν_+-dynamics. We first discuss the nullclines of f and ν_+, i.e., the contours in the f-ν_+ plane along which $df/dt = 0$ and $d\nu_+/dt = 0$ is satisfied, respectively.

The nullclines of f require $v_+(f/\nu_+) = 0$, which leads to a straight line,

$$f = \nu_+ F_{stall} \tag{8.15}$$

in the f-ν_+ plane, where the slope is given by the single-MT stall force $F_{stall} = F_0 \ln(\omega_{on}/\omega_{off})$ (see Fig. 8.10).

The nullclines of ν_+ are given by

$$0 = g(f,\nu_+) \equiv -\nu_+\omega_c(f/\nu_+) + \frac{1}{\langle\tau\rangle(f/\nu_+)}(1-\nu_+) \tag{8.16}$$

or equivalently

$$\nu_+ = \left[\omega_c\left(f/\nu_+\right)\tau\left(f/\nu_+\right)+1\right]^{-1} \tag{8.17}$$

and are *independent* of N. The shape of the nullclines depends on the functional dependence of the catastrophe rate on the force and, thus, on the catastrophe model. We will first focus on the Flyvbjerg catastrophe model, for which the nullclines of ν_+ have a characteristic loop shape, as shown in Fig. 8.10, which exhibits two solution branches: a *stable* upper branch $\nu_{+,u}$ corresponding to a collectively growing state with $\langle n_+\rangle = N\nu_{+,u}$ pushing MTs and an *unstable* lower branch $\nu_{+,l}$. For a soft barrier, the $\langle n_+\rangle$-dynamics is fast, and the force increases slowly during collective growth, while $\nu_+ = \nu_{+,u}$ is tracing the stable upper branch of the nullcline. The force per MT can increase up to a critical value f_c (with a corresponding value ν_c for ν_+), where stable and unstable branch join and where the nullcline has vertical slope $df/d\nu_+ = 0$ in the f-ν_+ plane. The critical force $F_c = f_c N$ represents the maximal load force for which the MT ensemble can maintain a stable state of collective growth. For $\langle F\rangle > F_c$ the number $\langle n_+\rangle$ of pushing MTs has to flow spontaneously to a state $\langle n_+\rangle = 0$.

The critical force f_c per MT can be obtained from two conditions: (i) the nullcline equation $g(f,\nu_+) = 0$, i.e., eq. (8.16), and (ii) taking a total derivative with respect to ν_+ and using the condition of a vertical slope $df/d\nu_+ = 0$ we arrive at the second condition $\frac{\partial}{\partial\nu_+} g(f,\nu_+) = 0$. Because $\omega_c(F)$ increases exponentially above F_0, see eq. (2.39), $d\omega_c/dF \sim \omega_c/F_0$ is a good approximation. The effective rescue time $\langle\tau\rangle = \langle\tau\rangle(f/\nu_+)$ has a much weaker force dependence, which we neglect. These approximations give

$$\begin{aligned} 0 &\approx -\omega_c(f/\nu_+)\left(1-\frac{f}{\nu_+ F_0}\right) - \frac{1}{\langle\tau\rangle(f/\nu_+)} \\ \frac{f}{\nu_+ F_0} &\approx 1 + \frac{1}{\omega_c(f/\nu_+)\langle\tau\rangle(f/\nu_+)} \end{aligned} \tag{8.18}$$

It turns out that (for both the Flyvbjerg and the Janson catastrophe models) $\omega_c\langle\tau\rangle \geq 1$ holds over the entire range of forces. In order to estimate f_c, we assume $\omega_c\langle\tau\rangle \gg 1$. This leads to an estimate $\frac{f}{\nu_+} \approx F_0$ in eq. (8.18), which can be used in the arguments of ω_c and $\langle\tau\rangle$. Solving the eqs. (8.16) and (8.18) for f_c and ν_c we find analytical estimates,

$$f_c \approx F_0 \frac{1}{\omega_c(F_0)\,\langle\tau\rangle(F_0)} \tag{8.19}$$

$$\nu_c \approx \frac{1}{1+\omega_c(F_0)\,\langle\tau\rangle(F_0)}. \tag{8.20}$$

According to eqs. (8.15) and (8.16), the nullclines for f and ν_+ and, thus, the critical values f_c and ν_c are strictly *independent* of N. Therefore, the critical total force $F_c = Nf_c$ has to be strictly *linear* in the number of MTs. The critical force is the maximal polymerization force that can be generated during polymerization in the presence of rescue

events. For a soft barrier ($N \gg \alpha$), rescues thus lead to a significant increase in the maximal polymerization force with a linear N dependence compared to the logarithmic dependence derived above in the absence of rescues. Moreover, the estimate (8.19) for f_c predicts an increase of the generated force with the on-rate ω_{on} because this increases v_+ and, thus, reduces ω_c and an increase with the rescue rate ω_r because this decreases $\langle\tau\rangle$ [see eq. (8.6)].

In order to analyze the system for fixed points, we compare the lower branch $\nu_{+,l}$ of the nullcline of ν_+ with the nullcline of f [see eq. (8.15)]. The lower branch is governed by the exponential increase $\omega_c(F) \sim \omega_c(0)\exp(cF/F_0)$ with force (with $c = 2/3$ in the Flyvbjerg and $c = 1$ in the Janson catastrophe model) resulting in $\omega_c(0)\exp(cf/\nu_+F_0) \sim 1/\langle\tau\rangle\nu_+$ or $f/\nu_+ \approx F_0\ln(1/\omega_c(0)\langle\tau\rangle\nu_+)/c$. This is always at *lower* forces than the nullcline [eq. 8.15)] of f because $F_{stall} = F_0\ln(\omega_{on}/\omega_{off}) \gg F_0\ln(1/\omega_c(0)\langle\tau\rangle\nu_+)/c$. This inequality can be violated only at very high rescue rates ω_r giving rise to a small $\langle\tau\rangle$. We obtained that $\omega_r \gg 1/s$ is necessary to obtain a fixed point. Only if this fixed point exists *and* is stable, it can undergo a Hopf bifurcation on lowering the rescue rate. We conclude that, for realistic parameter values $\omega_r \sim 0.05\,s^{-1}$, we are always far from a Hopf bifurcation.

The system rather *oscillates* in a *stable limit cycle*: After rescue (A in Fig. 8.10), the pushing force f increases with the MT growth velocity because of $\dot{f} = kv_+/N$, while $\nu_+ = \nu_{+,u}$ is tracing the stable branch of the nullcline. At the critical force level f_c, a collective catastrophe occurs (B in Fig. 8.10), where the ensemble is quickly driven to collective shrinking with $\langle n_+\rangle = 0$ or 1 and $\dot{f} = -kv_-/N$.

During shrinking the force level is reduced until an individual rescue event can initiate a collective rescue at a force F_{min} (C in Fig. 8.10). During rescue $\langle n_+\rangle$ increases quickly back to its stable fixed point value (A in Fig. 8.10) closing the limit cycle.

The collective rescue force F_{min} can be calculated from the condition that the lower unstable branch of the nullcline given by eq. (8.16) intersects the line $\langle n_+\rangle = 1$, leading to the condition

$$N = \omega_c(F_{min})\langle\tau\rangle(F_{min}) + 1. \tag{8.21}$$

Collective rescue typically happens at rather small force $F_{min} \ll F_0$ such that we find an essentially linear N dependence $F_{min} \sim N + \mathcal{O}(1)$.

The collective mean-field dynamics thus oscillates between forces F_{min} and F_c. The resulting time-averaged polymerization force

$$F_{s,N} = \overline{\langle F\rangle} \approx (F_{min} + F_c)/2 \tag{8.22}$$

is also *linear* in N. This is in agreement with the simulation results [see Fig. 8.6(a)]. Because $F_c \gg F_{min}$ the result $F_c \approx NF_0/[\omega_c(F_0)\langle\tau\rangle(F_0)]$ from eq. (8.19) determines the dependence of the polymerization force $F_{s,N}$ on the on-rate ω_{on} and the rescue rate ω_r. The estimate for F_c predicts an increase of the generated force with the on-rate ω_{on} because

this increases v_+ and, thus, reduces ω_c. For the velocity dependence (2.39) and assuming $v_+ \propto \omega_{on}$ (for $\omega_{on} \gg \omega_{on}$), eq. (8.19) gives $F_c \propto \omega_{on}^{2/3}$ for the Flyvbjerg catastrophe model (and $F_c \propto \omega_{on}$ for the Janson catastrophe model), which is in qualitative agreement with the simulation result of an approximately linear increase of the polymerization force with the on-rate ω_{on} in Fig. 8.7(a) and 8.7(b). From the result (8.19), we also predict an increase of the polymerization force with the rescue rate ω_r because this decreases $\langle\tau\rangle$. The pronounced increase of $F_{s,N}$ with the on-rate ω_{on} demonstrates that for an MT ensemble, the polymerization force can be sensitively regulated by changing the concentration of available monomers. We also find the collective stall force $F_{s,N}$ always remains much smaller than the N-fold single-MT stall force, $F_{s,N} \ll NF_{stall}$ [see Figs. 8.6(a) and 8.6(b)] in contrast to force-sharing filaments without dynamic instability, where $F_{s,N} = NF_{stall}$ holds exactly [66]. A further confirmation of the mean-field theory is provided by simulation results for the time-averaged pushing fraction $\overline{\nu_+} = \langle\overline{n_+}\rangle/N$ in Figs. 8.8(a) and 8.8(b). Mean field results for ν_+ evaluated using the nullcline eq. (8.16) for $f = F_{s,N}/N$ show good agreement with the simulations results.

The oscillatory limit cycle dynamics, which gives rise to collective catastrophe and rescue oscillations, is robust against perturbations because the system is far from a bifurcation for realistic rescue rates. Only for very high rescue rates $\omega_r \gg 1/s$, does a stable fixed point exist, which becomes unstable in a Hopf bifurcation on lowering the rescue rate.

Similar collective catastrophes and rescues are also observed in *in vitro* bulk polymerization experiments [89, 90]. In these experiments *many* MTs synchronously polymerize in a solution with GTP-tubulin concentration c_{GTP}. All MTs share the available concentration c_{GTP} and grow with a velocity $v_+(c_{GTP})$, which decreases if GTP-tubulin is consumed. Here, collective catastrophes and rescues are caused by sharing the concentration c_{GTP} of available GTP-tubulin, resulting in similar collective oscillations as force-sharing induces in the present system.

Finally, we want to note that the collective dynamics for $N \gg 1$ that we described here differs markedly from the dynamics of a *single* MT ($N = 1$) (see Sec. 4.3)[55]. For a single MT rescue does not happen at a particular force level F_{min} but after an average time $1/\omega_r$ set by the individual rescue rate. The resulting $N = 1$ mean-field equation for the average force $\langle F\rangle$ is $v_-/\omega_r = v_+(\langle F\rangle)/\omega_c(\langle F\rangle)$ [see eq. (4.32)] and equals shrinking and growing distance between individual rescue and catastrophe events.

8.2.4 Robustness with respect to catastrophe models

An essential requirement for the existence of an oscillatory limit cycle is the loop shape of the nullclines of $\langle n_+\rangle$ according to the stationary mean-field equation (8.16) (see Fig. 8.10). Results presented so far have been derived from the Flyvbjerg model. We obtain a very similar loop-shaped nullcline also with the catastrophe model by Janson *et al.* [see

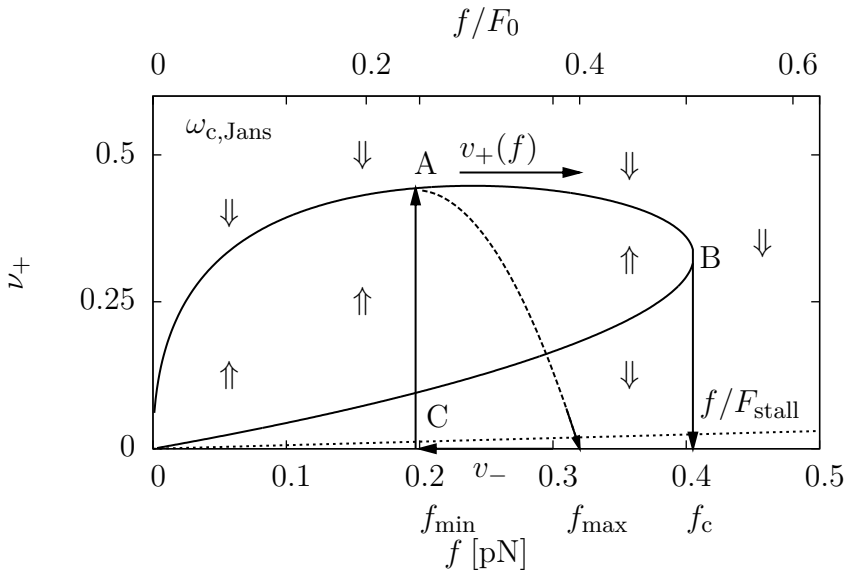

Figure 8.11: Nullclines of the mean-field equations for the Janson model for $\omega_{on} = 70\,s^{-1}$, $\omega_r = 0.05\,s^{-1}$, and $k = 10^{-7}$ N/m (soft barrier). The nullclines of $\nu_+ \equiv \langle n_+ \rangle / N$ are solutions of eq. (8.16) and assume a loop shape as a function of $f \equiv \langle F \rangle / N$. Open arrows indicate the mean-field flow of $\langle n_+ \rangle$. The nullcline for f is a straight line $\nu_+ = f/F_{stall}$ (dotted). The critical force is $f_c \simeq 0.4$ pN for the Janson model. Black arrows indicate the stable mean-field limit cycle; dashed line indicates effect of stochastic fluctuations.

Fig. 8.11].

The condition for a loop-shape nullcline is the existence of a critical force F_c, where the two solution branches of eq. (8.16) merge in a point with a vertical tangent. From eq. (8.16), we can derive the necessary condition

$$0 < \tau^{-1} < \omega_c(F) - F \frac{d}{dF} \omega_c(F) \tag{8.23}$$

for the existence of a critical force F_c. Therefore, we expect the same type of oscillatory limit cycle for collective catastrophe and rescue oscillations for a large class of catastrophe models which fulfill the two following conditions:

(i) The catastrophe rate $\omega_c = \omega_c(v_+)$ is a function of the growth velocity only.

(ii) The resulting force dependence fulfills condition (8.23), which gives rise to a catastrophe rate increasing exponentially with force above the characteristic force F_0.

Whereas the Flyvbjerg and Janson catastrophe models and, more generally, all models with $\omega_c \propto v_+^{-\varepsilon}$ ($\varepsilon > 0$) fulfill condition (8.23), it is violated for the linear catastrophe model eq. (2.40).

This explains that the mean-field result of an oscillatory limit cycle is robust with respect to variations of the catastrophe models: We expect qualitatively similar behavior for all

catastrophe rates $\omega_c(F)$, which are exponentially increasing with force above a characteristic force F_0, for example, in the standard catastrophe models by Flyvbjerg *et al.* [18, 68] or by Janson *et al.* [75]. This explains the robustness observed in the simulation results as shown in Figs. 8.4 and 8.3 , and Figs. 8.6, 8.7 and 8.8.

The condition (8.23) is violated for the linear catastrophe model [see eq. (2.40]. Accordingly, we do not expect to find an oscillatory limit cycle with collective catastrophe and rescue events. For this type of catastrophe model the nullclines are indeed no longer loop shaped, and the mean-field theory rather predicts a *stable* fixed point [see Fig. 8.12(b)]. Simulations confirm that collective catastrophe and rescue oscillations are absent for the linear catastrophe model, and we find a rather stationary position x of the obstacle and, thus, a stationary polymerization force [see Fig. 8.12(a)].

We investigate the stability of the intersection point by a linear stability analysis [91]. The coordinates of the intersection point are ν_+^* and f^*, and are determined numerically from eqs. (8.15) and (8.16) as a function of the growth parameters. From eqs. (8.11) and (8.12) we obtain the following Jacobian matrix

$$\underline{\underline{J}} = \begin{pmatrix} A & B \\ C & D \end{pmatrix}_{(\nu_+^*, f^*)} \tag{8.24}$$

with

$$\begin{aligned} A &= \frac{\partial}{\partial \nu_+}\left[-\nu_+\omega_c(f/\nu_+) + (1-\nu_+)\tau^{-1}(f/\nu_+)\right] \\ &= -\omega_c(f/\nu_+) - \tau^{-1}(f/\nu_+) + \left[\frac{(1-\nu_+)\omega_r}{(v_+(0)+v_-)\nu_+} + \tilde{b}\right]\frac{f\omega_{on}d}{F_0\nu_+}\exp\left(\frac{-f}{F_0\nu_+}\right), \end{aligned} \tag{8.25}$$

$$\begin{aligned} B &= \frac{\partial}{\partial f}\left[-\nu_+\omega_c(f/\nu_+) + (1-\nu_+)\tau^{-1}(f/\nu_+)\right] \\ &= \left[\frac{(1-\nu_+)\omega_r}{(v_+(0)+v_-)\nu_+} - \tilde{b}\right]\frac{\omega_{on}d}{F_0}\exp\left(\frac{-f}{F_0\nu_+}\right), \end{aligned} \tag{8.26}$$

$$C = \frac{\partial}{\partial \nu_+}\left[\frac{k}{N}v_+(f/\nu_+)\right] = \frac{kfd\omega_{on}}{NF_0\nu_+^2}\exp\left(\frac{-f}{F_0\nu_+}\right), \tag{8.27}$$

$$D = \frac{\partial}{\partial f}\left[\frac{k}{N}v_+(f/\nu_+)\right] = \frac{kfd\omega_{on}}{NF_0\nu_+}\exp\left(\frac{-f}{F_0\nu_+}\right). \tag{8.28}$$

With $\alpha = \mathrm{tr}(\underline{\underline{J}})$ and $\beta = \det(\underline{\underline{J}})$, the eigenvalues of the Jacobian matrix (8.24) are given by

$$\Gamma_{1,2} = \left.\frac{\alpha \pm \sqrt{\alpha^2 - 4\beta}}{2}\right|_{(\nu_+^*, f^*)}. \tag{8.29}$$

For a fixed set of growth parameters, both eigenvalues are evaluated at the intersection point of eq. (8.15) and eq. (8.16) with $\nu_+ = \nu_+^*$ and $f = f^*$. Results are depicted in Fig. 8.13.

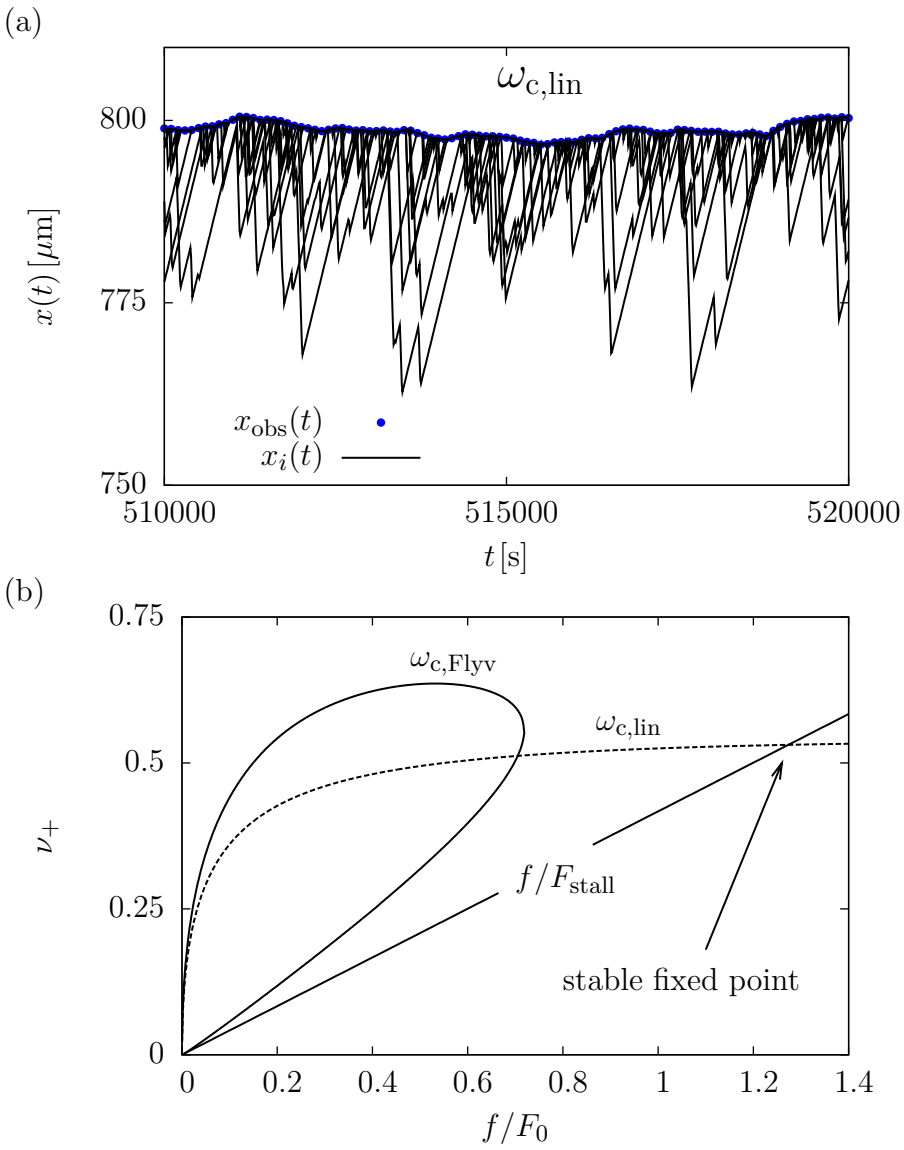

Figure 8.12: (a): Typical simulation trajectories for $N = 10$ MTs, $\omega_{\mathrm{on}} = 70\ \mathrm{s}^{-1}$, $\omega_{\mathrm{r}} = 0.05\ \mathrm{s}^{-1}$ and for the linear catastrophe model. (a): Positions of all MTs as a function of time t (solid lines); the obstacle position $x_{\mathrm{obs}}(t)$ (blue, filled dots) is the position of the leading MTs (only every 100th data point shown). (b): Nullclines of the mean-field equations for the linear model (dashed line) (2.40) with $\widetilde{a} = 0.005\ \mathrm{s}^{-1}$ and $\widetilde{b} = 8 \times 10^4\ \mathrm{m}^{-1}$ and for the Flyvbjerg model (solid line). We use $\omega_{\mathrm{on}} = 70\ \mathrm{s}^{-1}$, $\omega_r = 0.05\ \mathrm{s}^{-1}$, and $k = 10^{-7}$ N/m (soft barrier). For the linear catastrophe model, the nullcline for $\nu_+ \equiv \langle n_+ \rangle / N$ is not loop-shaped. A stable fixed point exists at the intersection with the nullcline for f, which is the straight line $\nu_+ = f/F_{\mathrm{stall}}$.

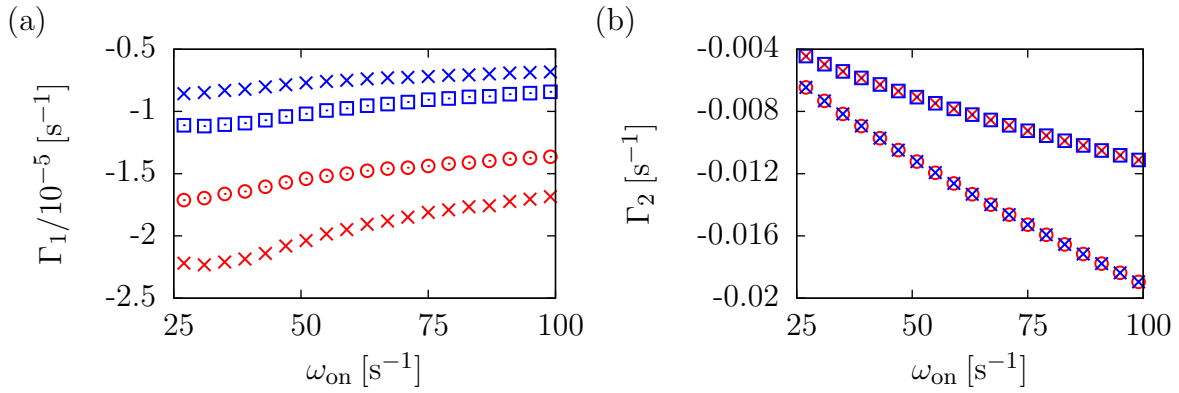

Figure 8.13: Eigenvalue $\Gamma_{1,2}$ of the Jacobian matrix [eq. (8.24)] as a function of ω_{on} and ω_r for $N = 5$ (red) and $N = 10$ (blue). $\Gamma_{1,2}$ are calculated from eq. (8.29). (a): Eigenvalue Γ_1 as a function of ω_{on} for $N = 5$ (red), $\omega_r = 0.05\,s^{-1}$ (×) and $\omega_r = 0.1\,s^{-1}$ (⊙). Eigenvalue Γ_1 as a function of ω_{on} for $N = 10$ (blue), $\omega_r = 0.05\,s^{-1}$ (×) and $\omega_r = 0.1\,s^{-1}$ (⊡). (b): Eigenvalue Γ_2 as a function of ω_{on} for $N = 5$ (red), $\omega_r = 0.05\,s^{-1}$ (×) and $\omega_r = 0.1\,s^{-1}$ (⊙). Eigenvalue Γ_2 as a function of ω_{on} for $N = 10$ (blue), $\omega_r = 0.05\,s^{-1}$ (×) and $\omega_r = 0.1\,s^{-1}$ (⊡).

For realistic parameter values (see Table A.1), both eigenvalues Γ_1 and Γ_2 are less than zero. The intersection point of the nullclines [see eq. (8.15) and eq. (8.16)] is stable with respect to small perturbations in ν_+ and f. However, both eigenvalues are functions of the catastrophe parameters $\tilde{a}$ and $\tilde{b}$. A different choice of $\tilde{a}$ and $\tilde{b}$ may lead to a change of sign in one of the two eigenvalues and, therefore, to an unstable intersection point.

8.2.5 Improved mean-field theory including stochastic fluctuations

The dynamical mean-field theory explains all simulation results qualitatively. In order to obtain quantitative agreement with stochastic simulations, we have to take into account that the maximal force F_{max} for a collective catastrophe is typically *smaller* than the critical mean-field force F_c (see Figs. 8.6 and 8.7) because of additional stochastic fluctuations of n_+, which reduce n_+ and decrease the time spend in a collective state of growth, that is the first passage-time to a shrinking state $n_+ = 0$ (see Figs. 8.10 and 8.11).

This reduction is governed by the mean first passage time T for a discrete one-step process with forward rates g_{n_+} and reverse rates r_{n_+},

$$\begin{aligned} g_{n_+} &= \tau^{-1}(N - n_+) \\ r_{n_+} &= \omega_c(F/n_+)n_+, \end{aligned} \tag{8.30}$$

starting from the stable $n_+ = \langle n_{+,u} \rangle = N\nu_{+,u}$ on the upper branch of the nullcline (with

a reflecting boundary at $n_+ = N$) to reach the absorbing boundary $n_+ = 0$ [62],

$$T(f_{\max}, N, \langle n_{+,\mathrm{u}} \rangle) = \sum_{\lambda=1}^{\langle n_{+,\mathrm{u}} \rangle} \sum_{\mu=\lambda}^{N} \frac{\prod_{i=\lambda}^{\mu-1} g_i}{\prod_{j=\lambda}^{\mu} r_j} = \sum_{\lambda=1}^{\langle n_{+,\mathrm{u}} \rangle} \sum_{\mu=\lambda}^{N} \frac{1}{r_\mu} \exp\left[\ln\left(\prod_{i=\lambda}^{\mu-1} \frac{g_i}{r_i}\right)\right]. \tag{8.31}$$

We want to note, that $n_+ = 0$ only acts as an absorbing boundary to calculate the MFPT from the stable upper branch of the nullcline to a state with $n_+ = 0$. At $n_+ = 0$ a collective state of growth ends and a collective state of shrinkage begins. The overall MT dynamics does not stop at $n_+ = 0$.

The mean first passage time T depends on f, N, and $\langle n_{+,\mathrm{u}} \rangle$ via the forward and reverse rates.

The force $f_{\max}$ is the load force that is reached by collective growth with a velocity $v_+(f/\nu_{+,u})$ during the MFPT T. Therefore, the maximal ensemble force $f_{\max}$ is determined self-consistently by the condition

$$T(f_{\min}, f_{\max}, N, \nu_{+,\mathrm{u}}) = \frac{N}{k} \int_{f_{\min}(N)}^{f_{\max}} df v_+^{-1}(f/\nu_{+,\mathrm{u}}). \tag{8.32}$$

This equation has to be solved together with the fixed point equation for $\nu_{+,\mathrm{u}}$ [eq. (8.17)] to obtain $f_{\max}$ as a function of N and the remaining system parameters.

To gain insight into the N-dependence of the maximal ensemble force $f_{\max}$, we can determine the N-dependence of T by approximating sums by integrals and introducing functions

$$\begin{aligned} g(\nu_+) &\equiv g_{n_+}/N = \tau^{-1}(f/\nu_+)(1-\nu_+) \\ r(\nu_+) &\equiv r_{n_+}/N = \nu_+ \omega_{\mathrm{c}}(f/\nu_+). \end{aligned} \tag{8.33}$$

We finally find

$$T \approx N \int_0^{\nu_{+,u}} dx \int_x^1 dy \frac{1}{r(y)} \exp\left[N \int_x^y da \ln\left(\frac{g_+(a)}{r_+(a)}\right)\right]. \tag{8.34}$$

It is important to note that T is of the form $T \sim N \exp[N u(f_{\max}, \nu_{+,u})]$ with some function u. T is essentially linear in N for small N but starts to increase faster than linear for larger N. Because $\nu_{+,\mathrm{u}}$ is independent of N according to the fixed point equation (8.17) for $\nu_{+,\mathrm{u}}$, and using the condition (8.32) determining $f_{\max}$, this leads to an approximately constant $f_{\max}$ for small $N < 10$, which starts to increase for larger N.

In Fig. 8.6 we show the time averaged MT ensemble force $F_{s,N}$ as a function of MT number N and different on-rates ω_{on}. The improved mean-field results are in qualitative and quantitative agreement with results from full stochastic simulations. This is in contrast

to pure mean-field results (see Sec. 8.2.3), which reproduce simulation results qualitatively well, but differ quantitatively. For large values of N and ω_{on}, the improved mean-field results overestimate simulations results, due to the exponential increases of the MFPT for large N and ω_{on} [see eq. (8.34)].

Fig. 8.7 shows $F_{s,N}$ as a function of the on-rate ω_{on} for different MT numbers N. Again we find good agreement between improved mean-field and simulation results.

In Fig. 8.8 the pushing fraction $\overline{\nu_+} = \langle \overline{n_+} \rangle / N$ of MTs is depicted. Also for this quantity, our improved mean-field theory agrees well with the full stochastic simulation results. In addition we find no considerable difference between pure and improved mean-field results. With the improved mean-field theory, we can also get quantitative results for the average time spend in a growing state, which is roughly half of the average period of collective steady state oscillations. In a period of growth, the system traces the upper part of the nullcline with average velocity $v_+(f/\nu_+)$, starting at f_{min}. In mean field approximation the average time spend in a collective state of growth, between f_{min} and the force f, is than given by

$$T(f_{\text{min}}, f, N, \nu_{+,\text{u}}) = \frac{N}{k} \int_{f_{\text{min}}(N)}^{f} df v_+^{-1}(f/\nu_{+,\text{u}}) \tag{8.35}$$

with $\nu_+(f)$ following eq. (8.17). This condition is equivalent to eq. (8.32) with $f = f_{\text{max}}$. We calculate $T(f)$ for the three characteristic mean-field forces f_{c}, f_{max}, and $F_{s,N}$ and compare them to growth durations T_+ measured in simulations. Results are shown in Figs. 8.14 and 8.15 for $N = 5$ and $N = 10$. We find good agreement between improved mean-field results and stochastic simulations. In both cases $T(f_{\text{max}})$ and $T(F_{s,N})$ are within the range of the measured average duration of growth, while $T(f_{\text{c}})$ exceeds measured values of T_+ considerably.

8.2.6 Semi-stochastic approach

In the previous sections, we discussed MT bundle dynamics in the presence of rescue events. For a soft barrier, we find oscillations of the polymerization force around its mean value. In the steady state the MT bundle alternates between phases of collective growth and shrinkage, characterised by the number n_+ of simultaneously pushing MT . In a phase of collective growth we have a stable population $n_+ > 1$ of MTs pushing against the elastic barrier, while in a state of collective shrinkage we have $n_+ \approx 0$. Based on a dynamical mean field theory we discussed the steady-state dynamics in terms of the average force $\langle F \rangle$ and the average number $\langle n_+ \rangle$ of pushing MTs (see Sec. 8.2.3 and 8.2.5). Within the mean-field theory we assume a fast n_+-dynamics compared to a slow F-dynamics, so that n_+ takes its average steady-state value for a fixed (or slow varying) average force $\langle F \rangle$ (see 8.2.5). In addition to the assumption of different timescales of the n_+- and F-dynamics, we employ several further approximations to establish the mean field theory. In a first step we use $\langle g_{n_+}(F/n_+) \rangle \approx g_{n_+}(\langle F/n_+ \rangle)$ and $\langle r_{n_+}(F/n_+, n_+) \rangle \approx r_{n_+}(\langle F/n_+ \rangle, \langle n_+ \rangle)$ [see

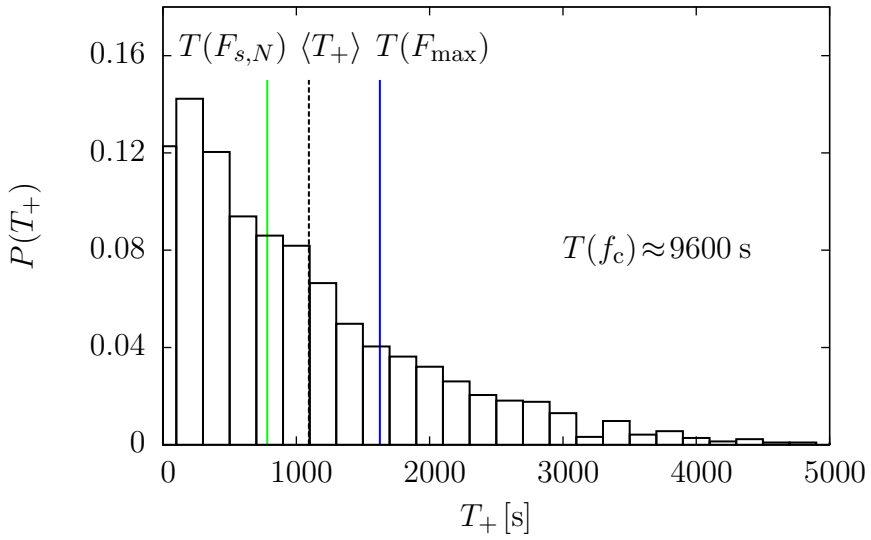

Figure 8.14: Probability $P(T_+)$ to find a phase of collective growth with length T_+, measured in simulations (see Sec. 7.1.2) for $N = 5$, $\omega_{\mathrm{on}} = 70\,\mathrm{s}^{-1}$ and $\omega_{\mathrm{r}} = 0.05\,\mathrm{s}^{-1}$. Vertical colored lines: $T(F)$ calculated via eq. (8.32) for $F_{\max}$ (blue line) and $F_{s,N}$ (green line). Dashed black line: Average duration of growth $\langle T_+ \rangle$ measured in simulations.

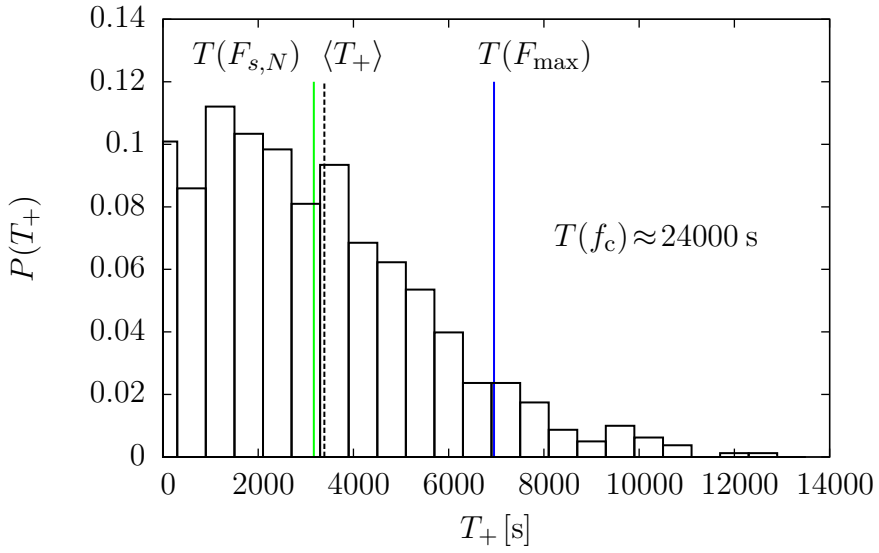

Figure 8.15: Probability $P(T_+)$ to find a phase of collective growth with length T_+, measured in simulations (see Sec. 7.1.2) for $N = 10$, $\omega_{\mathrm{on}} = 70\,\mathrm{s}^{-1}$ and $\omega_{\mathrm{r}} = 0.05\,\mathrm{s}^{-1}$. Vertical lines: $T(F)$ calculated via eq. (8.32) for $F_{\max}$ (blue line) and $F_{s,N}$ (green line). Dashed black line: Average duration of growth $\langle T_+ \rangle$ measured in simulations.

eq. (8.8)], and later $\langle F/n_+\rangle \approx \langle F\rangle\langle 1/n_+\rangle$ and $\langle 1/n_+\rangle \approx 1/\langle n_+\rangle$ [see. eq. (8.8) and eqs. (8.11) and (8.12)]. These approximations provide the essential elements $\langle n_+\rangle$ and $\langle F\rangle$ of the mean-field theory. However, the approximations are a priori not justified, since the underlying OPDF which determines the averages, is not known. In the following we present a semi-stochastic approach to the microscopic dynamics of the n_+ leading MTs in phases of collective growth and investigate the validity of the mean-field approximations, bases on the semi-stochastic n_+-dynamics.

The stochastic dynamics of the n_+ leading MTs is determined by the probability $p_{n_+}(t)$ to find n_+ leading MTs at time t. In order to calculate the probability $p_{n_+}(t)$ to find n_+ leading MTs for a given set of parameters, we assume a fast n_+-dynamics and treat F as a free tunable parameter. Again, this is a crucial approximation to the coupled n_+- and F-dynamics, but trajectories from simulations indicate, that, shortly after collective rescues, n_+ reaches its steady-state value, while F increases only slowly over much longer times scales (see Figs. 8.3 and 8.3). In addition, in Sec. 8.2.3 we find, that the macroscopic timescales of the $\langle n_+\rangle$- and $\langle F\rangle$-dynamics differ by a factor of 10, corresponding to a ten fold faster $\langle n_+\rangle$-dynamics compared to the $\langle F\rangle$-dynamics [see eqs. (8.13) and (8.14)].

The stochastic time evolution of the $n_+ \equiv n_+(F)$ with forward rates $g_{n_+} \equiv g_{n_+}(F, n_+)$ and backward rates $r_{n_+} \equiv r_{n_+}(F, n_+)$, given by eqs. (8.30), is described by a linear, one-step master equation for the probability $p_{n_+}(t, F)$ to find n_+ MTs at time t and for a fixed force F on the discrete state space $n_+ \in [0, N]$,

$$\partial_t p_{n_+}(t) = r_{n_++1}\, p_{n_++1}(t) + g_{n_+-1}\, p_{n_+-1}(t) - (r_{n_+} + g_{n_+})\, p_{n_+}(t), \tag{8.36}$$

with $n_+ = 0, 1, \ldots N$ and reflecting boundaries at $n_+ = 0$ and $n_+ = N$ [62, 63]. At the boundaries $n_+ = 0$ and $n_+ = N$ we have to adjust the forward and backward rate. For $n_+ = 0$, we set $g_0 \equiv \omega_r N$ and $r_0 \equiv 0$, corresponding to all MTs being in a collective state of shrinkage. At $n_+ = N$, we set $g_N \equiv 0$ and $r_N \equiv \omega_c(F/N)N$, corresponding to all MTs being in a collective state of growth.

In the steady state eq. (8.36) is solved with reflecting boundary at $n_+ = 0$ and we calculate the probability $p_{n_+} \equiv p_{n_+}(F)$ to find n_+ leading MT in the steady state explicitly [62],

$$p_{n_+} = \frac{g_{n_+-1}\, g_{n_+-2} \cdots g_1\, g_0}{r_{n_+}\, r_{n_+-1} \cdots r_2\, r_1} p_0 \tag{8.37}$$

with p_0 fixed by the normalization condition

$$p_0 = \left[1 + \sum_{n_+=1}^{N} \frac{g_0\, g_1 \cdots g_{n_+-1}}{r_1\, r_2 \cdots r_{n_+}}\right]^{-1}. \tag{8.38}$$

In Figs. 8.16 and 8.17, the steady-state probability p_{n_+} calculated from eqs. (8.37) and (8.38), is depicted for $N = 5$ and $N = 10$ and different values of the dimensionless force

F/F_0. Here we use the catastrophe model by Flyvbjerg *et al.* with $F_0 \simeq 7$ pN. For forces $F/F_0 < F_{s,N}/F_0$ smaller than the time averaged ensemble force $F_{s,N}$, p_{n_+} assumes a broad, Gaussian-shaped distribution, centered on an average $\langle n_+ \rangle > 0$ and $p_0 \approx 0$, corresponding to a stable population of leading MTs and, therefore, to phase of stable collective growth [see Fig. 8.16(a) and Fig. 8.17(a)]. We find such small forces, which satisfy $F/F_0 < F_{s,N}/F_0$, shortly after collective rescue events. At $F/F_0 \approx F_{s,N}/F_0$, p_{n_+} still assumes a broad, Gaussian-shaped distribution, but with a non-vanishing probability $p_0 > 0$. With increasing force, probability weight is shifted to smaller values of n_+. However, a stable population of leading MTs is maintained. If the force is increased to values $F/F_0 > F_{s,N}/F_0$ we find a sudden change in the probability distribution p_{n_+}. Most of the probability weight is now centered at $n_+ = 0$ and $p_0 \gg p_{n_+}\ \forall n_+ > 0$, so that $p_0 \approx 1$ [see Fig. 8.16(d) and Fig. 8.17(d)]. No stable population with $n_+ > 0$ is maintained, corresponding to a collective catastrophe. By tuning F, we can drive p_{n_+} from a broad, Gaussian-shaped distribution (small forces) to a strongly localized distribution (large forces), with most of the probability weight centered at $n_+ = 0$. This transition in the probability distribution for the n_+ leading MTs can be interpreted as the transition from a phase of collective growth to a phase of collective shrinkage, as observed in full stochastic simulations (see Figs. 8.3 and 8.3). Shortly after a collective rescue, we find small forces and p_{n_+} is Gaussian shaped. The force F is slowly increased by the polymerizing MTs and if a force $F > F_{s,N}$ is reached, p_{n_+} is reduced to $p_0 \approx 1$ and a collective catastrophe is initiated. In a state of collective shrinkage the force is decreased until the collective rescue force $F_{\min} \ll F_{s,N}$ is reached. The ensemble enters a state of collective growth, p_{n_+} again assumes a Gaussian shape, centered at $\langle n_+ > 1 \rangle$ and the cycle is closed. The semi-stochastic approach to the n_+-dynamics reproduces collective oscillations in the polymerization force qualitatively.

We want to stress out, that the transition of the steady-state probability distribution p_{n_+}, from a Gaussian-shaped form to a strong localized form at $n_+ = 0$ with increasing force, resembles the transition of a single MT growing against a constant force, from the regime of unbounded into the regime of bounded growth with increasing force (see. Sec. 4.2). For small forces and in the regime of unbounded growth, the probability $P(x,t)$ to find a MT with length x at time t is Gaussian shaped, while for large forces the MT enters the regime of bounded growth and $P(x)$ assumes an exponentially decaying form, with most of the probability weight localized at small MT length. Both, the shape of probability distributions and their transition with increasing force, are also found in the steady-state probability p_{n_+} given by eqs. (8.37) and (8.38). In Sec. 4.3 we found that, for a single MT growing against an elastic obstacle, the average dimensionless force $\langle \eta \rangle$ in the steady state approximately equals the critical dimensionless force η_c, which provides the transition from unbounded to bounded growth. For a single MT, growth under a constant force and growth against an elastic obstacle are therefore connected via $\eta_c \sim \langle \eta \rangle$.

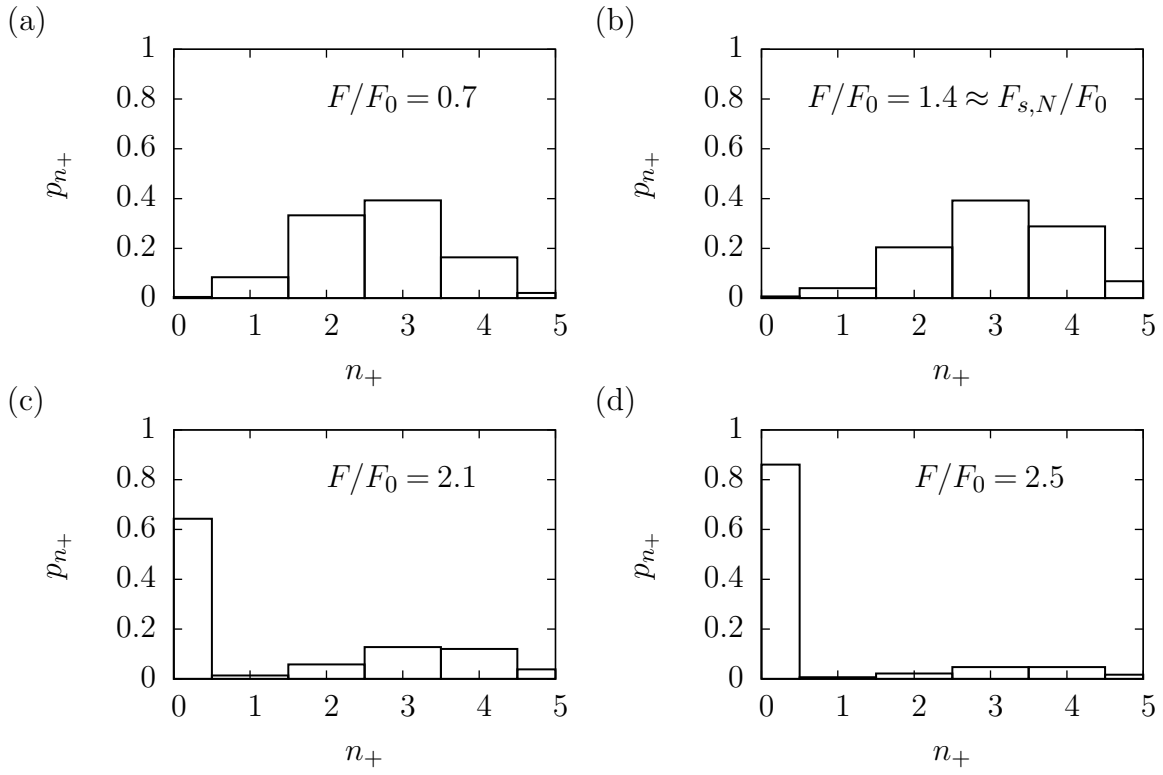

Figure 8.16: Steady-state probability p_{n_+} to find n_+ leading MTs for $N = 5$, $\omega_{\text{on}} = 70\,\text{s}^{-1}$, $\omega_{\text{r}} = 0.05\,\text{s}^{-1}$ and different values of F/F_0. (a): $F/F_0 = 0.7$. (b): $F/F_0 = 1.4$. (c): $F/F_0 = 2.1$. (d): $F/F_0 = 2.5$. We use the catastrophe model by Flyvbjerg *et al.* with $F_0 \simeq 7\,\text{pN}$.

Based on the results of the semi-stochastic approach, we suspect a similar connection of growth under constant force and growth against an elastic obstacle for MT ensembles with $N > 1$. However, a further investigation of the analogy of the dynamics of single MTs and MT ensembles needs much more effort and a deeper understanding of the underlying stochastic processes. This is beyond the scope of this thesis and had to be postponed.

We now want to address the question, if the semi-stochastic approach also reproduces results from full stochastic simulations quantitatively. In the steady state, we measure the probability $P(n_+)$ to find n_+ leading MT in a phase of collective growth. In Figs. 8.18 and 8.19 we compared $P(n_+)$ with the steady-state probability p_{n_+} from eqs. (8.37) and (8.38) with $F = F_{s,N}$. For $N = 5$ results from simulations agree well with results obtained from eqs. (8.37) and (8.38). Both probability distributions show similar shapes and yield nearly the same average number $\langle n_+ \rangle$ of leading MTs. However, there are small differences in the absolute values of the probability distributions. The steady-state probability p_{n_+} exhibits a non-vanishing part for $n_+ = 0$. The probability $P(0)$ can not be measured in simulations, since $n_+ = 0$ determines the begin of a collective phase of shrinkage and is , therefore, not part of a collective phase of growth. For $N = 10$ probability distributions are again similar shaped, but p_{n_+} is slightly shifted to higher values of n_+ compared to results from simulations (see Fig. 8.19) and we find $P(n_+) \approx p_{n_+ + 0.5}$. The shift to larger

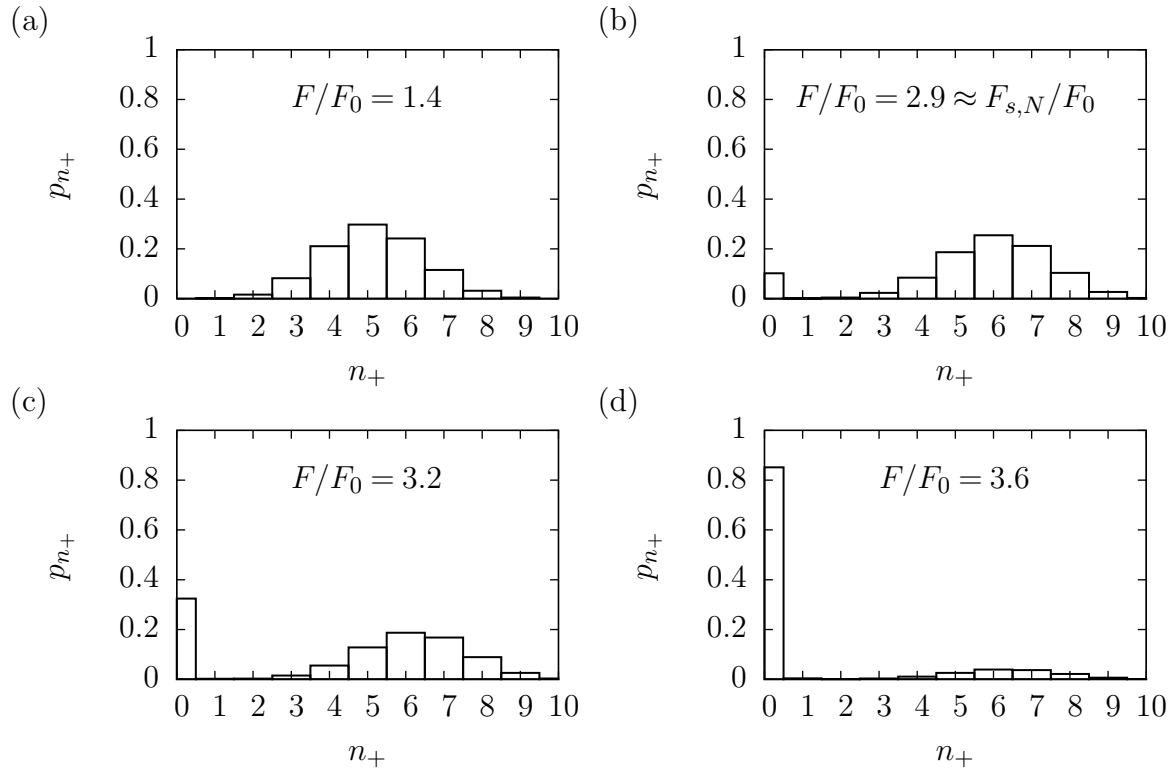

Figure 8.17: Steady-state probability p_{n_+} to find n_+ leading MTs for $N = 10$, $\omega_{\text{on}} = 70\,\text{s}^{-1}$, $\omega_{\text{r}} = 0.05\,\text{s}^{-1}$ and different values of F/F_0. (a): $F/F_0 = 1.4$. (b): $F/F_0 = 2.9$. (c): $F/F_0 = 3.2$. (d): $F/F_0 = 3.6$. We use the catastrophe model by Flyvbjerg *et al.* with $F_0 \simeq 7\,\text{pN}$.

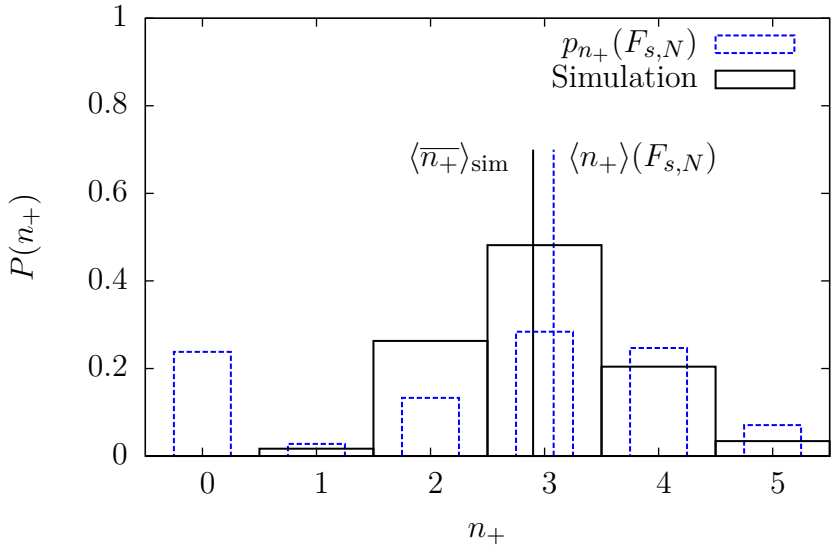

Figure 8.18: Probability $P(n_+)$ to find n_+ leading MTs in a collective state of growth, measured in simulations, for $N = 5$, $\omega_{\mathrm{on}} = 50\,\mathrm{s}^{-1}$ and $\omega_{\mathrm{r}} = 0.05\,\mathrm{s}^{-1}$. Solid boxes: $P(n_+)$ from simulations. Dashed boxes: Steady-state probability $p_{n_+}(F_{s,N})$ from eqs. (8.37) and (8.38) with $F = F_{s,N}$. For reasons of clarity we reduce the bin width from one to one-half. Solid vertical line: $\langle\overline{n_+}\rangle$ measured in simulations. Dashed vertical line: $\langle n_+\rangle = \sum_0^N n_+ p_{n_+}(F_{s,N})$.

values of n_+ can also be seen in the average number $\langle n_+\rangle$ of leading MTs. Nevertheless both distributions exhibit a large overlap and possess similar characteristics.

It is clearly visible, that the semi-stochastic approach to the n_+-dynamics reproduces results from simulations not only qualitatively but also quantitatively. Based on the steady-state probability distribution p_{n_+} from eqs. (8.37) and (8.38), we now want to investigate the quality and limits of mean-field approximations, such as $\langle\omega_{\mathrm{c}}(F/n_+)\rangle \approx \omega_{\mathrm{c}}(\langle F/n_+\rangle)$ or $\langle(F/n_+)\rangle \approx \langle F\rangle/\langle n_+\rangle$ (see Sec. 8.2.2).

In a first step we construct, from the microscopic probability distribution p_{n_+} [eqs. (8.37) and (8.38)], a macroscopic equation of motion for the number n_+ of leading MTs and find [62]

$$\frac{d}{dt}\langle n_+\rangle = \langle g_{n+}\rangle - \langle r_{n+}\rangle = \langle \tau^{-1}(F/n_+)\,(N-n_+)\rangle - \langle \omega_{\mathrm{c}}(F/n_+)n_+\rangle, \tag{8.39}$$

with

$$\langle u(n_+)\rangle \equiv \sum_{n_+=0}^{N} p_{n_+} u(n_+). \tag{8.40}$$

and some function $u(n_+)$. The steady-state solution of eq. (8.39) is given by:

$$\langle \tau^{-1}(F/n_+)\,(N-n_+)\rangle = \langle \omega_{\mathrm{c}}(F/n_+)n_+\rangle. \tag{8.41}$$

Equation (8.39) is equivalent to eq. (8.8) *before* mean-field approximations. The same applies to eq. (8.41) and eq. (8.16). It is clearly visible, both equations differ by the mean-

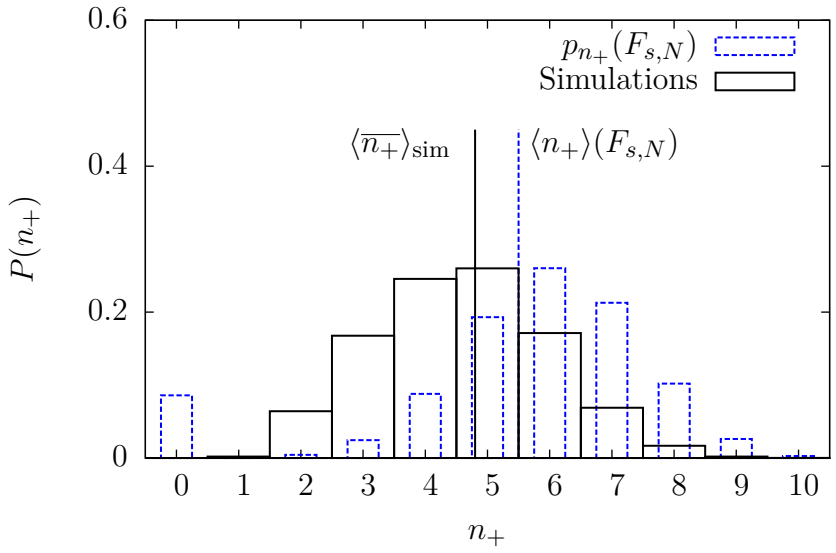

Figure 8.19: Probability $P(n_+)$ to find n_+ leading MTs in a collective state of growth, measured in simulations, for $N = 10$, $\omega_{\rm on} = 50\,{\rm s}^{-1}$ and $\omega_{\rm r} = 0.05\,{\rm s}^{-1}$. Solid boxes: $P(n_+)$ from simulations. Dashed boxes: Steady-state probability $p_{n_+}(F_{s,N})$ from eqs. (8.37) and (8.38) with $F = F_{s,N}$. For reasons of clarity we reduce the bin width from one to one-half. Solid vertical line: $\langle\overline{n_+}\rangle$ measured in simulations. Dashed vertical line: $\langle n_+\rangle$ calculated from p_{n_+} with $F = F_{s,N}$.

field approximations, where global averages are replaced by local averages, neglecting all correlations of higher order.

We start the analysis with $\langle r_{n_+}\rangle = \langle\omega_{\rm c}(F/n_+)n_+\rangle$ and perform the following sequence of successive mean-field approximations:

$$\langle\omega_{\rm c}(F/n_+)n_+\rangle \to \langle\omega_{\rm c}(F/n_+)\rangle\langle n_+\rangle \to \omega_{\rm c}(F\langle 1/n_+\rangle)\langle n_+\rangle \to \omega_{\rm c}(F/\langle n_+\rangle)\rangle\langle n_+\rangle. \qquad (8.42)$$

In each approximation step, the different averages are calculated via eq. (8.40) as a function of the dimensionless force F/F_0 with $F_0 \simeq 7{\rm pN}$ and $N = 10$, $\omega_{\rm on} = 70\,{\rm s}^{-1}$ and $\omega_{\rm r} = 0.05\,{\rm s}^{-1}$. Results are depicted in Fig. 8.20.

For forces up to $F/F_0 \approx 2$ there is no visible difference between all approximation steps. The average backward rate $r_{n_+} = \langle\omega_{\rm c}(F/n_+)n_+\rangle$ increases for forces $F/F_0 > 2$ and takes a constant value for $F/F_0 \approx 4$, corresponding to $v_+ \approx 0$ and $n_+ \approx 0$. The approximation steps $\omega_{\rm c}(\langle F/n_+\rangle)\langle n_+\rangle$ and $\omega_{\rm c}(F/\langle n_+\rangle)\rangle\langle n_+\rangle$ also show a characteristic increase with increasing force, but exhibit a divergence at $n_+ \approx 0$. This divergence is caused by vanishing n_+ and an exponential increase of $\omega_{\rm c}(F/n_+)$ for large forces (see Fig. 8.22). Both approximation steps differ also qualitatively. However, the semi-stochastic average backward rate $\langle\omega_{\rm c}(F/n_+)n_+\rangle$ and the final mean-field approximation result $\omega_{\rm c}(F/\langle n_+\rangle)\langle n_+\rangle$, which is a basic part of the dynamical mean-field theory used in Sec. 8.2.2 and Sec. 8.2.3, are nearly identical for small F/F_0 and exhibit a characteristic increase for large values of F/F_0. In contrast to the semi-stochastic results, the approximation step $r_{n_+} \approx \omega_{\rm c}(F\langle 1/n_+\rangle)\langle n_+\rangle$

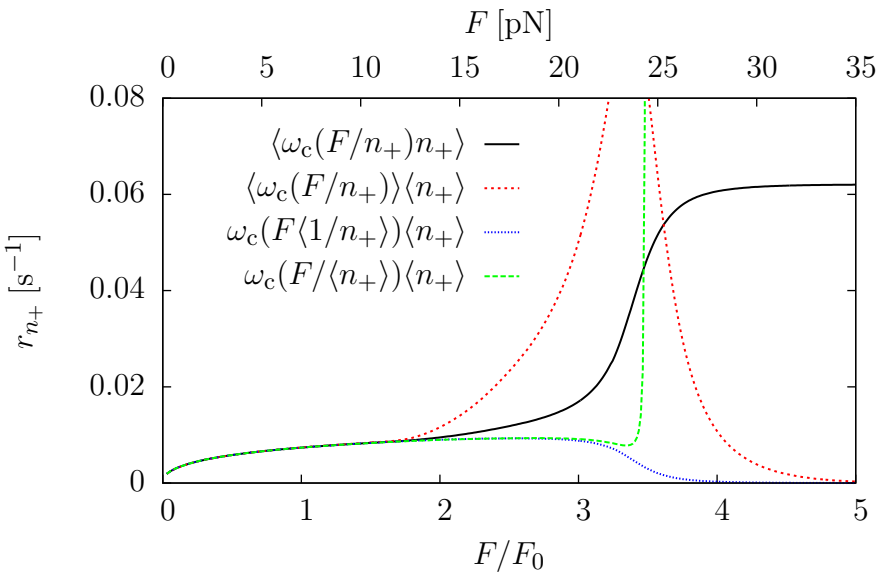

Figure 8.20: Backward rate $r_{n_+} = \langle\omega_c(F/n_+)n_+\rangle$ as a function of F/F_0 (bottom x-axis) and F (top x-axis) for $N = 10$, $\omega_{on} = 70\,s^{-1}$ and $\omega_r = 0.05\,s^{-1}$. Solid line: Semi-stochastic results for $\langle r_{n_+}\rangle = \langle\omega_c(F/n_+)n_+\rangle$. Dashed and dotted lines: Different types of mean-field approximations of $\langle r_{n_+}\rangle$.

does not increase with increasing force, but decreases and approaches zero for $F/F_0 \approx 4$. For large forces $\langle 1/n_+\rangle$ remains finite, while $\langle n_+\rangle \approx 0$.

We now investigate the average forward rate $g_{n_+} = \langle\tau^{-1}(F/n_+)(N - n_+)\rangle$, in the same way as in the case of the average backward rate. The following sequence of successive mean-field approximations is performed:

$$\begin{aligned}&\langle\tau^{-1}(F/n_+)(N-n_+)\rangle \to \langle\tau^{-1}(F/n_+)\rangle(N-\langle n_+\rangle)\rangle \to \\ &\tau^{-1}(F\langle 1/n_+\rangle)(N-\langle n_+\rangle) \to \tau^{-1}(F/\langle n_+\rangle)(N-\langle n_+\rangle).\end{aligned} \tag{8.43}$$

Results for $N = 10$, $\omega_{on} = 70\,s^{-1}$ and $\omega_r = 0.05\,s^{-1}$ are shown in Fig. 8.21.

We find only small differences between the semi-stochastic result $\langle g_{n_+}\rangle$ and all mean-field approximation steps for forces $F/F_0 \lesssim 2$. With increasing force mean-field approximations and semi-stochastic results begin to differ. While the semi-stochastic result $\langle g_{n_+}\rangle$ and the approximation step $\langle g_{n_+}\rangle \approx \tau^{-1}(F\langle 1/n_+\rangle)(N - \langle n_+\rangle)$ decrease and approach zero for forces $F/F_0 \gtrsim 3$, the approximation step $\langle\tau^{-1}(F/n_+)\rangle(N - \langle n_+\rangle)\rangle$ and the final mean-field approximation, used in Sec. 8.2.2 and Sec. 8.2.3, diverge at forces $F/F_0 \gtrsim 3$. The average forward rate $\langle g_{n_+}\rangle$ from semi-stochastic calculations and the final mean-field approximation $\langle g_{n_+}\rangle \approx \tau^{-1}(F/\langle n_+\rangle)(N - \langle n_+\rangle)$ do not exhibit the same characteristic behavior for large forces. This is in contrast to the average backward rate $\langle r_{n_+}\rangle$.

For forces $F/F_0 \lesssim 2$, the average forward rate $\langle g_{n_+}\rangle$ and the average backward rate $\langle r_{n_+}\rangle$ equal each other qualitatively and quantitatively , since both rates are connected via the

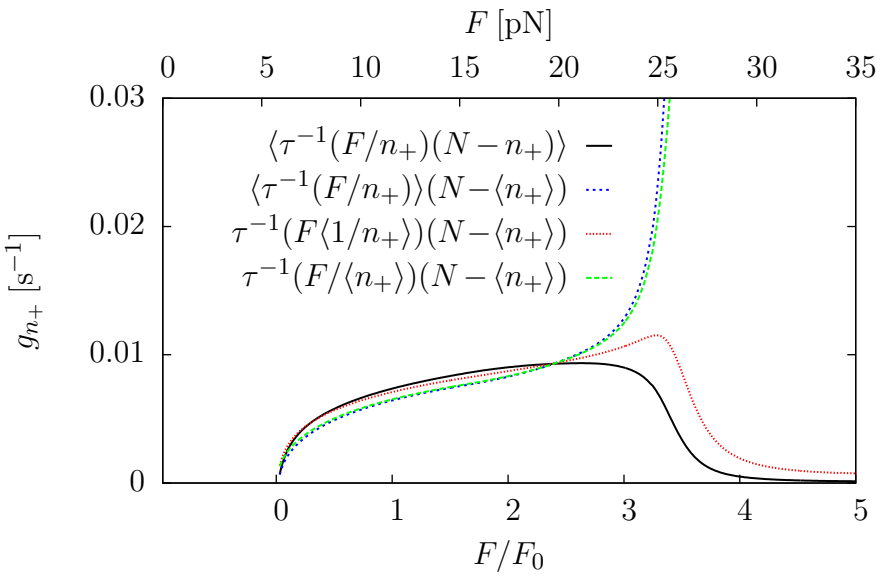

Figure 8.21: Forward rate $\langle g_{n_+}\rangle = \langle\tau^{-1}(F/n_+)(N-n_+)\rangle$ as a function of F/F_0 (bottom x-axis) and F (top x-axis) for $N = 10$, $\omega_{\text{on}} = 70\,\text{s}^{-1}$ and $\omega_{\text{r}} = 0.05\,\text{s}^{-1}$. Solid line: Semi-stochastic results for $\langle g_{n_+}\rangle$. Dashed and dotted lines: Different types of mean-field approximations of $\langle g_{n_+}\rangle$.

steady-state solution [eq. (8.41)] of eq. (8.39), but at larger force F/F_0 both rates show different behavior. The average backward rate $\langle r_{n_+}\rangle$ increases for forces $F/F_0 > 2$, while $\langle g_{n_+}\rangle$ decreases and tends to zero. The steady-state condition is no longer fulfilled and the ensemble undergoes a collective catastrophe, as expected for large forces.

At larger forces $F/F_0 \gtrsim 2$ results for $\langle r_{n_+}\rangle$ and $\langle g_{n_+}\rangle$, obtained with the semi-stochastic approach and results from the final mean-field approximation step, exhibit major differences (see Figs. 8.20 and 8.21). However, in Sec. 8.2.3 we found, that characteristic forces, as the critical force F_{c}, describe the dynamics of the MT bundle only qualitatively, and results for the average polymerization force $F_{s,N}$ obtained from pure mean-field calculations exceed results from stochastic simulations (see Fig. 8.6). In order to achieve quantitative agreement we introduced an improved mean-field theory (see Sec. 8.2.5). The essential part of the improved mean-field theory, is the calculation of the maximal ensemble force F_{max} from the MFPT starting at the upper stable branch of the nullcline with $\langle n_{+,u}\rangle > 0$ to an absorbing state with $n_+ = 0$. Results from the improved mean-field theory agree well with results from simulation and the average polymerization force $F_{s,N}$ is much smaller, compared to $F_{s,N}$ from the pure mean-field theory (see Fig. 8.6). For $\omega_{\text{on}} = 70\,\text{s}^{-1}$ and $\omega_{\text{r}} = 0.05\,\text{s}^{-1}$, the dimensionless maximal ensemble force is of the order $F_{\text{max}}/F_0 \approx 4$, which is in the range of forces, where $\langle r_{n_+}\rangle$ and $\langle g_{n_+}\rangle$, calculated within the semi-stochastic approach, and the final mean-field approximations do significantly differ (see Figs. 8.20 and 8.21). To test the validity and limits of the improved mean field theory, we compute the average fraction $\nu_+(f)_{\text{stoch}}$ of pushing MTs via eq. (8.40) and compare it to results from the improved mean-field theory. Results are depicted in Fig. 8.22.

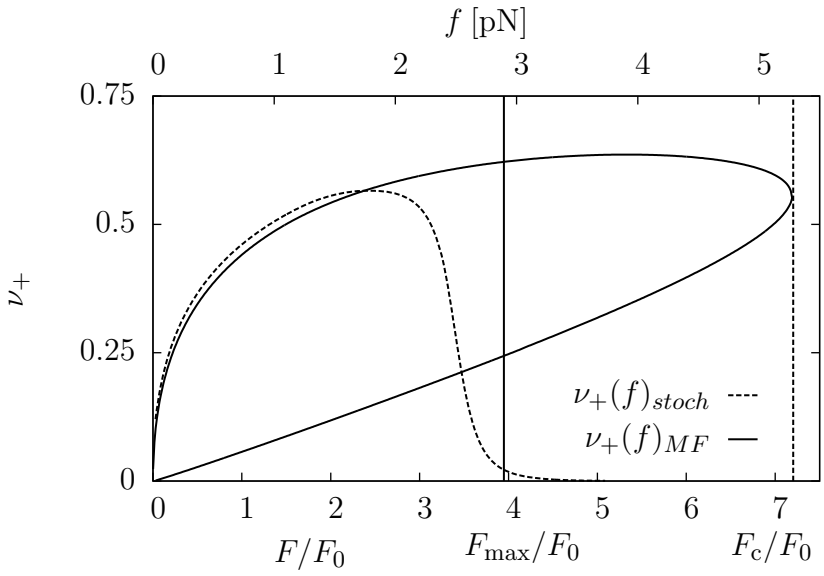

Figure 8.22: Average fraction ν_+ of pushing MTs as a function of F/F_0 (bottom axis) and $f = F/N$ (top axis) for $\omega_{on} = 70\,s^{-1}$ and $\omega_r = 0.05\,s^{-1}$. Solid line: $\nu_+(f)_{MF}$ as solution of mean field equation (8.16). Dashed line: $\nu_+(f)_{stoch}$ from semi-stochastic calculations. Solid vertical line: Maximal ensemble force F_{max} from improved mean-field calculations (see Sec. 8.2.5). Dashed vertical line: Critical mean-field force F_c from pure mean-field calculations (see Sec. 8.2.3)

With increasing force $\nu_+(F/F_0)_{stoch}$ follows the stable upper branch of the nullcline of eq. (8.16). At $F/F_0 \approx 2$, $\nu_+(F/F_0)_{stoch}$ starts to decrease and rapidly approaches zero for forces $F/F_0 \approx 4$, whereas the stable upper branch yields $\nu_+(F/F_0)_{MF} > 0$ until the critical force F_c/F_0 is reached. The difference of $\nu_+(F)_{stoch}$ and $\nu_+(F/F_0)_{MF}$ is in accordance with results from the previous paragraph. The semi-stochastic approach and the dynamic mean-field theory, based on the final approximation step, are in good agreement for forces $F/F_0 \lesssim 2$ only and differ significantly for larger forces. Within the improved mean-field theory we calculate the MFPT as a function of the force F, starting on the stable upper branch of the nullcline $\nu_{+,u}(F)$. For $F/F_0 > 2$ the starting point of the MFPT is not confirmed by the semi-stochastic approach. However, the final absorbing state of the MFPT as a function of force, $\nu_+(F) = 0$, and $\nu_+(F)_{stoc} = 0$ are equivalent to each other, since the characteristic behavior of the MFPT as a function of the force F is determined by the underlying probability distribution $p_{n_+}(t, F)$, with $p_{n+}(t, F)$ as solution of eq. (8.36) (for a detailed description see [62]). The MFPT final absorbing state $\nu_+(F) = 0$ and $\nu_+(F)_{stoch} = 0$ are, therefore, fixed by the same characteristic force F_{max}. Since F_{max} is not only determined by the MFPT but also from the condition of stable growth along the upper branch of the nullcline (see Sec. 8.2.5), which is not verified by the semi-stochastic approach for large forces, we find small deviations of $\nu_+(F_{max}) = 0$ and $\nu_+(F)_{stoc} = 0$.

To conclude: Semi-stochastic calculations and mean-field approximations agree well for both rates and forces $F/F_0 \lesssim 2$. Results derived from the pure dynamical mean-field

theory, which is based on the final approximation step, are in agreement with semi-stochastic calculations (see Fig. 8.22) and the mean-field approximation remain valid for forces up to $F/F_0 \lesssim 2$. At larger forces $F/F_0 \gtrsim 2$, semi-stochastic and mean-field approximation exhibit major differences. Results for the average polymerization force $F_{s,N}$, obtained from the pure dynamical mean field theory are only valid in the context of the mean-field theory and are not confirmed by semi-stochastic calculations. Also the improved mean field theory is not fully confirmed by the semi-stochastic approach for forces $F/F_0 > 2$. However, results for the maximal ensemble force $F_{\max}$ and thus for the average polymerization force $F_{s,N}$, are in good agreement with results from the semi-stochastic approach.

Chapter 9

Final conclusion [1]

We extend the single MT model to an ensemble of N MTs, growing against an elastic barrier (see Fig. 6.1).

In cooperative force generation by an ensemble of N MTs, the interplay between force-sharing and MT dynamic instability gives rise to a complex dynamics, which can be described in terms of collective catastrophe and rescue events.

We developed a dynamical mean-field theory [see eqs. (8.1) and (8.12)] which gives a quantitative description of the cooperative MT dynamics in terms of two parameters, the mean force $\langle F \rangle$ and the mean number of pushing MTs $\langle n_+ \rangle$, in both the absence and presence of rescue events.

The dynamical mean-field theory is validated by stochastic simulations of the MT ensemble dynamics.

In the absence of rescue events, the maximal polymerization force before collective catastrophes grows linearly with N for small N or a stiff elastic barrier, in agreement with existing experimental data [53], whereas it crosses over to a logarithmic dependence for larger N or soft elastic barrier [see eq. (8.5) and Fig. 8.1]. This crossover should be accessible in experiments by varying the stiffness of optical traps. The maximal polymerization force increases approximately linear in the tubulin on-rate [see eqs. (8.4) and (8.5)]. Again this should be accessible in experiments by varying the tubulin concentration.

In the presence of rescue events and for a *soft* elastic barrier, the dynamics becomes strongly modified: Collective catastrophes and rescues lead to an oscillatory stable limit cycle dynamics far from a Hopf bifurcation. These oscillations should be observable *in vitro* in experiments such as in Ref. [53] if the MT lengths are sufficient to observe rescue events and if the stiffness of optical traps is reduced. Moreover, *in vivo* the behavior of polarized MT ensembles can be explored, as has been shown in Ref. [92], and our model predicts synchronized growth and shrinkage in oscillations if a polarized MT ensemble is growing against an elastic barrier such as the cell cortex.

[1] Parts of the text have been published in reference [55] and is ©2012 American Physical Society. http://publish.aps.org/copyrightFAQ.html

In the presence of oscillations, we have quantified the maximal polymerization force $F_c = Nf_c$ in eq. (8.19) and the time-averaged polymerization force $F_{s,N}$ in eq. (8.22) based on the nullclines of the dynamics mean field theory. Both forces are *linear* in N (see Figs. 8.6), and the relevant force scale is the force scale F_0, above which the MT growth velocity decreases exponentially and the MT catastrophe rate increases exponentially. The time-averaged polymerization force strongly increases with increasing tubulin on-rate (and, thus, decreasing catastrophe rate) or increasing MT rescue rate (see Figs. 8.7).
Including stochastic fluctuations, which reduce the maximal polymerization force, we find a linear N dependence of forces for small MT numbers [see eq. (8.34)].
The linear N dependence of forces in the presence of rescue events is remarkable because we find an only logarithmic increase with N in the absence of rescue events for soft barriers (see Fig. 8.1).
Nevertheless, even the maximal polymerization force is significantly smaller than the N-fold single-MT stall force. This shows that MTs are not optimized with respect to force generation because of their dynamic instability, even if they cooperate in an ensemble. On the other hand, our analysis also shows that force generation in MT ensembles is very sensitive to changes of system parameters related to the dynamic instability of MTs. The combination of both results suggests that a MT ensemble is not efficient to generate high forces but that the dynamic instability in connection with the ensemble dynamics allows us to efficiently regulate force generation through several system parameters.
We show that our results are robustness against variations of the catastrophe model In terms of the relevant force scale F/F_0, the catastrophe models by Flyvbjerg *et al.* and Janson *et al.* yield similar results. The linear catastrophe model, lacking an exponentially increase for forces larger than F_0, does not exhibits a oscillatory limit cycle. We find a stable fixed point of the cooperative dynamics,
Finally we present a semi-stochastic approach to the dynamics of the n_+ leading MTs and investigate the limits of the dynamical mean field theory. For small forces, results obtained from the mean field theory are confirmed by semi-stochastic calculations, while for larger forces results exhibit major differences. In addition, we illustrate a possible connection of MT ensembles growing under constant force and growing against an elastic barrier.

Chapter 10

Outlook

We discuss some open issues, which can be addressed by the theoretical framework presented in this thesis:

- **Regulation by feedback mechanisms**
  Within a cell, MTs and regulating proteins form feedback loops. Recent work on the regulation of single MT growth dynamics by a positive feedback loop, revealed a complex interplay of single MT and protein dynamics [93, 94]. Simple feedback mechanisms can easily be incorporated into the MT ensemble model, to investigate their influence on the force generation by MT ensembles.

- **MT ensembles under constant force**
  Within this thesis, we discussed the polymerization dynamics of MT ensembles growing against an elastic obstacle. But, as in the case of a single MT, it is also possible to study MT ensemble dynamics under a constant force. Simulation results, not shown here, of MT ensemble growing under a constant force indicate two different growth regimes, resembling the regime of bounded and unbounded growth for a single MT. For small forces the average length of the MT ensemble increases linearly in time, whereas for large forces the average length approaches zero. There is a sharp transition between the two regimes. This transition can also be seen in the probability distributions p_{n_+} to find n_+ leading MTs, as discussed in Sec. 8.2.6. It should be possible, as in the case of a single MT, to find a critical force, which provides the transition between the two regimes. For a single MT we found that the critical force η_c approximately equals the average steady state force $\langle \eta \rangle$ for growth against an elastic obstacle (see Sec. 4.3.2). A similar connection may exist for MT ensembles growing under a constant force and growing against an elastic obstacle.

- **No force sharing in actin filaments**
  Recent optical trap experiments on the force generation of actin filaments showed that polymerizing bundles of parallelly arranged actin filaments do not share a

resiting force [51]. Existing polymerization models for parallel actin filaments do not address the force generation [26]. The MT ensemble model, presented in this thesis, can be modified in order to describe the polymerization dynamics of parallel actin filaments. Based on the modified model, the force generation of actin bundles can be investigated in a similar way, as the force generation of MT bundles.

- **Protofilament dynamics**
  The MT ensemble model can be modified to describe the dynamics of coupled protofilaments within a single MT. A single MT now acts as a single protofilament, which can either be in a state of growth or in a state of stall, resembling the state of shrinkage. In a state of growth, new GTP-tubulin monomers are incorporated into the tip of a single protofilament, whereas in a state of stall no GTP-tubulin monomers are attached. The growth of the protofilament is stalled and the entire protofilament consists of GDP-tubulin. Protofilaments can be coupled to neighboring filaments by lateral bonds, resembling the coupling of MTs via force-sharing. The number of lateral bonds can be increased by the addition of new GTP-tubulin monomers and decreased by hydrolysis. If a single protofilament switches into the state of stall, all lateral bonds are lost. If a critical amount of protofilaments is in the state of stall, too many lateral bonds are lost and the protofilament lattice is destabilized, corresponding to a collective catastrophe in the case of MT ensemble dynamics. The dynamics of the coupled protofilaments can than be analyzed in a similar way as the cooperative dynamics of MT ensembles.

Appendix A

Literature values for MT growth parameters and simulation parameters

Ref.	$v_+(0)$ [m/s]	ω_{on} [1/s]	v_- [m/s]	ω_r [1/s]
Drechsel [95]	$(0.7 \dots 2) \times 10^{-8}$	$(11 \dots 32)$	$\sim 1.8 \times 10^{-7}$	-
Gildersleeve [96]	$\sim 4.2 \times 10^{-8}$	~ 68	$\sim 4.2 \times 10^{-7}$	-
Walker [15]	$(4 \dots 8) \times 10^{-8}$	$(63 \dots 130)$	$\sim 5 \times 10^{-7}$	$(0.05 \dots 0.08)$(TUB)
Laan [53]	$\sim 4.2 \times 10^{-8}$	68.25	-	-
Janson [60]	$(3 \dots 4.3) \times 10^{-8}$	$(53 \dots 74)$	-	-
Pryer [16]	-	-	-	... 0.5 (TUB) ..0.15 (MAPS)
Dhamodharan [97]	-	-	-	... 0.07 (Cell) ... 0.085 (MAPS)
Nakao [98]	-	-	-	... 0.1 (TUB)
Shelden [99]	-	-	-	$(0.03 \dots 0.2)$ (Cell)

Table A.1: Literature values for parameters. TUB: *in vitro* results for tubulin solutions, Cell: *in vivo* results, MAPS: effect from MT associated proteins. Values for ω_{on} are estimated from measured growth velocities via $\omega_{\text{on}} \approx v_+(0)N/d$ neglecting $\omega_{\text{off}} = 6\,\text{s}^{-1}$ [60]. Here $N = 13$ denotes the number of protofilaments within a single MT.

Parameter	v_- [m/s] (see Table A.1)	ω_{off} [s^{-1}]	d [m]	r [$\text{m}^{-1}\text{s}^{-1}$]	v_h [m/s]	Δt [s]
Value	3×10^{-7}	6	0.6×10^{-9}	3.7×10^{6}	4.2×10^{-9}	0.1

Table A.2: Fixed parameter values for calculations and simulations.

Bibliography

[1] B. Alberts, A. Johnson, J. Lewis, M. Raff, K. Roberts, P. Walter. *Molecular Biology of the Cell.* Garland Science, New York (2008). 1, 1.1, 1.1, 1.2, 1.1, 1.1, 1.4, 1.1

[2] J. Howard. *Mechanics of Motor Proteins and the Cytoskeleton.* Sinauer Associates, Inc., Sunderland, Massachusetts (2001). 1, 1.1, 1.1, 1.1, 2.2, 2.2, 2.2

[3] J. Howard, A. A. Hyman. Dynamics and mechanics of the microtubule plus end. *Nature* **422**(6933), 753 (2003). doi:10.1038/nature01600.
URL http://www.ncbi.nlm.nih.gov/pubmed/12700769 1, 1.1

[4] L. A. Amos, T. S. Baker. The three-dimensional structure of tubulin protofilaments. *Nature* **279**(5714), 607 (1979). doi:10.1038/279607a0.
URL http://www.nature.com/nature/journal/v279/n5714/abs/279607a0.html 1.1

[5] E. Mandelkow, E. M. Mandelkow. Microtubular structure and tubulin polymerization. *Current Opinion in Cell Biology* **1**(1), 5 (1989). doi:10.1016/S0955-0674(89)80029-8. 1.1

[6] E. Nogales, S. G. Wolf, K. H. Downing. Structure of the $\alpha\beta$ tubulin dimer by electron crystallography. *Nature* **391**(6663), 199 (1998). doi:10.1038/34465.
URL http://www.nature.com/nature/journal/v391/n6663/full/391199a0.html 1.1

[7] V. VanBuren, D. J. Odde, L. Cassimeris. Estimates of lateral and longitudinal bond energies within the microtubule lattice. *Proceedings of the National Academy of Sciences of the United States of America* **99**(9), 6035 (2002). doi:10.1073/pnas.092504999.
URL http://www.pubmedcentral.nih.gov/articlerender.fcgi?artid=122897&tool=pmcentrez&rendertype=abstract 1.1, 1.1

[8] A. Grafmüller, E. G. Noya, G. A. Voth. Nucleotide-Dependent Lateral and Longitudinal Interactions in Microtubules. *Journal of Molecular Biology* **425**(12), 2232 (2013). doi:10.1016/j.jmb.2013.03.029.
URL http://www.ncbi.nlm.nih.gov/pubmed/23541590 1.1

[9] T. Mitchison, M. Kirschner. Dynamic instability of microtubule growth. *Nature* **312**(5991), 237 (1984). doi:10.1038/312237a0.
URL http://www.ncbi.nlm.nih.gov/pubmed/6504138 1.1, 1.1

[10] J. Luders, T. Stearns. Opinion - Microtubule-organizing centres: a re-evaluation. *Nature Reviews Molecular Cell Biology* **8**(2), 161 (2007). doi:10.1038/nrm2100.
URL http://www.nature.com/nrm/journal/v8/n2/full/nrm2100.html 1.1

[11] D. K. Fygenson, E. Braun, A. Libchaber. Phase diagram of microtubules. *Physical Review E* **50**(2), 1579 (1994). doi:10.1103/PhysRevE.50.1579.
URL http://pre.aps.org/abstract/PRE/v50/i2/p1579_1 1.1

[12] D. K. Fygenson, H. Flyvbjerg, K. Sneppen, A. Libchaber, S. Leibler. Spontaneous nucleation of microtubules. *Physical Review E* **51**(5), 5058 (1995). doi:10.1103/PhysRevE.51.5058.
URL http://pre.aps.org/abstract/PRE/v51/i5/p5058_1 1.1

[13] T. D. Pollard. Rate Constants for the Reaction of ATP-Actin and ADP-Actin with the End of Actin filaments. *The Journal of Cell Biology* **103**(6), 2747 (1986). doi:10.1083/jcb.103.6.2747.
URL http://jcb.rupress.org/content/103/6/2747 1.1

[14] H. P. Erickson, E. T. O'Brien. Microtubule dynamic instability and GTP hydrolysis. *Annual Review of Biophysics and Biomolecular Structure* **21**, 145 (1992). doi:10.1146/annurev.bb.21.060192.001045.
URL http://www.ncbi.nlm.nih.gov/pubmed/1525467 1.1, 1.5

[15] R. A. Walker, E. T. O'Brien, N. K. Pryer, M. F. Soboeiro, W. A. Voter, H. P. Erickson, E. D. Salmon. Dynamic instability of individual microtubules analyzed by video light microscopy: rate constants and transition frequencies. *The Journal of Cell Biology* **107**(4), 1437 (1988). doi:10.1083/jcb.107.4.1437.
URL http://www.ncbi.nlm.nih.gov/pubmed/3170635 1.1, 2.3, A

[16] N. K. Pryer, R. A. Walker, V. P. Skeen, B. D. Bourns, M. F. Soboeiro, E. D. Salmon. Brain microtubule-associated proteins modulate microtubule dynamic instability in vitro. Real-time observations using video microscopy. *Journal of Cell Science* **103**(4), 965 (1992).
URL http://www.ncbi.nlm.nih.gov/pubmed/1487507 1.1, A

[17] H. T. Schek, M. K. Gardner, J. Cheng, D. J. Odde, A. J. Hunt. Microtubule assembly dynamics at the nanoscale. *Current Biology* **17**(17), 1445 (2007). doi:10.1016/j.cub.2007.07.011.

URL http://www.pubmedcentral.nih.gov/articlerender.fcgi?artid=2094715&tool=pmcentrez&rendertype=abstract 1.1, 1.4, 1.9, 2.2, 4.1, 4.3, 4.3.1

[18] H. Flyvbjerg, T. E. Holy, S. Leibler. Microtubule dynamics: Caps, catastrophes, and coupled hydrolysis. *Physical Review E* **54**(5), 5538 (1996). doi: 10.1103/PhysRevE.54.5538.
URL http://www.ncbi.nlm.nih.gov/pubmed/9965740 1.1, 2.3, 2.3, 2.3, 4.2, 4.3.1, 8.2.4

[19] D. N. Drechsel, M. W. Kirschner. The minimum GTP cap required to stabilize microtubules. *Current Biology* **4**(12), 1053 (1994). doi:http://dx.doi.org/10.1016/S0960-9822(00)00243-8.
URL http://www.ncbi.nlm.nih.gov/pubmed/7704569 1.1

[20] H. Y. Kueh, T. J. Mitchison. Structural plasticity in actin and tubulin polymer dynamics. *Science* **325**(5943), 960 (2009). doi:10.1126/science.1168823.
URL http://www.pubmedcentral.nih.gov/articlerender.fcgi?artid=2864651&tool=pmcentrez&rendertype=abstract 1.1, 2.3

[21] G. Margolin, H. V. Goodson, M. S. Alber. Mean-field study of the role of lateral cracks in microtubule dynamics. *Physical Review E* **83**(4), 041905 (2011). doi:10.1103/PhysRevE.83.041905.
URL http://link.aps.org/doi/10.1103/PhysRevE.83.041905 1.1

[22] A. Akhmanova, M. Dogterom. Kinesins lead aging microtubules to catastrophe. *Cell* **147**(5), 966 (2011). doi:10.1016/j.cell.2011.11.011.
URL http://www.ncbi.nlm.nih.gov/pubmed/22118452 1.1, 1.1

[23] A. Dimitrov, M. Quesnoit, S. Moutel, I. Cantaloube, C. Poüs, F. Perez. Detection of GTP-tubulin conformation in vivo reveals a role for GTP remnants in microtubule rescues. *Science* **322**(5906), 1353 (2008). doi:10.1126/science.1165401.
URL http://www.ncbi.nlm.nih.gov/pubmed/18927356 1.1

[24] C. Tropini, E. A. Roth, M. Zanic, M. K. Gardner, J. Howard. Islands containing slowly hydrolyzable GTP analogs promote microtubule rescues. *PloS One* **7**(1), e30103 (2012). doi:10.1371/journal.pone.0030103.
URL http://www.pubmedcentral.nih.gov/articlerender.fcgi?artid=3260198&tool=pmcentrez&rendertype=abstract 1.1

[25] L. Cassimeris, N. K. Pryer, E. Salmon. Real-Time Observations of Microtubule Dynamic Instability in Living Cells. *The Journal of Cell Biology* **107**(6), 2223 (198). doi:10.1083/jcb.107.6.2223.
URL http://jcb.rupress.org/content/107/6/2223 1.5

[26] K. Tsekouras, D. Lacoste, K. Mallick, J. F. Joanny. Condensation of actin filaments pushing against a barrier. *New Journal of Physics* **13**(10), 103032 (2011). doi:10.1088/1367-2630/13/10/103032.
URL http://stacks.iop.org/1367-2630/13/i=10/a=103032?key=crossref.4e3dd120185e7373ff9a6810fea08277 1.1, 10

[27] X. Li, J. Kierfeld, R. Lipowsky. Actin Polymerization and Depolymerization Coupled to Cooperative Hydrolysis. *Physical Review Letters* **103**(4), 1 (2009). doi:10.1103/PhysRevLett.103.048102.
URL http://link.aps.org/doi/10.1103/PhysRevLett.103.048102 1.1, 2.3

[28] P. A. Curmi, S. S. L. Andersen, S. Lachkar, O. Gavet, E. Karsenti, M. Knossow, A. Sobel. The stathmin/tubulin interaction in vitro. *The Journal of Biological Chemistry* **272**(40), 25029 (1997). doi:10.1074/jbc.272.40.25029.
URL http://www.ncbi.nlm.nih.gov/pubmed/9312110 1.1, 2.1, 4.3.2.3

[29] M. K. Gardner, M. Zanic, C. Gell, V. Bormuth, J. Howard. Depolymerizing kinesins Kip3 and MCAK shape cellular microtubule architecture by differential control of catastrophe. *Cell* **147**(5), 1092 (2011). doi:10.1016/j.cell.2011.10.037.
URL http://www.ncbi.nlm.nih.gov/pubmed/22118464 1.1, 2.3

[30] P. T. Tran, L. Marsh, V. Doye, S. Inoué, F. Chang. A mechanism for nuclear positioning in fission yeast based on microtubule pushing. *The Journal of Cell Biology* **153**(2), 397 (2001). doi:10.1083/jcb.153.2.397.
URL http://www.pubmedcentral.nih.gov/articlerender.fcgi?artid=2169469&tool=pmcentrez&rendertype=abstract 1.2

[31] D. R. Drummond, R. A. Cross. Dynamics of interphase microtubules in Schizosaccharomyces pombe. *Current Biology* **10**(13), 766 (2000). doi:10.1016/S0960-9822(00)00570-4.
URL http://www.sciencedirect.com/science/article/pii/S0960982200005704 1.2

[32] R. R. Daga, K. G. Lee, S. Bratman, S. Salas-Pino, F. Chang. Self-organization of microtubule bundles in anucleate fission yeast cells. *Nature Cell Biology* **8**(10), 1108 (2006). doi:10.1038/ncb1480.
URL http://www.ncbi.nlm.nih.gov/pubmed/16998476 1.2

[33] M. E. Janson, R. Loughlin, I. Loïodice, F. Chuanhai, D. Brunner, F. J. Nédélec, P. T. Tran. Crosslinkers and Motors Organize Dynamic Microtubules to Form Stable Bipolar Arrays in Fission Yeast. *Cell* **128**(2), 357 (2007). doi:10.1016/j.cell.2006.12.030.
URL http://www.sciencedirect.com/science/article/pii/S0092867407000487 1.2

[34] R. R. Daga, A. Yonetani, F. Chang. Asymmetric microtubule pushing forces in nuclear centering. *Current Biology* **16**(15), 1544 (2006). doi:10.1016/j.cub.2006.06.026.
URL http://www.ncbi.nlm.nih.gov/pubmed/16890530 1.2, 4.1

[35] L. Sacconi, I. M. Tolić-Nørrelykke, C. Stringari, R. Antolini, F. S. Pavone. Optical micromanipulations inside yeast cells. *Applied Optics* **44**(11), 2001 (2005). doi:10.1364/AO.44.002001.
URL http://www.opticsinfobase.org/ao/abstract.cfm?uri=AO-44-11-2001 1.2

[36] C. Tischer, D. Brunner, M. Dogterom. Force- and kinesin-8-dependent effects in the spatial regulation of fission yeast microtubule dynamics. *Molecular Systems Biology* **5**(250), 250 (2009). doi:10.1038/msb.2009.5.
URL http://www.pubmedcentral.nih.gov/articlerender.fcgi?artid=2671921&tool=pmcentrez&rendertype=abstract 1.2

[37] D. Foethke, T. Makushok, D. Brunner, F. J. Nédélec. Force- and length-dependent catastrophe activities explain interphase microtubule organization in fission yeast. *Molecular Systems Biology* **5**(241), 241 (2009). doi:10.1038/msb.2008.76.
URL http://www.pubmedcentral.nih.gov/articlerender.fcgi?artid=2671915&tool=pmcentrez&rendertype=abstract 1.2, 1.7

[38] D. K. Fygenson, J. F. Marko, A. Libchaber. Mechanics of Microtubule-Based Membrane Extension. *Physical Review Letters* **79**(22), 4497 (1997). doi:10.1103/PhysRevLett.79.4497.
URL http://link.aps.org/doi/10.1103/PhysRevLett.79.4497 1.3, 1.8

[39] L. Dehmelt, F. M. Smart, R. S. Ozer, S. Halpain. The role of microtubule-associated protein 2c in the reorganization of microtubules and lamellipodia during neurite initiation. *The Journal of Neuroscience* **23**(29), 9479 (2003).
URL http://www.ncbi.nlm.nih.gov/pubmed/14573527 1.3

[40] K. Franze, J. Guck. The biophysics of neuronal growth. *Reports on Progress in Physics* **73**(9), 094601 (2010). doi:10.1088/0034-4885/73/9/094601.
URL http://stacks.iop.org/0034-4885/73/i=9/a=094601?key=crossref.1e6c2d7988b5dab945ccce0f5a6ef772 1.3

[41] J. R. Moffitt, Y. R. Chemla, S. B. Smith, C. Bustamante. Recent advances in optical tweezers. *Annual Review of Biochemistry* **77**, 205 (2008). doi:10.1146/annurev.biochem.77.043007.090225.
URL http://www.ncbi.nlm.nih.gov/pubmed/18307407 1.4

[42] K. C. Neuman, S. M. Block. Optical trapping. *The Review of Scientific Instruments* **75**(9), 2787 (2004). doi:10.1063/1.1785844.
URL http://www.pubmedcentral.nih.gov/articlerender.fcgi?artid=1523313&tool=pmcentrez&rendertype=abstract 1.4

[43] K. C. Neuman, A. Nagy. Single-molecule force spectroscopy: optical tweezers, magnetic tweezers and atomic force microscopy. *Nature Methods* **5**(6), 491 (2008). doi:10.1038/NMETH.1218.
URL http://www.nature.com/nmeth/journal/v5/n6/full/nmeth.1218.html 1.4

[44] T. T. Perkins. Optical traps for single molecule biophysics: a primer. *Laser & Phontonics Reviews* **3**(1-2), 203 (2009). doi:10.1002/lpor.200810014.
URL http://jila.colorado.edu/perkins/publications/optical-traps-single-molecule-biophysics-primer 1.4

[45] A. Ashkin. Obervation of a single-beam gradient force optical trap for dielectric particles. *Optics Letters* **11**(5), 288 (19862). doi:10.1364/OL.11.000288.
URL http://www.opticsinfobase.org/ol/abstract.cfm?URI=ol-11-5-288 1.4

[46] A. Ashkin. Forces of a single-beam gradient laser trap on a dielectric sphere in the ray optics regime. *Biophysical Journal* **61**(2), 569 (1992). doi:10.1016/S0006-3495(92)81860-X.
URL http://linkinghub.elsevier.com/retrieve/pii/S000634959281860X 1.4

[47] G. J. Brouhard, H. T. Schek, A. J. Hunt. Advanced optical tweezers for the study of cellular and molecular biomechanics. *Transactions on Biomedical Engineering* **50**(1), 121 (2003). doi:0.1109/TBME.2002.805463.
URL http://ieeexplore.ieee.org/xpl/articleDetails.jsp?arnumber=1179141 1.4, 2.2

[48] K. Visscher, S. P. Gross, S. M. Block. Construction of multiple-beam optical traps with nanometer-resolution position sensing. *Journal of Selected Topics in Quantum Electronics* **2**(4), 1066 (1996). doi:10.1109/2944.577338.
URL http://ieeexplore.ieee.org/xpl/articleDetails.jsp?arnumber=577338 1.4, 2.2

[49] S. C. Kuo, M. P. Sheetz. Force of single kinesin molecules measured with optical tweezers. *Science* **260**(5105), 232 (1993). doi:10.1126/science.8469975.
URL http://www.ncbi.nlm.nih.gov/pubmed/20151444 1.4

[50] J. D. Wen, M. Manosas, P. T. X. Li, S. B. Smith, C. Bustamante, F. Ritort, I. Tinoco. Force unfolding kinetics of RNA using optical tweezers. I. Effects of experimental variables on measured results. *Biophysical Journal* **92**(9), 2996 (2007). doi:10.1529/biophysj.106.094052.

URL http://www.pubmedcentral.nih.gov/articlerender.fcgi?artid=1852336&tool=pmcentrez&rendertype=abstract 1.4

[51] M. J. Footer, J. W. J. Kerssemakers, J. A. Theriot, M. Dogterom. Direct measurement of force generation by actin filament polymerization using an optical trap. *Proceedings of the National Academy of Sciences of the United States of America* **104**(7), 2181 (2007). doi:10.1073/pnas.0607052104.
URL http://www.pubmedcentral.nih.gov/articlerender.fcgi?artid=1892916&tool=pmcentrez&rendertype=abstract 1.4, 10

[52] J. W. J. Kerssemakers, E. L. Munteanu, L. Laan, T. L. Noetzel, M. E. Janson, M. Dogterom. Assembly dynamics of microtubules at molecular resolution. *Nature* **442**(7103), 709 (2006). doi:10.1038/nature04928.
URL http://www.ncbi.nlm.nih.gov/pubmed/16799566 1.4, 2.2

[53] L. Laan, J. Husson, E. L. Munteanu, J. W. J. Kerssemakers, M. Dogterom. Force-generation and dynamic instability of microtubule bundles. *Proceedings of the National Academy of Sciences of the United States of America* **105**(26), 8920 (2008). doi:10.1073/pnas.0710311105.
URL http://www.ncbi.nlm.nih.gov/pmc/articles/PMC2449340/ 1.4, 1.9, 2.2, 2.2, 4.3, 4.3.1, 6.1, 8, 8.1, 8.1, 8.2, 8.2.1, 9, A

[54] B. Zelinski, J. Kierfeld. Cooperative dynamics of microtubule ensembles: Polymerization forces and rescue-induced oscillations. *Physical Review E* **87**, 012703 (2013). doi:10.1103/PhysRevE.87.012703.
URL http://link.aps.org/doi/10.1103/PhysRevE.87.012703 1.4, 1, 1, 1

[55] B. Zelinski, N. Müller, J. Kierfeld. Dynamics and length distribution of microtubules under force and confinement. *Physical Review E* **86**, 041918 (2012). doi:10.1103/PhysRevE.86.041918.
URL http://link.aps.org/doi/10.1103/PhysRevE.86.041918 1, 1, 1, 1, 8.2.3, 1

[56] F. Verde, M. Dogterom, E. Stelzer, E. Karsenti, S. Leibler. Control of microtubule dynamics and length by cyclin A- and cyclin B-dependent kinases in Xenopus egg extracts. *The Journal of Cell Biology* **118**(5), 1097 (1992). doi:10.1083/jcb.118.5.1097.
URL http://www.jstor.org/stable/1615232 2.1, 2.1, 2.1, 2.1, 4.1, 4.2

[57] M. Dogterom, S. Leibler. Physical aspects of the growth and regulation of microtubule structures. *Physical Review Letters* **70**(9), 1347 (1993). doi:10.1103/PhysRevLett.70.1347.
URL http://link.aps.org/doi/10.1103/PhysRevLett.70.1347 2.1, 2.1, 2.1, 4.2

[58] B. Mulder. Microtubules interacting with a boundary: Mean length and mean first-passage times. *Physical Review E* **86**(1), 1 (2012). doi:10.1103/PhysRevE.86.011902. URL http://link.aps.org/doi/10.1103/PhysRevE.86.011902 2.1, 4.1

[59] K. Ookata, S. Hisanaga, J. C. Bulinski, H. Murofushi, H. Aizawa, T. J. Itoh, H. Hotani, E. Okumura, K. Tachibana, T. Kishimoto. Cyclin B Interaction with Microtubule-associated Protein 4 (MAP4) Targets p34cdc2 Kinase to Micrombules and Is a Potential Regulator of M-phase Microtubule Dynamics. *The Journal of Cell Biology* **128**(5), 849 (1995). doi:10.1083/jcb.128.5.849. URL http://www.ncbi.nlm.nih.gov/pmc/articles/PMC2120387/?tool=pmcentrez&rendertype=abstract 2.1

[60] M. E. Janson, M. Dogterom. Scaling of Microtubule Force-Velocity Curves Obtained at Different Tubulin Concentrations. *Physical Review Letters* **92**(24), 248101 (2004). doi:10.1103/PhysRevLett.92.248101. URL http://link.aps.org/doi/10.1103/PhysRevLett.92.248101 2.2, A, A.1

[61] C. S. Peskin, G. M. Odell, G. F. Oster. Cellular motions and thermal fluctuations: the Brownian ratchet. *Biophysical Journal* **65**(1), 316 (1993). doi:10.1016/S0006-3495(93)81035-X. URL http://linkinghub.elsevier.com/retrieve/pii/S000634959381035X 2.2, 2.2

[62] N. G. van Kampen. *Stochastic Processes in Physics and Chemistry.* Elsevier, Amsterdam (2007). 2.2, 8.2.5, 8.2.6, 8.2.6, 8.2.6

[63] C. Gardiner. *Stochastic Methods.* Springer, Heidelberg (2009). 2.2, 8.2.6

[64] A. Mogilner, G. Oster. The polymerization ratchet model explains the force-velocity relation for growing microtubules. *European Biophysics Journal* **28**(3), 235 (1999). doi:10.1007/s002490050204. URL http://www.springerlink.com/openurl.asp?genre=article&id=doi:10.1007/s002490050204 2.2

[65] A. E. Carlsson. Force-velocity relation for growing biopolymers. *Physical Review E* **62**(5), 7082 (2000). doi:10.1103/PhysRevE.62.7082. URL http://www.ncbi.nlm.nih.gov/pubmed/11102065 2.2

[66] J. Krawczyk, J. Kierfeld. Stall force of polymerizing microtubules and filament bundles. *Europhysics Letters* **93**(2), 28006 (2011). doi:10.1209/0295-5075/93/28006. URL http://stacks.iop.org/0295-5075/93/i=2/a=28006 2.2, 8.2.3

[67] A. B. Kolomeisky, M. E. Fisher. Force-Velocity Relation for Growing Microtubules. *Biophysical Journal* **80**(1), 149 (2001). URL http://dx.doi.org/10.1016/S0006-3495(01)76002-X 2.2

[68] H. Flyvbjerg, T. E. Holy, S. Leibler. Stochastic Dynamics of Microtubules: A Model for Caps and Catastrophes. *Physical Review Letters* **73**(17), 2372 (1994). doi:10.1103/PhysRevLett.73.2372.
URL http://link.aps.org/doi/10.1103/PhysRevLett.73.2372 2.3, 2.3, 2.3, 8.2.4

[69] L. Brun, B. Rupp, J. J. Ward, F. Nédélec. A theory of microtubule catastrophes and their regulation. *Proceedings of the National Academy of Sciences of the United States of America* **106**(50), 21173 (2009). doi:10.1073/pnas.0910774106.
URL http://www.pubmedcentral.nih.gov/articlerender.fcgi?artid=2795527&tool=pmcentrez&rendertype=abstract 2.3

[70] H. Bowne-Anderson, M. Zanicy, M. Kauer, J. Howard. Microtubule dynamic instability: A new model with coupled GTP hydrolysis and multistep catastrophe. *BioEssays* **35**(6), 579 (2013). doi:10.1002/bies.201370066.
URL http://www.ncbi.nlm.nih.gov/pubmed/23532586 2.3

[71] X. Li, R. Lipowsky, J. Kierfeld. Coupling of actin hydrolysis and polymerization: Reduced description with two nucleotide states. *Europhysics Letters* **89**(3) (2010). doi:10.1209/0295-5075/89/38010.
URL http://stacks.iop.org/0295-5075/89/i=3/a=38010 2.3

[72] F. Schwabl. *Quantenmechanik.* Springer, Heidelberg (2005). 2.3

[73] M. Abramowitz, A. I. Stegun. *Handbook of Mathematical Functions.* Dover Publications, Inc., New York (1965). 2.3

[74] O. Vallée, M. Soares. *Airy Functions and Applications to Physics.* Imperial College Press, London (2004). 2.3, 2.3

[75] M. E. Janson, M. E. de Dood, M. Dogterom. Dynamic instability of microtubules is regulated by force. *The Journal of Cell Biology* **161**(6), 1029 (2003). doi:10.1083/jcb.200301147.
URL http://www.pubmedcentral.nih.gov/articlerender.fcgi?artid=2173003&tool=pmcentrez&rendertype=abstract 2.3, 2.3, 2.3, 2.3, 8.2.4

[76] W. H. Press, S. A. Teukolsky, S. A. Teukolsky, B. Flannery. *Numerical Recipes 3rd Edition.* Cambridge University Press, Cambridge (2007). 3.1

[77] T. E. Holy, S. Leibler. Dynamic instability of microtubules as an efficient way to search in space. *Proceedings of the National Academy of Sciences of the United States of America* **91**(12), 5682 (1994). doi:10.1073/pnas.91.12.5682.
URL http://www.pubmedcentral.nih.gov/articlerender.fcgi?artid=44060&tool=pmcentrez&rendertype=abstract 4.1

[78] M. Dogterom, B. Yurke. Microtubule Dynamics and the Positioning of Microtubule Organizing Centers. *Physical Review Letters* **81**(2), 485 (1998). doi: 10.1103/PhysRevLett.81.485.
URL http://link.aps.org/doi/10.1103/PhysRevLett.81.485 4.1

[79] B. Govindan, W. Spillman. Steady states of a microtubule assembly in a confined geometry. *Physical Review E* **70**(3), 1 (2004). doi:10.1103/PhysRevE.70.032901.
URL http://link.aps.org/doi/10.1103/PhysRevE.70.032901 4.1, 4.1

[80] Y. A. Komarova, I. A. Vorobjev, G. G. Borisy. Life cycle of MTs: persistent growth in the cell interior, asymmetric transition frequencies and effects of the cell boundary. *Journal of Cell Science* **115**(Pt 17), 3527 (2002). doi:10.3410/f.1008394.105507.
URL http://www.ncbi.nlm.nih.gov/pubmed/12154083 4.1

[81] C. Faivre-Moskalenko, M. Dogterom. Dynamics of microtubule asters in microfabricated chambers: the role of catastrophes. *Proceedings of the National Academy of Sciences of the United States of America* **99**(26), 16788 (2002). doi: 10.1073/pnas.252407099.
URL http://www.pubmedcentral.nih.gov/articlerender.fcgi?artid=139222&tool=pmcentrez&rendertype=abstract 4.1

[82] N. Müller. *Polymerisationskinetik von Mikrotubuli unter Kraft.* Bachelor thesis, Technische Universität Dortmund (2011). 2

[83] C. Tischer, P. R. Ten Wolde, M. Dogterom. Providing positional information with active transport on dynamic microtubules. *Biophysical Journal* **99**(3), 726 (2010). doi:10.1016/j.bpj.2010.05.026.
URL http://www.pubmedcentral.nih.gov/articlerender.fcgi?artid=2913178&tool=pmcentrez&rendertype=abstract 4.3.2.1

[84] R. A. Walker, N. K. Pryer, E. D. Salmon. Dilution of Individual Microtubules Observed in Real Time. In Vitro : Evidence That Cap Size Is Small and Independent of Elongation Rate. *The Journal of Cell Biology* **114**(1), 73 (1991). doi:10.1083/jcb.114.1.73.
URL http://jcb.rupress.org/content/114/1/73 4.3.2.3

[85] R. M. Corless, G. H. G. D. E. G. Hare, D. J. Jeffrey, D. E. Knuth. On the Lambert W function. *Advances in Computational Mathematics* **5**(4), 329 (1996). doi:10.1007/BF02124750.
URL https://cs.uwaterloo.ca/research/tr/1993/03/W.pdf 8.1

[86] M. Dogterom, B. Yurke. Measurement of the Force-Velocity Relation for Growing Microtubules. *Science* **278**(5339), 856 (1997). doi:10.1126/science.278.5339.856.
URL http://www.sciencemag.org/cgi/doi/10.1126/science.278.5339.856 8.1

[87] T. Erdmann, U. S. Schwarz. Stability of Adhesion Clusters under Constant Force. *Physical Review Letters* **92**(10), 12 (2004). doi:10.1103/PhysRevLett.92.108102.
URL http://link.aps.org/doi/10.1103/PhysRevLett.92.108102 8.2.1

[88] T. Erdmann, U. S. Schwarz. Stochastic dynamics of adhesion clusters under shared constant force and with rebinding. *The Journal of Chemical Physics* **121**(18), 8997 (2004). doi:10.1063/1.1805496.
URL http://www.ncbi.nlm.nih.gov/pubmed/15527366 8.2.1

[89] M. F. Carlier. Synchronous Oscillations in Microtubule Polymerization. *Proceedings of the National Academy of Sciences of the United States of America* **84**(15), 5257 (1987). doi:10.1073/pnas.84.15.5257.
URL http://www.pnas.org/cgi/doi/10.1073/pnas.84.15.5257 8.2.3

[90] A. Marx, E. Mandelkow. A model of microtubule oszillation. *European Biophysis Journal* **22**(6), 405 (1994). doi:10.1007/BF00180162.
URL http://www.ncbi.nlm.nih.gov/pubmed/8149923 8.2.3

[91] S. H. Strogatz. *Nonlinear Dynamics and Chaos.* Westview Press, Boulder, Colorado (2000). 8.2.4

[92] R. Picone, X. Ren, K. D. Ivanovitch, J. D. W. Clarke, R. A. McKendry, B. Baum. A polarised population of dynamic microtubules mediates homeostatic length control in animal cells. *PLoS Biology* **8**(11), e1000542 (2010). doi:10.1371/journal.pbio.1000542.
URL http://www.pubmedcentral.nih.gov/articlerender.fcgi?artid=2982804&tool=pmcentrez&rendertype=abstract 9

[93] S. E. Kassar. *Regulation and filament growth in the cytoskeleton.* Diploma thesis, Technische Universität Dortmund (2013). 10

[94] M. Zeitz. *Feedback mechanism for microtubule polymerization regulation.* Diploma thesis, Technische Universität Dortmund (2013). 10

[95] D. N. Drechsel, A. A. Hyman, M. H. Cobb, M. W. Kirschner. Modulation of the dynamic instability of tubulin assembly by the microtubule-associated protein tau. *Molecular Biology of the Cell* **3**(10), 1141 (1992).
URL http://www.ncbi.nlm.nih.gov/pmc/articles/PMC275678/ A

[96] R. F. Gildersleeve, A. R. Cross, K. E. Cullen, A. P. Fagen, R. C. Williams. Microtubules grow and shorten at intrinsically variable rates. *The Journal of Biological Chemistry* **267**(12), 7995 (1992).
URL http://www.ncbi.nlm.nih.gov/pubmed/1569058 A

[97] R. Dhamodharan, P. Wadsworth. Modulation of microtubule dynamic instability in vivo by brain microtubule associated proteins. *Journal of Cell Science* **108**(4), 1679 (1995).
URL http://www.ncbi.nlm.nih.gov/pubmed/7615685 A

[98] C. Nakao, T. J. Itoh, H. Hotani, N. Mori. Modulation of the stathmin-like microtubule destabilizing activity of RB3, a neuron-specific member of the SCG10 family, by its N-terminal domain. *The Journal of Biological Chemistry* **279**(22), 23014 (2004). doi:10.1074/jbc.M313693200.
URL http://www.ncbi.nlm.nih.gov/pubmed/15039434 A

[99] E. Shelden, P. Wadsworth. Observation and quantification of individual microtubule behavior in vivo: microtubule dynamics are cell-type specific. *The Journal of Cell Biology* **120**(4), 935 (1993). doi:10.1083/jcb.120.4.935.
URL http://jcb.rupress.org/content/120/4/935 A

Teilpublikationen

- B. Zelinski, N. Müller and J. Kierfeld (2012).
  Dynamics and length distribution of microtubules under force and confinement.
  Physical Review E **86**, 041918, **arXiv:1212.3583**

- B. Zelinski and J. Kierfeld (2013).
  Cooperative dynamics of microtubule ensembles: Polymerization forces and rescue-induced oscillations.
  Physical Review E **87**, 012703, **arXiv:1301.1155**

Danksagung

An dieser Stelle möchte ich mich herzlich bei all denen bedanken, die zum Gelingen dieser Arbeit beigetragen haben.

An erster Stelle möchte ich mich bei Prof. Jan Kierfeld für die Vergabe des interessanten Themas und für die hervorragende Betreuung bedanken. Die vielen offen geführten Diskussionen und Anregungen haben maßgeblich zum Gelingen dieser Arbeit beigetragen. Ich habe mich in seiner Arbeitsgruppe stets wohlgefühlt und sehr viel gelernt.

Des Weiteren bedanke ich mich bei allen ehemaligen und aktuellen Mitgliedern der Arbeitsgruppe. Sie hatten immer ein offenes Ohr für Fragen und Probleme, forderten aber auch Ihren Teil meiner Zeit und Aufmerksamkeit.

Dr. Kai Schmidt, Prof. Dr. Ulrich Schwarz und Dr. Carsten Raas danke ich für die Begutachtung meiner Arbeit. Großer Dank gebührt auch allen Mitarbeitern von T1 und T2 für die angenehme und entspannte Arbeitsatmosphäre.

Vielen Dank auch an meine WG-Mitbewohner Tim Fischer, Felix Gorschlüter und Stefan Schmidt. Es ist immer schön nach Hause zu kommen.

Im Besonderen möchte ich mich bei meinen Eltern und meinem Bruder bedanken, die mich zu jeder Zeit und in jeglicher Hinsicht unterstüzt haben.